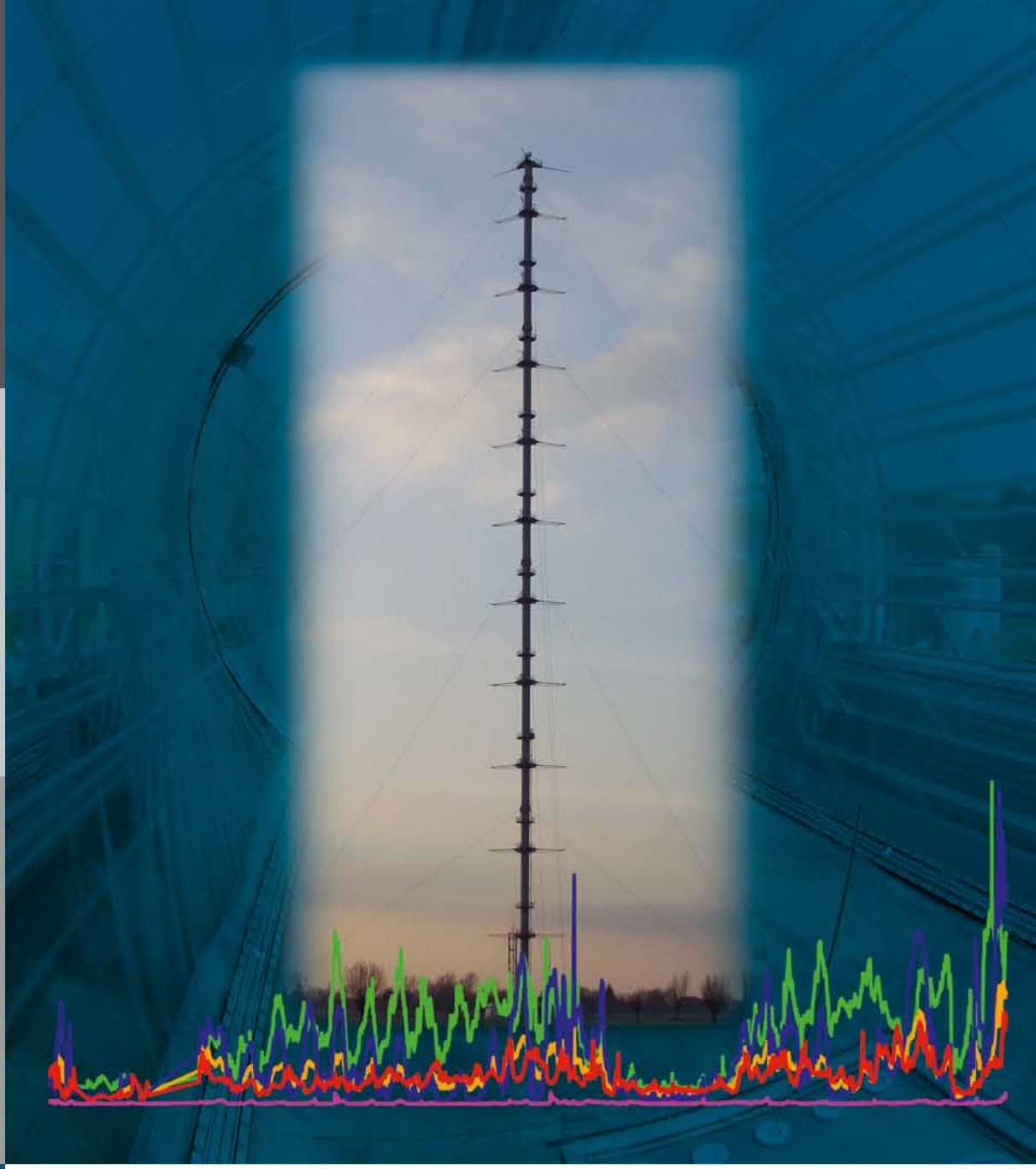

# Water and Organic Nitrate Detection in an AMS: Laboratory Characterization and Application to Ambient Measurements

Amewu A. Mensah

JÜLICH
FORSCHUNGSZENTRUM

Mitglied der Helmholtz-Gemeinschaft

Schriften des Forschungszentrums Jülich
Reihe Energie & Umwelt / Energy & Environment Band / Volume 104

Forschungszentrum Jülich GmbH
Institute of Energy and Climate Research (IEK)
Troposphere (IEK-8)

# Water and Organic Nitrate Detection in an AMS: Laboratory Characterization and Application to Ambient Measurements

Amewu A. Mensah

Schriften des Forschungszentrums Jülich
Reihe Energie & Umwelt / Energy & Environment Band / Volume 104

ISSN 1866-1793 ISBN 978-3-89336-698-9

Bibliographic information published by the Deutsche Nationalbibliothek.
The Deutsche Nationalbibliothek lists this publication in the Deutsche Nationalbibliografie; detailed bibliographic data are available in the Internet at http://dnb.d-nb.de.

| | |
|---|---|
| Publisher and Distributor: | Forschungszentrum Jülich GmbH<br>Zentralbibliothek<br>52425 Jülich<br>Phone +49 (0) 24 61 61-53 68 · Fax +49 (0) 24 61 61-61 03<br>e-mail: zb-publikation@fz-juelich.de<br>Internet: http://www.fz-juelich.de/zb |
| Cover Design: | Grafische Medien, Forschungszentrum Jülich GmbH |
| Printer: | Grafische Medien, Forschungszentrum Jülich GmbH |
| Copyright: | Forschungszentrum Jülich 2011 |

Schriften des Forschungszentrums Jülich
Reihe Energie & Umwelt / Energy & Environment Band / Volume 104

D 38 (Diss., Köln, Univ., 2010)

ISSN 1866-1793
ISBN 978-3-89336-698-9

The complete volume ist freely available on the Internet on the Jülicher Open Access Server (JUWEL) at http://www.fz-juelich.de/zb/juwel

*Für Fiona und Romeo*

Berichterstatter: PD Dr. Andreas Hofzumahaus, FZ Jülich
Prof. Dr. Andreas Wahner, FZ Jülich

Tag der mündlichen Prüfung: 21.04.2010

## Abstract

Atmospheric aerosols were studied by three different means. Laboratory experiments determined the relative ionization efficiency of water ($RIE_{H2O}$) in an Aerodyne Aerosol Mass Spectrometers (AMS), simulation chamber experiments gave insight to the reaction products of biogenic volatile organic compounds (BVOC) oxidation products, and the findings were applied to two field campaign measurements at Cabauw, NL, in May 2008 and February 2009. Knowing the liquid water content of aerosol particles is vital for the assessment of their climate forcing potential. A value of 2 for $RIE_{H2O}$ was determined by studying oxalate salts with different amounts of crystal water. BVOCs contribute much more to the global budget of VOCs than anthropogenic ones but oxidation products in terms of secondary organic aerosol often correlate to anthropogenic tracers such as $NO_x$ from fossil fuel burning. In atmospheric simulation chamber experiments, organic nitrates from BVOC-$NO_3$ oxidation showed higher vapor pressures than pure organic compounds produced in the same reactions. Organic nitrates comprised up to approx. 41 % of the particulate phase. A specific fragmentation ratio of nitrate ($NO_2^+/NO^+$) of 0.1 was found by high resolution AMS analysis differing strongly from the value of 0.4 known for the most abundant ambient $NO_3$ specie ($NH_4NO_3$). Ambient average particulate mass loadings were 9.72 µg/m$^3$ dominated by organics (40 %) in 2008 and 5.62 µg/m$^3$ dominated by nitrate (42 %) in 2009. Data comparison to collocated instruments showed good agreement. Positive Matrix Factorization analysis of the particulate organic fraction distinguished semi and low volatile oxygenated organic aerosol (OOA) as well as hydrocarbon like organic aerosol (HOA) in both campaigns. An additional highly oxygenated OA with a mass spectrum very similar to fulvic acid was found in 2008. The average contribution of organic nitrate to the particulate nitrate mass was 34.9 % in 2008 and 5.2 % in 2009.

## Kurzzusammenfassung

Atmosphärische Aerosolpartikel wurden mit Hilfe eines Aerosolmassenspektrometers untersucht. Der Flüssigwassergehalt atmosphärischer Aerosolpartikel spielt eine zentrale Rolle in ihrer Klimawirksamkeit. Durch Untersuchung des Kristallwassergehaltes von Oxalsäuresalzen wurde die relative Ionisierungseffizienz von Wasser mit einem Wert von 2 bestimmt. Global dominieren biogene flüchtige organische Substanzen (BVOC) das VOC-Budget. Ihre Oxidationsprodukte in Form von sekundären organischen Aerosolen können starke Korrelationen zu anthropogenen Spurenstoffen, z.B. $NO_x$ aufweisen. In der Atmosphärensimulationskammer SAPHIR wurden BVOCs mit $NO_3$ oxidiert. Die in diesen Reaktionen entstandenen organischen Nitrate wiesen einen deutlich höheren Dampfdruck auf als die gleichzeitig erzeugten rein organischen Verbindungen. Der Beitrag der Organonitrate zur gesamten partikulären Masse war ~ 41 %. Das spezifische Fragmentierungsmuster der Organonitrate von $NO_2^+$ zu $NO^+$ (0,1) unterscheidet sich signifikant von dem von Nitraten aus $NH_4NO_3$ (0,4). Die in den Laborstudien gewonnenen Erkenntnisse wurden bei der Analyse von Felddaten zweier Kampagnen in Cabauw, NL (Mai 2008 und Februar 2009) angewendet. Die mittlere Partikelbeladung betrug 9,72 µg/m$^3$ in 2008 und 5,62 µg/m$^3$ in 2009. 2008 wurde die Zusammensetzung der Partikel von organischen Verbindungen dominiert (40 %), 2009 von Nitrat (42 %). Vergleiche mit unabhängigen Methoden ergaben gute Übereinstimmungen. Der organische Anteil der Partikel wurde mithilfe der Methode der positiven Matrixfaktorisierung untersucht. Für beide Messperioden war der organische Beitrag in niedervolatile und semivolatile oxidierte sowie kohlenwasserstoffartige organische Verbindungen unterteilt. Zusätzlich wurde 2008 eine Komponente gefunden, die der Fulvinsäure stark ähnelt. Die Untersuchung des Fragmentierungsverhaltens des partikulären Nitrates ergab einen mittleren Beitrag organischer Nitrate von 34,9 % für 2008 und 5,2 % für 2009.

# Table of Contents

## List of Abbreviations

| | |
|---|---|
| AB | Air Beam |
| ACCENT | Atmospheric Composition Change the European NeTwork of excellence, http://www.accent-network.org/farcry_accent/ |
| AmOx | Ammonium Oxalate |
| AMS | Aerodyne Aerosol Mass Spectrometer |
| a.s.l. | above sea level |
| BC | Black Carbon |
| BVOC | Biogenic Volatile Organic Compounds |
| amu | atomic mass unit |
| BWP | Beam Width Probe |
| $C$ | Average Mass Loading |
| $CE$ | Collection Efficiency |
| CESAR | Cabauw Experimental Site for Atmospheric Research, |
| CL | Chemiluminescence |
| CPC | Condensational Particle Counter |
| $d_{\mathrm{m}}$ | mobility diameter |
| $d_{\mathrm{va}}$ | vacuum aerodynamic diameter |
| DMA | Differential Mobility Analyzer |
| $E_{\mathrm{b}}(d_{\mathrm{va}})$ | effect of particle phase on collection efficiency |
| $E_{\mathrm{L}}(d_{\mathrm{va}})$ | effect of the Liu-type aerodynamic lens on collection efficiency |
| $E_{\mathrm{S}}(d_{\mathrm{va}})$ | effect of particle size on collection efficiency |
| ECN | Energy Research Centre of the Netherlands, The Netherlands, http://www.ecn.nl/nl/ |
| EI | Electron Impact ionization |
| EMEP | European Monitoring and Evaluation Programme, http://www.emep.int/ |
| EUCAARI | European Integrated project on Aerosol Cloud Climate Air Quality Interactions, http://www.atm.helsinki.fi/eucaari/ |
| *FWHM* | Full Width Half Maximum |
| GHG | Green House Gases |
| HR-ToF | High-Resolution Time of Flight |
| $I$ | Ion Count Rate |
| ICG-2 | Institut für Chemie und Dynamik der Geosphäre, Troposphäre, Jülich, Germany, http://www.fz-juelich.de/icg/icg-2/ |
| *IE* | Ionization Efficiency |

## List of Abbreviations (continued)

| | |
|---|---|
| IMPACT | Intensive Measurement Period At Cabauw Tower |
| IPCC | Intergovernmental Panel On Climate Change; http://www.ipcc.ch/ |
| KNMI | Royal Netherlands Meteorological Institute, The Netherlands, http://www.knmi.nl/ |
| KOx | Potassium Oxalate |
| LED | Light Emitting Diode |
| MAAP | Multi Angle Absorption Photometer |
| MARGA | Measuring AeRosol and GAses |
| *MF* | Mass Fraction |
| MS | Mass Spectrometer |
| MS | Mass Spectrum |
| *MW* | Molecular Weight |
| *m*/*z* | mass to charge ratio |
| $N_A$ | Avogadro Constant = $6.022 \cdot 10^{23}$ $mol^{-1}$ |
| NaOx | Sodium Oxalate |
| NIST | National Institute for Standards and Technology |
| NO*x* | $NO + NO_2$ |
| OM | Organic Matter |
| OxAc | Oxalic Acid |
| PILS | Particle Into Liquid Sampler |
| PM | Particulate Matter |
| POA | Primary Organic Aerosol |
| ppb | Parts per billion ($10^{-9}$) |
| ppm | Parts per million ($10^{-6}$) |
| ppt | Parts per trillion ($10^{-12}$) |
| PSL | Polystyrene Latex Spheres |
| PToF | Particle Time of Flight |
| PTR-TD-MS | Proton-Transfer-Reaction Thermo-Desorption Mass Spectrometer |
| PulsedCRDS | Pulsed Cavity Ring-Down Spectrometer |
| *Q* | Volumetric Flow Rate |
| Q-MS | Quadrupole Mass Spectrometer |
| $\rho$ | Density |

## List of Abbreviations (continued)

| | |
|---|---|
| *RH* | Relative Humidity |
| *RIE* | Relative Ionization Efficiency |
| *RP* | Resolving Power |
| SAPHIR | Simulation of Atmospheric PHoto oxidation In a large Reaction chamber |
| SJAC | Steam Jet Aerosol Collector |
| SMPS | Scanning Mobility Particle Sizer |
| SOA | Secondary Organic Aerosol |
| TD-LIF | Thermal Dissociation Laser Induced Fluorescence |
| TNO | Built Environment and Geosciences Airquality & Climate, Uetrecht, The Netherlands, http://www.tno.nl/index.cfm |
| toc | total organic carbon |
| UMR | Unit Mass Resolution |
| WAD | Wet Annular Denuder |
| WSOC | Water Soluble Organic Carbon |
| VOC | Volatile Organic Compounds |

# 1. Introduction

Aerosols are defined as suspended particulate matter (PM), which can be solid or liquid in addition to the surrounding gas phase. The aerosol particles are characterized by their size, composition and shape. The size, mostly referred to as the particle diameter, spans over several orders of magnitude from a few nanometers to several micrometers (Figure 1.1). There is no clear definition of a lower size limit due to floating transition from molecules to small particles in the size range below 10 nm. Particles much larger than several micrometers are too large to stay suspended and fall out of the gas phase within a short time. Atmospheric particles are generally classified as nucleation, accumulation, or coarse mode particles (Figure 1.1), which can be determined by size distribution measurements.

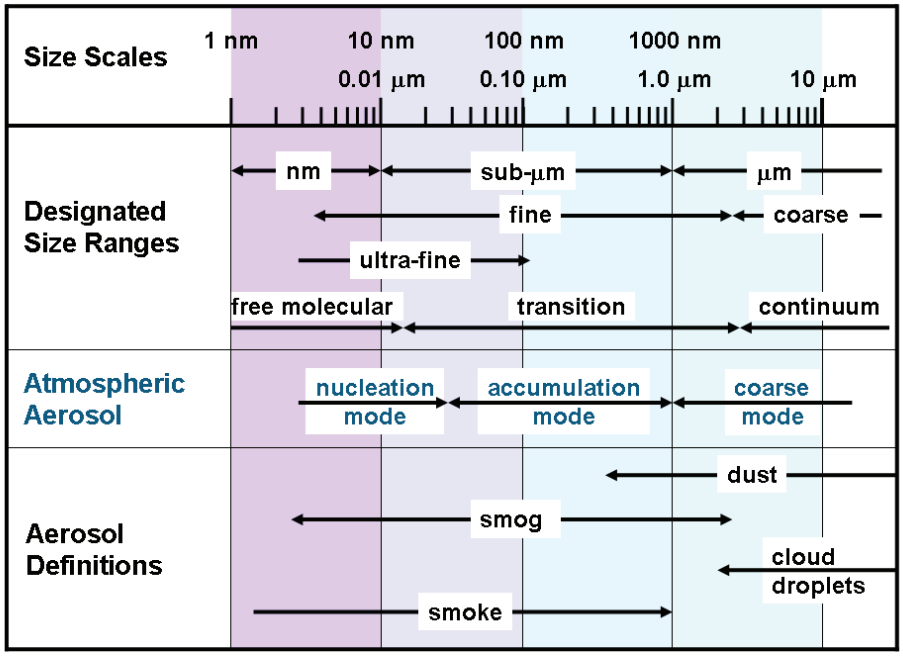


Figure 1.1 Size ranges, size definitions and corresponding examples of atmospheric aerosol particles adopted from [*Hinds*, 1999].

Aerosol particles directly and indirectly affect the global climate. Depending on their optical properties, particles can scatter or absorb long and short wave radiation. This has an impact on visibility (global dimming [*Nazarenko and Menon*, 2005; *Ramanathan et al.*, 2007; *Romanou et al.*, 2007]) and can have cooling or heating effects on the

atmosphere. They also exhibit a range of indirect effects such as altering the properties of clouds or acting as surface for heterogeneous reactions. Their most important impact an cloud properties is acting as cloud condensation nuclei (CCN). Changes in particle number concentration and size distribution alter cloud albedo [*Norris and Wild*, 2007] and can cause suppression or enhancement of rain [*Nober et al.*, 2003; *Tao et al.*, 2007; *Vaughan T. J. Phillips*, 2002]. A property determining the direct and indirect climate effects of particles is the ability to take up water referred to as hygroscopicity of the particle. Hygroscopicity is used as an indirect measure of the particles liquid water content in atmospheric studies [*Ehn et al.*, 2007; *Hämeri et al.*, 2001; *Jimenez et al.*, 2009; *Neusüß et al.*, 2002; *Saxena and Hildemann*, 1996]. Direct measurements of the particles liquid water content, which are hard to achieve up to now, would improve the understanding of aerosol particles impact on the global climate significantly. The IPCC report 2007 [*IPCC*, 2007] identifies aerosol particles as the major uncertainty in the prediction of future climatic conditions. Furthermore, aerosol particles are associated with health hazards such as increased cardiopulmonary [*Moolgavkar et al.*, 1994] or lung cancer mortality [*Pope et al.*, 2002].

While the large size range that is covered by atmospheric aerosol particles opens a wide field of complexity on its own, further complexity is added by the compositional variability of the particles. Apart from the above mentioned water, the major constituents found in atmospheric aerosol particles are sulfate, nitrate, ammonium, minerals, black carbon (BC) and organic components often referred to as organic matter (OM) [*Rogge et al.*, 1993]. The fractional abundance of the individual constituents is strongly dependent on the particles origin and process of formation.

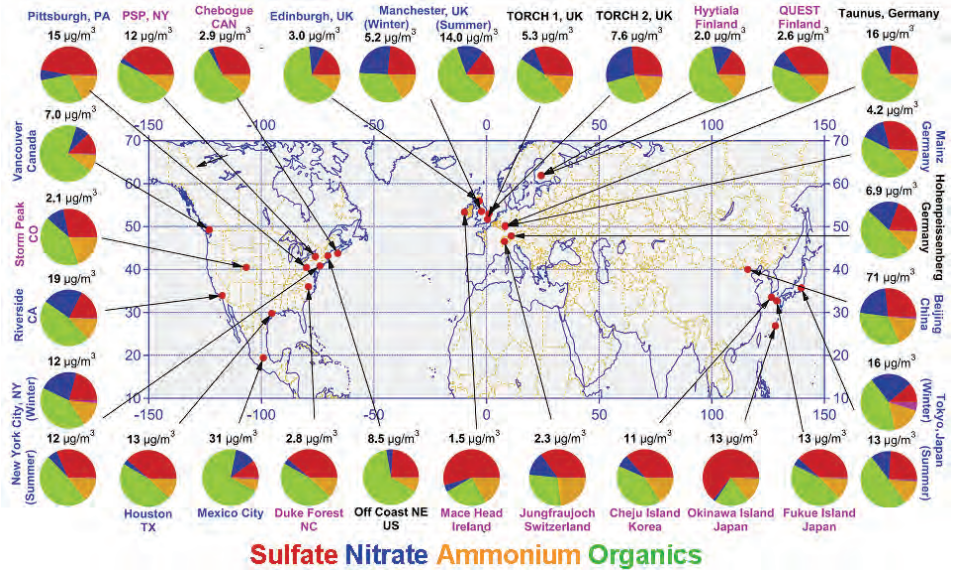


Figure 1.2 Aerosol mass spectrometric measurements of the fine particulate aerosol fraction. Colors for the study labels indicate the type of sampling location: urban areas (blue), <100 miles downwind of major cites (black), and rural/remote areas >100 miles downwind (pink). Pie charts show the average mass concentration and chemical composition: organic matter (organics, green), sulfate (red), nitrate (blue), and ammonium (orange) [*Zhang et al.*, 2007].

Figure 1.2 (taken from [*Zhang et al.*, 2007]) shows the average mass concentrations of aerosol particles in the fine mode determined by aerosol mass spectrometric measurements across the Northern Hemisphere. The fractional abundance of sulfate (red), nitrate (blue), ammonium (orange), and organics (OM, green) is given in the pie charts. As can be seen, OM accounts for a significant fraction in all measurements independent of location.

While it is comparatively easy to get insights to the physical properties such as the size distribution or refractive index of aerosol particles, compositional analysis especially of the organic fraction is still very challenging. Organic aerosols can be separated into primary (POA) and secondary (SOA) depending on their process of formation (Figure 1.3). POA consists of particles that are directly emitted into the atmosphere such as black carbon from anthropogenic combustion processes or plant debris from biogenic sources. SOA in contrast is formed by gas to particle conversion of semi and low volatile organic compounds (VOC) after their oxidation. The global VOC budget is dominated by biogenic emissions, which are estimated to be at the order of 1150 Tg C/a and therefore almost a tenfold of anthropogenic emissions [*Guenther et al.*, 1995].

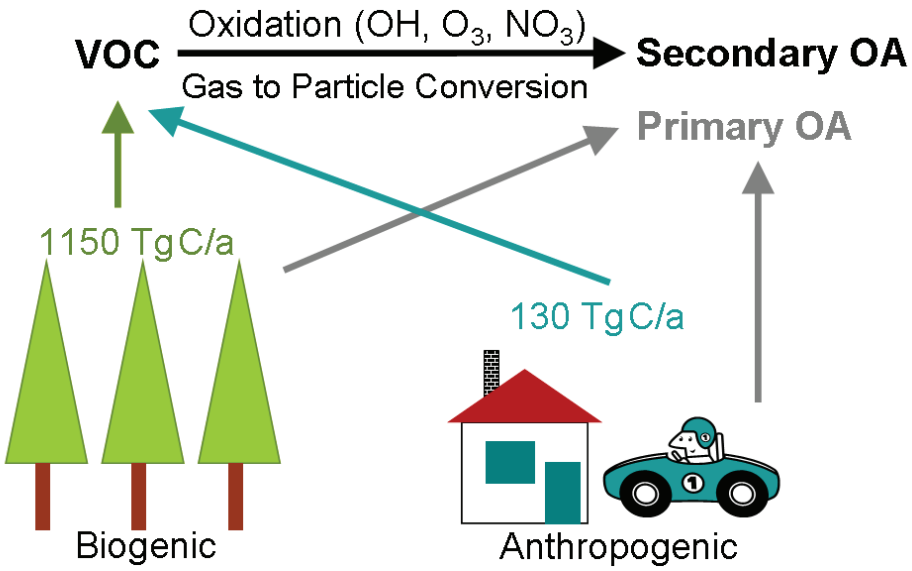


Figure 1.3 Sources of organic aerosol particles. Emission rates are taken from [*Guenther et al.*, 1995].

VOCs are primarily oxidized by hydroxy radicals (•OH), ozone ($O_3$) and nitrate radicals (•$NO_3$) in the tropospheric atmosphere. From these three oxidants, only $NO_3$ is considered to be mainly of anthropogenic origin. This is due to the fact that the nitrate radical is formed by oxidation of $NO_2$ with ozone (equation (1.1a)) and the educt $NO_2$ is part of $NO_x$ (= NO + $NO_2$) which is strongly associated with anthropogenic emissions [*Finlayson-Pitts and Pitts*, 2000].

$$NO_2 + O_3 \rightarrow NO_3 + O_2 \quad \textbf{(1.1a)}$$

$$NO_3 + NO_2 \leftrightarrow N_2O_5 \quad \textbf{(1.1b)}$$

At high $NO_3$ concentrations further addition of $NO_2$ leads to $N_2O_5$ which decomposes in case of $NO_3$ depletion (equation (1.1b)). $NO_3$ is rapidly photolyzed by sunlight causing it to reach significant oxidation potential only during night times. This is contrary to OH, which is only active during daytime, since it is produced from the reaction of water vapor with exited oxygen atoms and the exited oxygen atoms in turn are produced by photolysis of ozone at wavelengths below 360 nm. Ozone itself can be found at significant concentrations both under day or night conditions. When VOCs are oxidized compounds of high, semi, and low volatility are formed. While high volatile compounds remain in the gas phase, low and semi volatile compounds lay the basis for SOA particles by gas to particle conversion (upper part of Figure 1.3). Low volatile compounds

condensate on preexisting or nucleate to form new particles and semi volatile compounds partition between gas and particulate phase.

In the light of the high biogenic contribution to VOC (BVOC) emissions [*Guenther et al.*, 1995] and high rate coefficients of VOCs with $NO_3$ [*Atkinson*, 1997; *Atkinson and Arey*, 2003] the oxidation of BVOCs by $NO_3$ might lead to a significant contribution to the total SOA budget [*Fry et al.*, 2009]. Still, most studies on atmospheric SOA formation from the oxidation of VOCs focus on OH and $O_3$ oxidation and only a limited number of studies investigate the $NO_3$ oxidation of VOCs and subsequent SOA formation, some of which are [*Griffin et al.*, 1999; *Hallquist et al.*, 1999; *Hoffmann et al.*, 1997; *Skov et al.*, 1992]. The deficit of knowledge on this reaction scheme causes this SOA production pathway to be neglected in most global models. The discrepancies between measured and modeled SOA budgets as reported by [*Hallquist et al.*, 2009; *Kanakidou et al.*, 2005; *Volkamer et al.*, 2006] might be reduced by implementation of the $NO_3$ + BVOC reaction into global models [*Fry et al.*, 2009].

The statements of the last two paragraphs indicate that the investigation of aerosol particles in the whole extend of their physical and chemical properties is challenging. Laboratory, simulation chamber, and field measurements allow the experimental investigation of aerosol particles with increasing dimension of scale and complexity. Small scale laboratory experiments on the one hand allow for the best investigation of singular, clearly defined processes and properties. Field measurements on the other side give insights to the real atmospheric particle behavior but the interpretation of the findings are difficult to decouple from meteorological aspects such as transport, precipitation or temperature. An intermediate position between field and laboratory in terms of complexity and scale is taken by simulation chambers. Experiments in simulation chambers are performed in a controlled environment, but the conditions can be set to be close to the real atmosphere. Knowledge gained in laboratory or simulation chamber experiments is applied to field measurements and questions that arise at field measurements can be investigated in detail in chamber/laboratory experiments.

In the present work aerosol mass spectrometry (AMS, detailed description in chapter 2) was used to investigate the chemical composition of aerosol particles in laboratory (chapter 3), simulation chamber (chapter 4) and field studies (chapter 5). The relative ionization efficiency of water ($RIE_{H2O}$) in an AMS was determined in laboratory experiments (chapter 3). The knowledge of the $RIE_{H2O}$ is an important step on the way to

measure the particles liquid water content directly and thereby increase the understanding of particle-gas phase interactions and the impact of aerosol particles on the global climate. The SOA and organic nitrates produced by $NO_3$ oxidation of three different BVOCs in an atmospheric simulation chamber were investigated towards their physical and chemical properties (chapter 4). Furthermore, a detection scheme for organic nitrates by mass spectrometric measurements was developed. The findings gained from these two studies performed under controlled laboratory conditions were applied to two field measurement datasets collected at Cabauw, The Netherlands, a representative measurement site for Western Europe (chapter 5). Atmospheric particles water and organic nitrate content were investigated.

# 2. The Aerosol Mass Spectrometer

The first step in investigating aerosol particles is the decision on the right sampling and analyzing technique. Offline and online techniques exist for the chemical investigation of OA. The collection of aerosol particles on filters and subsequent extraction and analysis of the particles is an offline technique. Extraction and analysis can be for example the dissolution of the collected particles in an organic solvent followed by gas chromatographic/mass spectrometric analysis of the eluent. If high particle loads are sampled, only parts of the filter are needed for an analysis allowing to address several different questions by one probe. The disadvantage of offline measurements is a generally low time resolution ranging from hours to days. Since atmospheric situations can change very rapidly, this causes the investigation of an averaged sample. Furthermore, the handling and storage of the samples can analysis cause contamination, evaporation of semi volatile components, or aging and alteration due to chemical reactions during storage. Online sampling techniques minimized the alteration of the sampling probe since the probe is analyzed almost instantaneously after sampling. Analytical difficulties arise since only low mass loadings can be sampled if sampling intervals range from seconds to a few minutes. This becomes clear when considering the low ambient concentrations of aerosol particles compared to has phase concentrations. Particle concentrations typically range from few microgram per meters cubed in remote areas like Hyttiälä, FIN [*Zhang et al.*, 2007] to about 100 $\mu g/m^3$ in polluted areas like Mexico City, MX [*Aiken et al.*, 2009] while gaseous nitrogen alone has a concentration of $950 \cdot 10^6$ $\mu g/m^3$ in the air. Therefore, when applying online techniques only a limited number of questions can be addressed. Online instruments generally need to be transportable, i.e. of limited size and mass, thereby limiting the analyzing techniques to the ones that do not require an entire laboratory set up. A commercially available online instrument is the Aerodyne Aerosol Mass Spectrometer (AMS). It is a very powerful instrument that allows to address the questions of aerosol particles mass, size distribution, composition, shape and even partly volatility. Additionally high time resolution can be achieved with the AMS. Two types of this instrument were used for the investigation of aerosol particles presented in this work. The set-up (chapter 2.1), working principle (chapter 2.2 and 2.3), and operation (chapter 2.4) will be presented in the upcoming sections.

## 2.1. Set Up of the AMS

The Aerodyne Aerosol Mass Spectrometer (AMS) [*Canagaratna et al.*, 2007; *Jayne et al.*, 2000; *Jimenez et al.*, 2003] is a particle analyzing instrument which allows the mass spectrometric online investigation of aerosol particle composition after separation from the gas phase. The AMS is built up in four sections: an aerodynamic lens as inlet, a differentially pumped vacuum particle sizing chamber, a vaporization/ionization region and a mass spectrometer (MS).

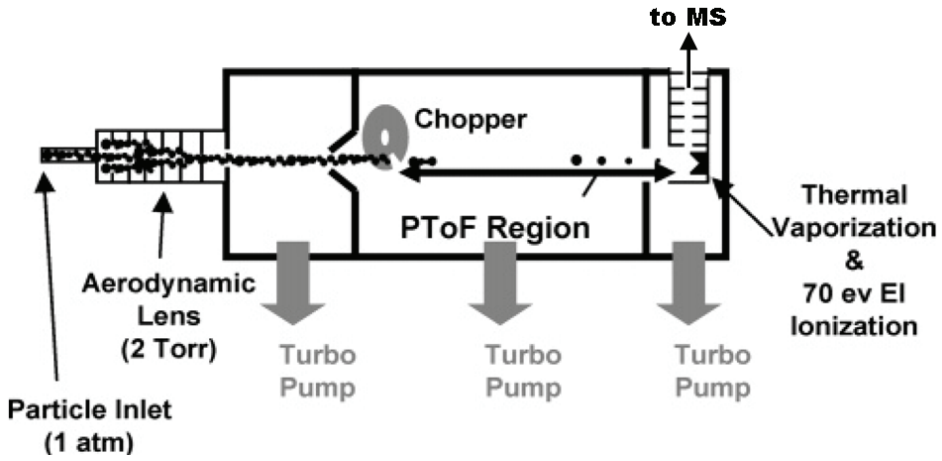


Figure 2.1 Schematic drawing of an AMS (partly taken from [*DeCarlo et al.*, 2006]).

An aerosol stream of 80 mL/min passes through a Liu type aerodynamic lens [*Liu et al.*, 1995a; b]. The lens reduces the gas phase to particle phase concentration by a factor of $10^7$. It focuses the particle stream to a narrow beam of about 1 mm diameter and has an almost 100 % transmission efficiency for particles between 70 nm and 500 nm. Particles in the size ranges of 30 nm to 70 nm and 500 nm to 2500 nm are still substantially transmitted, with a 50 % transmission efficiency for particles of 1 µm [*Jayne et al.*, 2000; *Zhang et al.*, 2004]. Hence, the AMS is referred to as $PM_1$ instrument [*Canagaratna et al.*, 2007].

The particles are accelerated at the exit of the lens and fly through a particle sizing chamber with a pressure within the chamber of approximately $10^{-3}$ Pa. The particle sizing is achieved by measuring the particles time of flight (PToF) between entering the chamber and detection, since the particles velocity is directly proportional to their aerodynamic diameter. A spinning disk that has two radial slits chops the particle beam at the exit of the aerodynamic lens. The recording of the flight time starts when the particles pass through

one of the slits, detected by an LED and a photodiode, and ends when ion signal is detected.

After passing through the PToF chamber the particle beam strikes a conic tungsten surface, the so called vaporizer. The vaporizer consists of porous tungsten and has an inverted conical shape, to achieve optimum particle collection efficiency. The temperature of the vaporizer can be modulated from about 150 °C to about 950 °C and is chosen such that maximum signal is obtained. In general, the vaporizer is operated at approximately 600°C causing the non-refractory components of the particles to flash evaporate on the surface [*Jayne et al.*, 2000].

The evaporated molecules are ionized by 70 eV Electron Impact (EI). The required electrons are emitted by a filament that is located millimeters beside the vaporizer. The ionized molecules are then extracted into the MS for compositional analysis. EI ionization is a standard ionization method. Acquired mass spectra can therefore be compared to data base spectra like the public available data base from the National Institute for Standards and Technology (NIST). One must keep in mind, that the flash evaporation of the particles introduces additional internal energy which in turn leads to a high degree of fragmentation when the molecules are ionized.

A Quadrupole AMS (Q-AMS) and a High Resolution Time of Flight AMS (HR-ToF-AMS) were used in this work. The major difference between these two instruments is the mass spectrometer. The quadrupole mass spectrometer (Q-MS) consecutively scans a defined range of mass to charge ratios ($m/z$'s) with only a narrow mass range reaching the detector at a given time. The scan of a mass range of 300 $m/z$'s requires about 300 ms [*Drewnick et al.*, 2007]. Opposite to this, the HR-ToF mass spectrometer acquires all $m/z$'s in one ion extraction, which occurse about every 30 µs in V-mode and ever 50 µs in W-mode. V- and W- mode refer to the flight path of the ions within the MS. V-mode is a single reflection flight path and W-mode is a triple reflection flight path of 1.3 m and 2.9 m, respectively [*DeCarlo et al.*, 2006] resulting in a high mass resolution. The resolving power ($RP$) of the MS is defined as the ratio of the nominal mass ($m$) to the full width of the signal at half maximum ($\Delta m$):

$$RP = \frac{m}{\Delta m}. \qquad \textbf{(2.1)}$$

A resolving power of about 2000 and 4000 is achieved in V-mode and W-mode, respectively, while the Q-MS achieves a resolving power of about 100 [*DeCarlo et al.*,

2006]. Figure 2.2 (taken from [*DeCarlo et al.*, 2006]) shows the mass spectrometric signals of different AMS types at *m*/*z* 43 and *m*/*z* 44 in comparison. The resolving power of the HR-ToF-MS allows a clear separation of individual ions (dotted line V-mode and thin black line W-mode) in contrast to the signal of the Q-MS (thick black line) as shown in the inset for *m*/*z* 43.

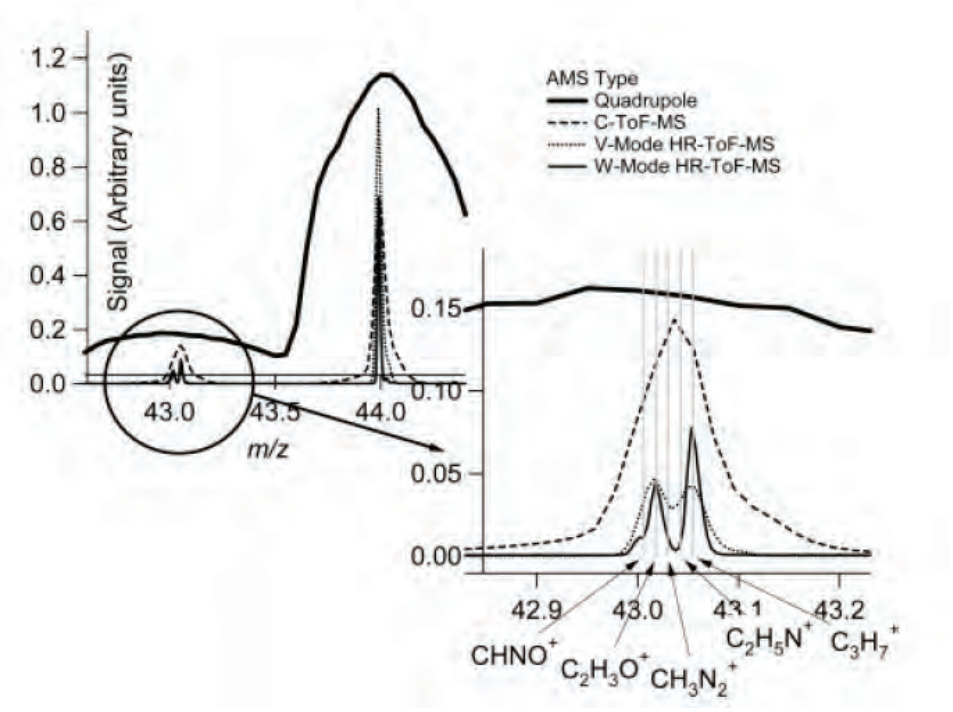


Figure 2.2 Display of the resolving power of different AMS types taken from [*DeCarlo et al.*, 2006].

## 2.2. Identification of Chemical Compounds in the AMS

Electron impact (EI) ionization is an ionization method that causes fragmentation of the molecules due to the high energy of the electrons (70 eV), which is significantly higher than the average ionization energy of molecules like water (12.62 eV). An assignment of the resulting fragments to parenting ions is possible when the fragmentation pattern of the ions is know [*McLafferty and Turecek*, 1993]. This in turn allows for assumptions on the parenting ion on the basis of the detected fragments. The fragmentation pattern of a molecule depends not only on the ionization method but on the entire scheme of molecule/ion production. Though basic patterns are always valid for a specific ionization method, the fragmentation patterns of individual instruments need to be determined. In the

case of the AMS, the combination of flash evaporation and EI ionization causes a higher degree of fragmentation than can be found in standard mass spectrometric data base. Still, constant instrument performance results in constant fragmentation pattern of the parenting ions. The total amount of the parenting ion can be determined by investigation of the major fragments. In contrast to mass spectra obtained with a HR-ToF-AMS, only Unit Mass Resolution (UMR) mass spectra can be obtained with a Q-AMS. Its limited resolving power inhibits to resolve the contributions of different species to the signal on a single *m*/*z* (Figure 2.2). This limitation demands for a technique to attribute fractions of the signal to different species and is achieved by the application of the so called fragmentation table. The fragmentation table consists of rows representing the *m*/*z*'s and columns representing the individual species (Table 2.1).

Table 2.1 Part of the AMS fragmentation table (taken from [*Allan et al.*, 2004]).

The fragmentation tables for gas phase water (frag_RH), the $^{16}O^+$ and $^{16}O_2^{2+}$ fragments due to gas phase oxygen (frag_O16), particulate water (frag_water) and ammonium (frag_$NH_4$)

| *m/z* | frag_RH | frag_O16 | frag_water | frag_$NH_4$ |
|---|---|---|---|---|
| 15 | | | | 0.1*frag_$NH_4$[16][b] |
| 16 | 0.04*frag_RH[18][b] | 0.353*frag_air[14][b] | 0.04*frag_water[18][b] | [16], −frag_water[16], −frag_air[16], −frag_sulphate[16], −frag_organic[16] |
| 17 | 0.25*frag_RH[18][b] | | 0.25*frag_water[18][b] | [17], −frag_water[17], −frag_air[17], −frag_sulphate[17], −frag_organic[17] |
| 18 | 0.01*frag_air[28][b] | | [18], −frag_air[18], −frag_sulphate[18], −frag_organic[18] | |
| 19 | 0.000691*frag_RH[18][a], 0.002*frag_RH[17][a] | | 0.000691*frag_water[18][a], 0.002*frag_water[17][a] | |
| 20 | 0.002*frag_RH[18][a] | | 0.002*frag_water[18][a] | |

The relative contribution to the gas phase from water vapour is typically variable in time and to be completely thorough, should be accounted for by adjusting the multiplier in the frag_RH[18] entry. However, any inaccuracy in this number will only affect the ability to quantitatively distinguish water vapour from particulate water, which is not required in most applications. The ratio governing the $^{16}O^+$ and $^{16}O_2^{2+}$ peak is variable between instruments and configurations and has to be set correctly in order to be able to calculate ammonium concentrations correctly.

Though the concentration of the gas phase is reduced by a factor of $10^7$ within the aerodynamic lens, significant concentrations of the major gas phase species are still detected in the AMS. The sum of these species is called Air Beam (AB). Gas phase species like oxygen and water in the form of relative humidity contribute to the signal on *m*/*z* 16. At the same time, the major fragment of particulate ammonium generated in an AMS is detected on *m*/*z* 16 ($NH_2^+$), which can be read from the row corresponding to *m*/*z* 16 in the fragmentation table in Table 2.1. To account for interferences or specific measurement

conditions the contribution of the individual species needs to be determined. Results of laboratory experiments on the fragmentation behavior of compounds are used in the case of particulate interferences. The contribution of gas phase components to the signal on a specific *m/z* can be determined by the analysis of particle free air. In general, a particle filter (e.g. HEPA) is placed into the sampling line to attain particle free air. If in this particle free air signal on e.g. *m/z* 16 is taken as a positive or negative mass loading of a particulate species like ammonium, the contribution of the interfering gas phase species (here e.g. $O^{16}$, frag_O16) needs to be corrected.

As discussed in chapter 1, aerosol particles can be composed of a huge variety of individual substances. Some of the "species" of interest detected in an AMS are water ($H_2O$), ammonium ($NH_4$), nitrate ($NO_3$), sulfate ($SO_4$), and organic matter (OM) called organics (Org). Note, that in aerosol and especially the AMS community the notation deviates from IUPAC suggestions, i.e. molecules like $NH_4$ or $NO_3$ are not presented as ions but as "species". $NO_3$ detected in the AMS might originate from $HNO_3$, nitrate salts or organic nitrate. The vaporizing, ionization, and detection scheme does not allow a direct determination of the origin without further analysis. The major ion fragments of these substances as they are detected in an AMS are listed in Table 2.2.

Table 2.2 List of species and major detected ion fragments in an AMS. Bold face denotes these ions, which are preferentially used for species detection and further mass determination (taken from [*Canagaratna et al.*, 2007]).

| Group | Molecule/Species | | Ion Fragments | Mass Fragments |
|---|---|---|---|---|
| Water | $H_2O$ | $e^-$ → | $H_2O^+$, $HO^+$, $O^+$ | **18**, 17, 16 |
| Ammonium | $NH_3$ | $e^-$ → | $NH_3^+$, $NH_2^+$, $NH^+$ | 17, **16**, 15 |
| Nitrate | $HNO_3$ | $e^-$ → | $HNO_3^+$, $NO_2^+$, $NO^+$ | 63, **46**, **30** |
| Sulfate | $H_2SO_4$ | $e^-$ → | $H_2SO_4^+$, $HSO_3^+$, $SO_3^+$ $SO_2^+$, $SO^+$ | 98, 81, 80 **64, 48** |
| Organic *(Oxygenated)* | $C_nH_mO_y$ | $e^-$ → | $H_2O^+$, $CO^+$, $CO_2^+$ $H_3C_2O^+$, $HCO_2^+$, $C_nH_m^+$ | 18, 28, **44**, **43**, 45, ... |
| Organic *(hydrocarbon)* | $C_nH_m$ | $e^-$ → | $C_nH_m^+$ | 27, 29, **41, 43, 55, 57**, 69, 71... |

## 2.3. Quantification in the AMS

The measured particulate aerosol mass concentration ($C$) of the AMS [*Jimenez et al.*, 2003] can be calculated as:

$$C = \frac{1}{CE}\frac{1}{Q}\frac{MW}{N_A}\frac{1}{IE}I\,. \qquad \textbf{(2.2)}$$

The average mass concentration ($C$ [µg/m$^3$]) depends on the collection efficiency ($CE$, explained in detail at the end of this chapter), the volumetric flow rate ($Q$ [m$^3$/s]) into the instrument, the average molecular weight ($MW$ [µg/mol]) and ionization efficiency ($IE$) of the compounds in the particle, and the ion count rate ($I$ [s$^{-1}$]) detected in the mass spectrometer. $N_A$ is the Avogadro constant. While $CE$ and $IE$ account for the systematic error in $C$, the statistical error is caused by the counting statistics of $I$. The bulk mass loading is the sum over the mass loadings of individual components of the aerosol particles. The mass concentration of a specific compound like nitrate can be written as:

$$C_{NO_3} = \frac{1}{CE}\frac{1}{IE_{NO_3}}\frac{1}{Q}\frac{MW_{NO_3}}{N_A}\sum_{f=30,46} I_f\,. \qquad \textbf{(2.3)}$$

Here, the individual ionization efficiency ($IE_{NO3}$), molecular weight ($MW_{NO3}$) and ion counts of the compounds fragments ($I_f$) are taken into account. A compound is detected as fragments on specific $m/z$'s as a result of the vaporization and ionization scheme of the AMS. Each compound has a specific ionization pattern, which allows the calculation of the total amount on the basis of the most prominent ions. The most prominent ions of e.g. nitrate are the $NO^+$ ion on $m/z$ 30 and the $NO_2^+$ ion on $m/z$ 46 (Table 2.2).

For quantitative measurements with the AMS the ionization efficiency ($IE$) needs to be determined. The $IE$ of the instrument is determined by a calibration with ammonium nitrate particles [*Drewnick et al.*, 2004; *Jayne et al.*, 2000]. In the standard calibration procedure dried and size selected ammonium nitrate particles are measured with the AMS and a condensational particle counter (CPC) in parallel. Taking the bulk density of ammonium nitrate, the size, and the number of the particles, the total mass of aerosol particles introduced into the AMS can be calculated. This value is compared to the detected ion signal of the mass spectrometer. A scaling factor is introduced to link the amount of molecules introduced into the AMS with the ion count per molecule detected by

the AMS. The scaling factor, the so called *IE*, is in general at the order of $10^{-6}$ ions/molecule.

The ammonium nitrate calibration allows the determination of the mass of different compounds as nitrate equivalent mass. The actual mass of the compound of interest can be determined, when the compounds specific ionization efficiency is known. In practice, ionization efficiencies relative to the nitrate $IE_{NO3}$ are used. These ionization efficiencies are called relative ionization efficiencies (*RIE*). The *RIE* of $NH_4$ ($RIE_{NH4}$), which is determined during the standard *IE* calibration, is generally about 4. I.e., the ionization efficiency of $NH_4$ is four times higher than the ionization efficiency of nitrate. By application of the relative ionization efficiency, the absolute amount of a specific compound can be determined with the AMS. The determination of the *RIE* for individual species is an ongoing process in the AMS community. Up to now the *RIE* of some species measured by the AMS are still not known. In these cases the *RIE* is set to 1 and the detected masses are reported as nitrate equivalent masses.

To assure correct size distribution measurements, the AMS size detection needs to be calibrated. All calibrations performed for the work presented here were performed with Polystyrene Latex Spheres (PSL, Duke Scientific Corporation, Palo Alto CA) of different sizes over the size range of interest, i.e. 8 sizes between 81 nm and 596 nm. Aqueous solutions of the PSLs were nebulized by a constant output atomizer (TSI 3076), the produced particles are dried by silica gel and introduced into the AMS. Flight velocities of the individual PSLs were fitted to their diameter to yield a calibration curve according to equation (2.4).

$$v = \frac{v_{lens} + (v_{gas} - v_{lens})}{\left(1 + \frac{d_{va}}{D^*}\right)^b} \qquad \textbf{(2.4)}$$

Here, $v$ is the measured flight velocity of the particles, $v_{lens}$ the velocity of the largest particles, that are transmitted through the lens, $v_{gas}$ the maximal velocity of gas molecules behind the lens, $d_{va}$ the aerodynamic vacuum diameter of the particles, and $D^*$ and b are fitted coefficients. An example of calibration data and the corresponding fit curve is given in Figure 2.3. The black line represents the fit curve obtained from size calibration measurements with PSLs on 28.04.08. The corresponding data is not shown to increase clarity. Superimposed on the fit curve are calibration data obtained from measurements on 01.05.08 (black upright diamonds), 03.05.08 (green squares), and 08.05.08 (red lying

diamonds). Clearly the particle time of flight was found to be constant over the measurement period, thus allowing the analysis of the PToF-data with one set of fit parameters.

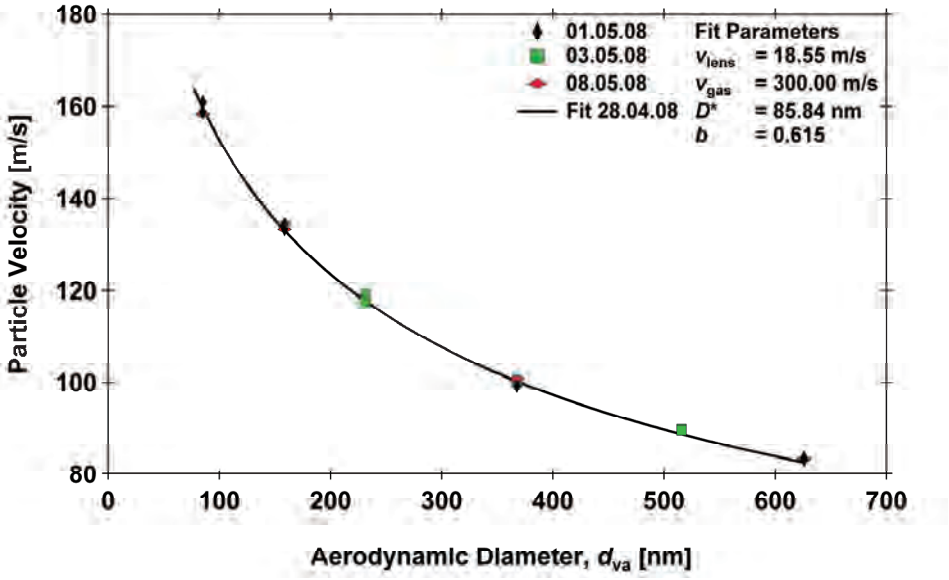


Figure 2.3 Fit curve from size calibration measurements performed on 28.04.08 (black line) and data determined from calibrations on 01.05.08 (black diamonds), 03.05.08 (green squares), and 08.05.08 (red diamonds).

Another quantity that needs to be determined for quantitative measurements with the AMS is the so called Collection Efficiency (*CE*, equation (2.2)), which is of high importance when inter-instrumental comparisons are performed. The *CE* is a unit less quantity, which accounts for the difference between aerosol mass entering the instrument and the detected mass with respect to the actual. The *CE* of the AMS can be determined by parallel measurement with another particle detecting instrument like a SMPS. In case of the AMS the overall *CE* depends on the particle's vacuum aerodynamic diameter ($d_{va}$) and is composed of three parts [*Huffman et al.*, 2005].

$$CE(d_{va}) = E_L(d_{va}) \times E_S(d_{va}) \times E_b(d_{va}) \quad \textbf{(2.5)}$$

$E_L(d_{va})$ represents the effect of the Liu-type aerodynamic lens [*Liu et al.*, 1995a; b; *Liu et al.*, 2007] on the collection efficiency. $E_S(d_{va})$ represents the effect of particle shape and $E_b(d_{va})$ the effect of particle phase, i.e. the probability of the particle to bounce off the

vaporizer prior to total evaporation. In practice, the *CE* is highly sensitive to the physical state of the particles. While the *CE* of waxy to liquid particles ranges from 0.9 to 1.0, solid particles can have a *CE* of less than 0.25. The physical state of the particles is not only a question of ambient humidity but also of composition. The investigation of laboratory generated dried and internally mixed ammonium nitrate and ammonium sulfate aerosol particles showed changing *CE* depending on the particle composition [*Matthew et al.*, 2008]. The *CE* ranged from 0.3 for pure ammonium sulfate to 1.0 for pure ammonium nitrate. The *CE* was constantly around 0.3 for ammonium nitrate mass fractions below 50%. From this point the *CE* increased constantly with increasing ammonium nitrate ratio to 1.0.

A *CE* dependence on particle composition was also found in field measurements [*Crosier et al.*, 2007; *Quinn et al.*, 2006]. Crosier evaluated the following formula:

$$CE = 0.975 - \left( \frac{SO_4^{-2}}{SO_4^{-2} + NO_3^{-1}} \right) \cdot 0.582 . \qquad \textbf{(2.6)}$$

Opposite to the laboratory results of constant *CE* for ammonium sulfate dominated particles, the *CE* in Crosier's equation increases constantly from 0.4 for pure ammonium sulfate to 1.0 for pure ammonium nitrate particles. A constant *CE* of 0.5 is commonly used for field measurement datasets [*Drewnick et al.*, 2004; *Drewnick et al.*, 2007; *Hogrefe et al.*, 2004].

Within the present work, a *CE* was determined for the field dataset presented in chapter 5. By comparison of the AMS measurements to the results of a collocated SMPS in May 2008 a *CE* dependence on the nitrate concentration of the particles was found.

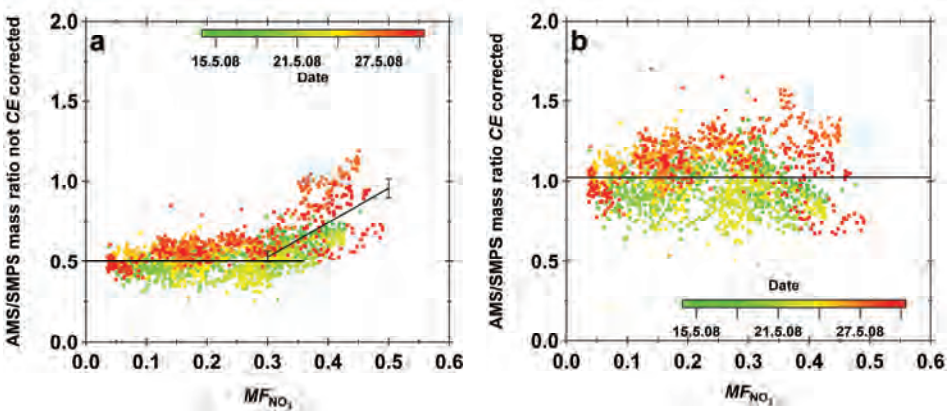


Figure 2.4 AMS/SMPS mass ratio before (a) and after (b) *CE* application as function of nitrate mass fraction ($MF_{NO3}$). The color code refers to measurement date and time.

Figure 2.4 shows the effect of the *CE* application to the AMS data in comparison to SMPS results. The ratio of the total particulate mass detected by the AMS to the particulate mass derived from Scanning Mobility Particle Sizer (SMPS) measurements versus the nitrate mass fraction ($MF_{NO3}$) of the particles is presented. The SMPS data was available from 14.05.2008 to 31.05.2008 and this measurement period is reflected by the color coding of the data. The inflection of the AMS/SMPS mass ratio at a $MF_{NO3}$ of 0.3 (Figure 2.4 a) was time independent and comparisons to result of other AMS measurements performed at other locations during that campaign indicate a general *CE* behavior of that kind across Europe [Douglas Worsnop personal communication]. According to the results a constant *CE* of 0.5 was applied to all measurements with a nitrate mass fraction ($MF_{NO3}$) below 0.3 and the *CE* of particles with higher nitrate fractions was calculated according to the following equation:

$$CE = 2.31 \cdot MF_{NO_3} - 0.18 . \qquad \textbf{(2.7)}$$

The overall *CE* application in comparison to the SMPS measurements resulted in a constant ratio of 1.02 ± 0.01 shown in Figure 2.4 b.

## 2.4. Data Acquisition Modes

The AMS can be run in different data acquisition modes [*Jimenez et al.*, 2003]. The three modes of acquisition used in this work are described in the following. Mode one is the standard mass spectrum (MS) mode in which the Q-MS scans the masses from

1 atomic mass unit (amu) to 300 amu with one amu resolution. As already mentioned in the beginning of this chapter, the HR-ToF-AMS does not scan the individual *m*/*z*'s but acquires an entire mass spectrum at every single ion extraction. The single mass spectra are averaged over some period of time defined as saving interval. This mode is used to acquire mass spectra of the bulk aerosol particle phase. The AMS produces two different kinds of mass spectra, open and closed spectra. The open spectrum reflects the entire aerosol stream. To record the closed spectrum, a chopper is placed into the aerosol stream, hindering the particulate phase to be detected. The remaining gas phase and background contaminations are recorded. By subtracting the closed from the open spectrum, a differential spectrum excluding possible internal contaminations can be obtained.

The second measurement mode is the Particle Time-of-Flight (PToF) mode. This mode is used to acquire size resolved data with a detection range spanning from a few nanometers to about 2000 nm. The detection range allows not only the detection of particles but also the detection of gas phase molecules, the so called air beam. The size of a particle is determined by its flight time between entrance into the sizing chamber of the AMS and detection of molecular fragments in the MS. Size distributions of the major inorganic particle components ammonium, nitrate, sulfate and chloride as well as all organic components combined (organics) can be recorded. Opposite to the MS mode, in which the quadrupole scans the masses in general from *m*/*z* 10 to 300, the detected masses have to be preselected in the PToF mode. The major fragments of the components of interest are selected, i.e. *m*/*z* 30 and *m*/*z* 46 for $NO_3$ or *m*/*z* 48 and *m*/*z* 64 for $SO_4$ (Table 2.2). Again, no selection of individual masses needs to be done in case of the HR-ToF-AMS, since all masses are detected simultaneously at every single extraction.

The third mode is the Beam Width Probe (BWP) [*Huffman et al.*, 2005]. When a particle stream exits the aerodynamic lens into the vacuum/particle sizing chamber, it is focused to a beam of approximately 1 mm. Still, Brownian motion and imperfect focusing causes the beam to broaden on its way to the vaporizer due to small radial velocity components. Additional lift forces cause the broadening to be more pronounced for irregularly shaped particles than for spherical particles [*Liu et al.*, 1995b]. By measuring the beam divergence the particles non-sphericity can be determined [*DeCarlo et al.*, 2004]. In the BWP a thin vertical wire of 0.5 mm diameter is placed in front of the vaporizer at different positions. The diameter of the wire is small compared to the diameter of the vaporizer of 3.8 mm. Still, the wire shields the vaporizer partly as it is placed into the aerosol stream. It can be precisely placed at different positions. The aerosol stream has a

radial intensity distribution with its maximum at the center, causing different grades of reduction in signal intensity depending on the position of the BWP wire. A central position results in maximum signal reduction of up to 70 % for spherical particles like 350 nm PSLs.

# 3. Laboratory Experiment - RIE of Water

The water content of an aerosol particle determines its physical and chemical properties to a large extent. Nevertheless direct measurements of particulate water are rarely performed and in many cases indirect measures such as the hygroscopic growth factor are used to infer a particles ability to take up water and act as cloud condensation nuclei (CCN). The water content of a particle determines for example the physical state, i.e. whether a particle is solid or liquid, the refractive index or the potential to act as a chemical reaction vessel. Regarding the significance of water not only for the particle itself but also for the particles climate forcing potency, it is desirable to have an option to directly determine the particle's water content. In order to be able to do so with an AMS the $RIE_{H2O}$, interferences from other compounds, and possible loss processes during particle sampling need to be quantified.

The experimental determination of the relative ionization efficiency of water ($RIE_{H2O}$) in an AMS, which is unknown up to now, will be presented in the following. Three oxalic acid salts with different thermodynamically stable crystal water contents were used for the investigation. The selected oxalates are optimal for the purpose of determining the *RIE* of water since they have a defined crystal water content that does not evaporate upon fast pressure reduction [*Baxter and Lansing*, 2002], thus minimizing the risk of water being lost during sampling. Furthermore, the oxalate ion has a simple fragmentation pattern facilitating a good interpretation of the mass spectra and the mass signal of the oxalate fraction can be used as internal standard. The findings are applied to oxalic acid, an important substance in the atmosphere [*Sun and Ariya*, 2006] and a prominent reference substance in laboratory experiments for CCN research [*Koehler et al.*, 2006].

## 3.1. Set-Up

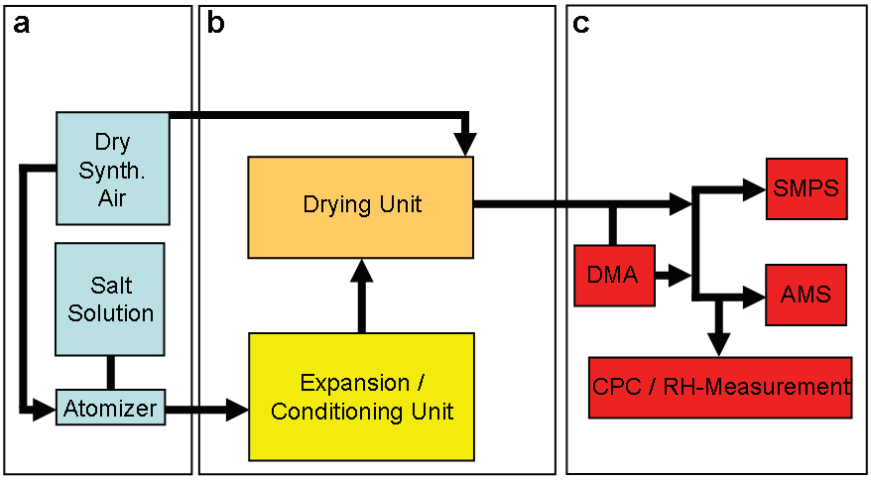


Figure 3.1 Schematic drawing of the experimental set-up: a) aerosol preparation part, b) aerosol conditioning part and c) aerosol analysis part.

The experiments were conducted under controlled laboratory conditions. A TSI 3076 constant output atomizer (Figure 3.1 a) was used to produce the aerosol. It was run with clean filtered synthetic air (Linde, Lipur 6.0), which had a relative humidity (*RH*) of less then 0.2 % at room temperature. To allow the freshly produced particles to coagulate and discharge, the aerosol stream was led into a conditioning unit (Figure 3.1 b). The conditioning unit was a glass tube with a diameter of 12 cm and a length of 24 cm, causing a residence time of about 4 min for the aerosol. Next, the aerosol was led into an expansion/dilution tube from which only parts of the aerosol stream were extracted at a flow rate of approximately 680 mL/min. For drying purposes, the aerosol stream first passed through a drying tube filled with silica gel (Sorbsil C Chamaeleo, dried at 100°C) and then through a Gore-Tex drying tube (Figure 3.1 b). The Gore-Tex was flushed in counter flow (ca. 600 mL/min) with clean and filtered dry synthetic air (*RH* < 0.2 %). The *RH* of the aerosol stream was monitored by a HMP235 Vaisala and never exceeded 0.2 % at the inlet of the analyzing instruments. Stainless steel tubing of 6 mm inner diameter was used to connect the individual parts of the experimental set-up.

The analytical instrumentation consisted of a Condensational Particle Counter (CPC, TSI 3022A), a Scanning Mobility Particle Sizer (SMPS, TSI 3071) and an Aerodyne Quadrupole Aerosol Mass Spectrometer (Q-AMS, [*Jayne et al.*, 2000], Figure 3.1 c). The aerosol particle concentration was measured with the CPC at a flow rate of 300 mL/min. The particle size distribution was measured by the SMPS at an aerosol flow rate of

300 mL/min and a sheath flow of 3 L/min in these experiments. An additional Differential Mobility Analyzer (DMA 3071) was used to size select oxalate particles in some experiments. The chemical composition of the aerosol particles was measured by the Q-AMS. The Q-AMS was run at an aerosol flow rate of 80 mL/min. The standard saving interval for all experiments was 5 min.

## 3.2. Materials and Methods

The salts used to investigate the relative ionization efficiency of water ($RIE_{H2O}$) in an Q-AMS were sodium oxalate ($Na_2(CO_2)_2$, NaOx), potassium oxalate ($K_2(CO_2)_2 \cdot 1H_2O$, KOx) and ammonium oxalate ($(NH_4)_2(CO_2)_2 \cdot 1H_2O$, AmOx). Oxalic acid ($H_2(CO_2)_2 \cdot 2H_2O$, OxAc) was used to apply our findings. All salts were bought from Merck in a purity grade of "puriss. p.a." ≥ 99.9 %. Aqueous solutions of different concentrations were produced in measuring cylinders (1 L, Schott).

MilliQ water of a resistance of 18.2 MΩ and a total organic carbon content (*toc*) of 4-10 ppb was produced in a Millipore apparatus (Gradient A10). The apparatus was fed with high grade de-ionized water. It was observed that the *toc* level within the pure water and the particle concentration after nebulizing pure water could be significantly reduced, if the UV lamp was allowed to run for at least 30 min prior to water withdrawal. Therefore, the UV lamp was lit approximately 1 hour before water withdrawal. All containers were rinsed three times with the solution/water supposed to be stored in there before actual filling.

Each investigation of a single oxalate consisted of two experimental parts. The properties of the background were determined in the first experimental part. The background was defined as mass spectrometric signals originating from the gas phase or particulate impurities. The particulate impurities might be taken up by the clean air by passing through the experimental set-up or by nebulizing the pure MilliQ water. The first experimental part itself consisted of three steps. First step was the investigation of the synthetic air straight from the source. No particulate contaminations could be detected. Second step was the investigation of the air after passing through the entire aerosol preparation system (part a and b in Figure 3.1). Less then 100 particles/cm³ were recorded in these measurements. Third step was the investigation of the aerosol produced by atomizing the pure water, which was used do prepare the actual oxalate solution of interest. The particle concentration and size distribution measurements performed by the SMPS

determined a particle concentration of $10^4$ to $10^5$ particles/cm$^3$ originating from nebulizing pure MilliQ water. All particles were in the size range below 100 nm and the mode diameter was below 14 nm. Since the mode diameter was significantly above 100 nm in all oxalate experiments, contaminations arising from the MilliQ water or the instrumental setup and the background contamination could be neglected in the further analysis.

The second experimental part was the actual analysis of the oxalate particles. The particles shape and compositions were investigated. The Q-AMS was run in the three different data acquisition modes discussed above (chapter 2.4.) First, mass spectra of the entire size distribution were recorded for approximately one hour. Q-AMS saving intervals were 5 min, CPC saving intervals 10 sec and the SMPS recorded the size distribution from 14 nm to 560 nm within 5 min. The CPC and the SMPS were run in parallel to the Q-AMS during all experimental parts. Second, the BWP mode was run to get insights to the particle shape. The wire passed through 7 equidistant positions. In-stream positions were alternated with the out-of-stream starting position. An entire cycle had a duration of 65 min. Five to seven complete cycles were run for each oxalate. Third, PToF measurements of particles were performed. The size resolved measurements were used to derive aerosol particle densities from combined Q-AMS and SMPS measurements.

The mass determination of individual components takes place by application of a fragmentation wave table ([*Allan et al.*, 2004], see chapter 2.2). Several inorganic species, gas phase components, and organics are considered. The fragmentation wave table is based on the fragmentation pattern of the individual species. In our case water, ammonium, and organic were the compounds of interest. The ammonium ion yields ion signal on the mass to charge ratios ($m/z$) 15, 16 and 17. The major fragment is detected on $m/z$ 16. The contribution of ammonium to the signals on $m/z$ 15 and 17 is determined relative to the signal intensity on $m/z$ 16. The water molecule yields ion signal on the mass to charge ratios 16 to 20, with the major signal on $m/z$ 18. The contribution to the other $m/z$'s is determined relative to the major ion signal. Though ammonium and water contribute partly to the total signal on the mass to charge ratios 16 and 17, the two compounds can be separated by the fact of their different major ions and fragmentation patterns. The defined composition and known fragmentation pattern of inorganic species result in a limited amount of ions contributing to the signal on a well known number of mass to charge ratios.

The fragmentation wave table was adapted to the specific object of investigation. The details of this adaptation will be given in chapter 3.3.2.

## 3.3. Results

### 3.3.1. Physical Properties

The physical properties of the oxalate particles were determined to assure that the investigated particles were dry and probably in their thermodynamically stable state and therefore contain the expected amount of crystal water. The particles shapes and densities were used as evidences.

It was important to assure that the particles were absolutely dry under the experimental conditions. Though the *RH* of the overall aerosol stream was below 0.2 % right at the entrance of the Q-AMS, the particles might have enclosed some residual water. If residual water was left in the particles, the detected water amount would not solely depend on the crystal water content of the individual oxalates. Additionally, the particles could keep the spherical shape of the original solution droplets, when their efflorescence is hindered by residual water. As mentioned in chapter 2.4 and 3.1, the BWP is a tool to investigate the shape of aerosol particles.

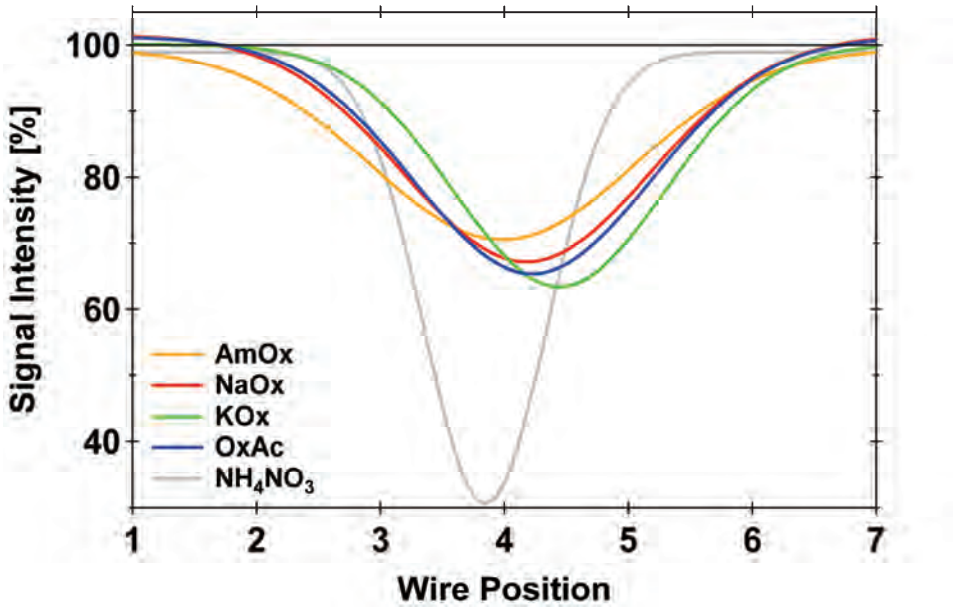


Figure 3.2: Beam Width Probe results for the organic fraction of oxalate particles (colored lines) and $NO_3$ of $NH_4NO_3$ (grey line). Shown is the measured signal intensity as a function of wire position (4 = center position).

The measured signal intensity as function of wire position for the organic fraction of the four oxalates (colored lines) and the nitrate fraction of $NH_4NO_3$ (grey line) is shown in Figure 3.2. The lines represent the Gaussian fit curves determined from the measurements on 7 equidistant wire positions labeled on the x-axis. The single data points are not presented for increased clarity. The full width at half maximum (*FWHM*) gives information on the spericity of the particles. As can be seen, the fit curves representing the organic fraction of the oxalates are very similar but much broader than the fit curve of the nitrate signal detected for $NH_4NO_3$. Ammonium nitrate was chosen as reference since it is a well known AMS calibration substance that encounters a high degree of detectability and focusability [*Jayne et al.*, 2000]. The broad distribution of the oxalate signal with significant contribution at wire positions close to the edge of the vaporizer, indicates that the oxalate particles were not well focused to a narrow beam due to their shape i.e., the particles were not spherical. This in turn is evidence, that the particles were dry. Note, that the shift of minima position along the x-axis is not of scientific significance concerning the shape of particles and is therefore not further discussed.

Particle density was measured to further support that the investigated particles were in their thermodynamically stable state. The effective density ($\rho_{eff}$) of aerosol particles can be determined by parallel measurement of the particle size with an AMS and an SMPS [*DeCarlo et al.*, 2004]:

$$\rho_{eff} = \frac{d_{va}}{d_m}\rho_0 \,. \qquad \textbf{(3.1)}$$

The AMS determines the condensed phase mass and the aerodynamic diameter ($d_{va}$) of the particles. In contrast, the SMPS determines the condensed phase volume and the mobility diameter ($d_m$) of the particles. The ratio of these two diameters multiplied with unity density ($\rho_0$) yields the effective density of the aerosol particles ($\rho_{eff}$). Since $d_{va}$ is not only a function of particle size but also of particle morphology, $\rho_{eff}$ might differ from the bulk components density if the particle is irregularly shaped or bears internal voids. For the four oxalates investigated the densities determined by equation (3.1) were compared to the bulk densities.

Table 3.1: a) Effective densities from combined SMPS ($d_m$) and AMS ($d_{va}$) measurements. b) Measured mass ratios of water to organics and ammonium to organics (chapter 3.3.2). c) Chemical formulas of the substances.

| Oxalate | a) Density [g/cm$^3$] | | | b) Ratio Measured | | c) Formula |
|---|---|---|---|---|---|---|
| | Lit* | Our Data ♣ | Δ [%] | $H_2O$/Org | $NH_4$/Org | |
| NaOx | 2.34 | 2.13 | -9 | -- | -- | $Na_2C_2O_4$ |
| KOx | 2.13 | 2.12 | -0.5 | 0.20 | -- | $K_2C_2O_4 \bullet 1\ H_2O$ |
| AmOx | 1.50 | 1.23 | -18 | 0.20 | 0.39 | $(NH_4)_2C_2O_4 \bullet 1\ H_2O$ |
| OxAc | 1.65 | 1.78 | +8 | 0.16 | 0.09 | $H_2C_2O_4 \bullet 2\ H_2O$ |

*[*Lide*, 2009], ♣In density determinations of dried ammonium sulfate particles of different sizes performed according to the routine presented here, a maximal error of 6 % was found [*Reimer*, 2007].

The results of the density measurements are given in Table 3.1. Comparison to the literature data [*Lide*, 2009] show the largest discrepancy of 18 % for AmOx. The lowest discrepancy of only 0.5 % is found for KOx. NaOx shows a discrepancy of 9 %. Since the *RH* of the aerosol stream was below 0.2 % the particles were believed to be dry and the slightly reduced measured densities to originate either from the non-sphericity of the particles already determined by the BWP. The oxalates under investigation have orthorhombic or monoclinic crystal lattices where either the largest lattice constant is about twice the other two or two lattice constants are about twice as large as the smallest one [*Ahmed and Cruickshank*, 1953; *Jeffrey and Parry*, 1954; *Mielniczek-Brzóska and Sangwal*, 1995]. This enables prolate crystals or oblate structures, respectively, both with shape factors of about 1.1 [*Johnson et al.*, 1987]. On the other hand, we must state that the median deviation of 9 % with respect to the bulk densities is within the uncertainties of this kind of density measurements.

However, the effective density determined for OxAc is higher than the literature value which cannot be explained by the shape factor mentioned above. This topic will be discussed in more detail in chapter 3.3.3.

### 3.3.2. Water Content of Oxalate Particles

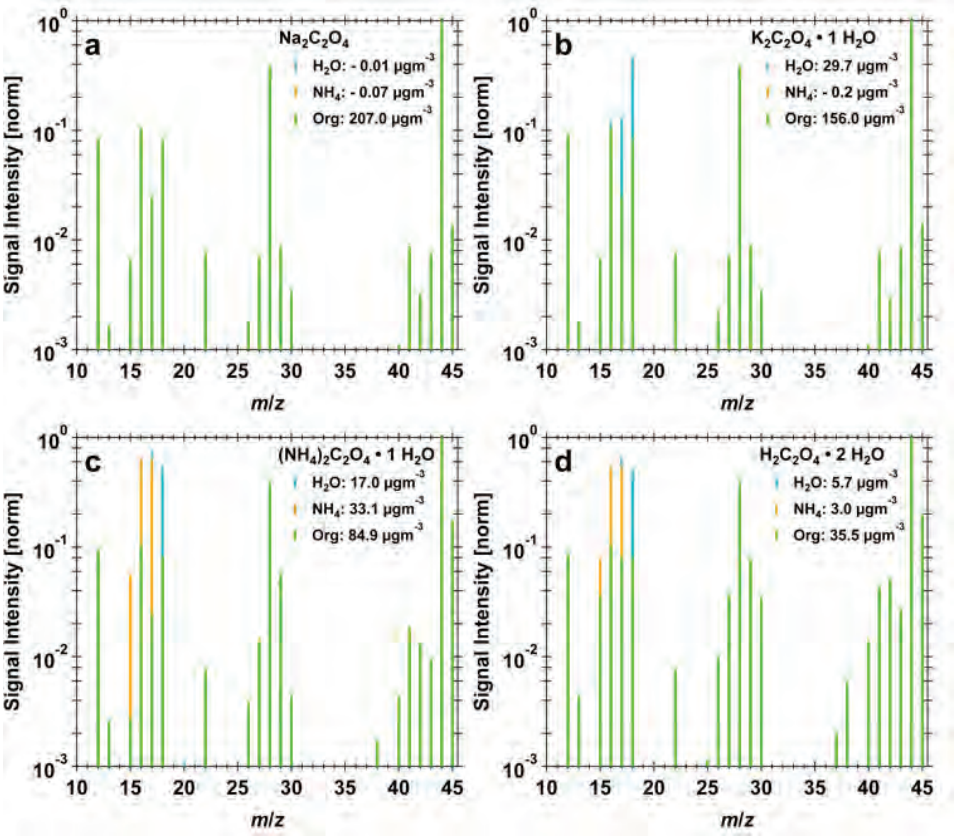


Figure 3.3 Mass spectra and detected mass loadings for (a) sodium oxalate, (b) potassium oxalate, (c) ammonium oxalate and (d) oxalic acid.

Figure 3.3 a to d show the mass spectra of the investigated oxalates at a vaporizer temperature of 600°C. The color coding in the mass spectra reflects the contribution of different components to the signal intensity at the individual mass to charge ratios (*m*/*z*). Organics are green, ammonium is orange and water is blue. The spectra are normalized to the organic signal at *m*/*z* 44.

Sodium oxalate (Figure 3.3 a) contains no crystal water so no particulate water should be detected by the AMS (Table 3.1). The standard fragmentation wave table assumes a relative humidity of about 60 % and denotes an according contribution of gas phase water to the detected background gas phase. Due to the measured *RH* of less than 0.2 % in these experiments, the air fragmentation wave had to be adjusted to yield zero detectable gas phase water. Since no inorganic compound beside sodium is supposed to be

part of the aerosol particles, the organic fragmentation wave was adjusted. All signals beside the ones for water and ammonium were attributed to organics.

In contrast to compounds like organics, ammonium, and water, which can be detected at the standard AMS operating temperature of approximately 600 °C, sodium can only be detected at higher operating temperatures of approximately 900 °C. At temperatures above 700 °C the oven material starts to vaporize. The oven is composed of tungsten and several other metals including sodium and potassium. As a result the detected sodium mass is a mixture of particle and oven material. Consequently, sodium can not be easily detected quantitatively in an AMS. Thus, sodium oxalate contains no internal standard. Nevertheless, it provides a measure to create a fragmentation wave for the organics signal to be expected for oxalates.

Potassium oxalate (Figure 3.3 b) contains one unit of crystal water per molecular unit. The data from these measurements will be used to determine the relative ionization efficiency of water ($RIE_{H2O}$). $RIE_{H2O}$ quantifies the difference of the ionization efficiency of water compared to the ionization efficiency of nitrate ($IE_{NO3}$, chapter 2.3). For a quantification of the water content of particles both $RIE_{H2O}$ and $IE_{NO3}$ need to be taken into account as shown in equation (3.2):

$$C_{H_2O} = \frac{1}{RIE_{H_2O}} \frac{1}{IE_{NO_3}} \frac{1}{CE} \frac{1}{Q} \frac{MW_{H_2O}}{N_A} \sum_{f=18} I_f \ . \qquad \textbf{(3.2)}$$

Based on the chemical structure of potassium oxalate the molar mass ratio of water to organic is $MW(H_2O)/MW(Ox) = 0.20$. The application of the new fragmentation wave table generated for sodium oxalate yields a detected water to organic mass ratio of 0.4 when no $RIE_{H2O}$ is applied. Therefore, the $RIE_{H2O}$ is determined to be 2. The new $RIE_{H2O}$ will be applied to all upcoming analysis. As in the case of sodium, potassium cannot be used as internal standard.

Ammonium oxalate like potassium oxalate contains one unit of crystal water per molecular unit. Ammonium and water were clearly detected and separated by the Q-AMS (Figure 3.3 c). The molar mass ratio of water to organic is $MW(H_2O)/MW(Ox) = 0.20$ and the molar mass ratio of ammonium to organic is $2xMW(NH_4)/MW(Ox) = 0.41$. The detected molar mass ratio of water to organic is 0.20 and of ammonium to organic is 0.39 when the optimized fragmentation wave table and the new $RIE_{H2O}$ are applied.

The substance used to apply our findings from the oxalate salts was oxalic acid. One mol of oxalic acid contains two moles of crystal water. Figure 3.3 d shows the mass

spectrum of oxalic acid. A molar mass ratio of water to organics of only 0.16 is determined instead of the expected ratio of 0.41. Additionally, a significant amount of ammonium is detected. Since the adjusted fragmentation wave table worked well for the three oxalate salts, the detected ammonium signal might arise from a contamination of the oxalic acid. This point is further examined in the upcoming sections.

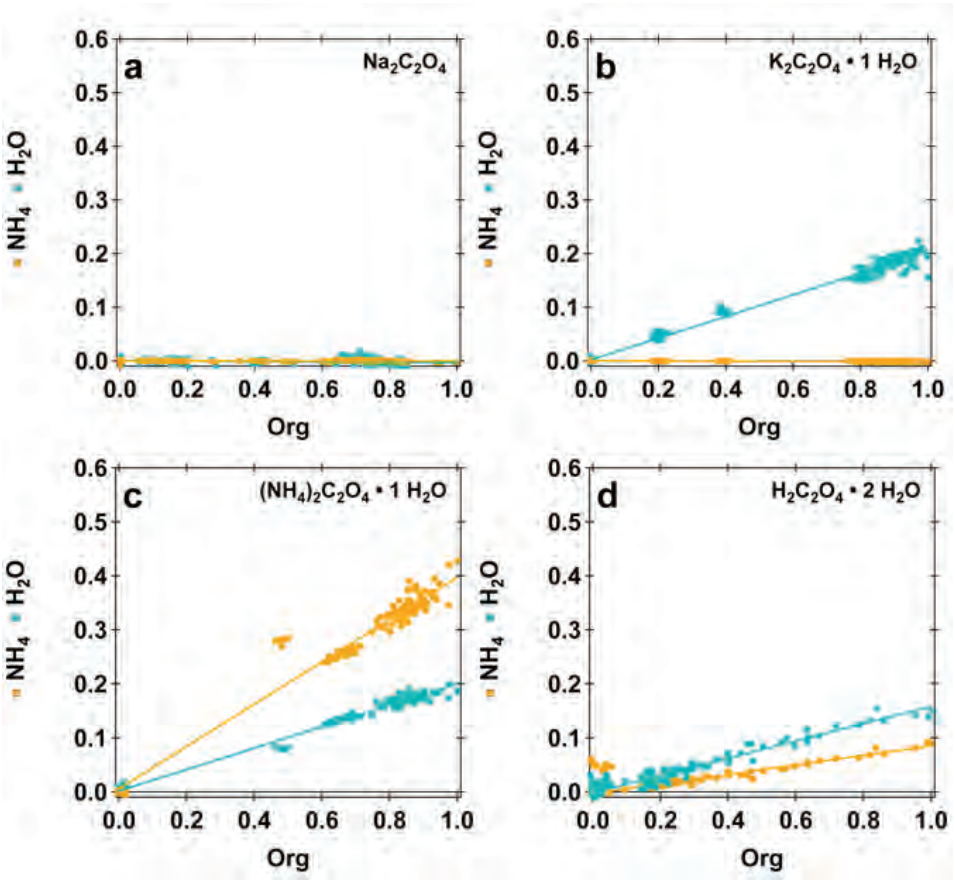


Figure 3.4. Data and fit curves of the correlation of water and ammonium to organic in (a) sodium oxalate, (b) potassium oxalate, (c) ammonium oxalate and (d) oxalic acid normalized to the maximum organic mass.

Figure 3.4 a to d show the ratio of water and ammonium, respectively, to organics. Organics, ammonium, and water mass loadings were divided by the maximal organics mass loading in each experiment to normalize the date and simplify the reading of the ratios. Additionally, linear fit curves through the data are included as guidance of the eye. The data is normalized to the maximum organic mass to investigate, if the ratio depends is mass loading dependent.

The results for NaOx are shown in Figure 3.4 a. Neither water nor ammonium correlate with the organic content of the particles at any mass loading and the concentration of both compounds is zero.

The detected water content correlates with the organics concentration. Figure 3.4 b shows the result for KOx after application of all adjustments. The high coefficient of determination $R^2_{KOx,H2O} = 0.98$ proves the mass independence of this ratio, i.e. constant ratio over the entire mass loading range.

The results of the correlation for AmOx are in agreement with the expected ratios based on the molecular structure of AmOx. Again, high coefficients of determination for both compounds are achieved ($R^2_{AmOx,H2O} = 0.98$, $R^2_{AmOx,NH4} = 0.96$).

In the case of OxAc not only the average mass spectrum but also the correlation analysis point towards a contamination of OxAc by ammonium. A $R^2_{OxAc,H2O} = 0.94$ for water and an even higher one of $R^2_{OxAc,NH4} = 0.98$ for ammonium indicate a mass independent contamination of the oxalic acid solution with ammonium. If the new $RIE_{H2O}$ of 2 is applied, the observed water to organic ratio is only 0.16 (Figure 3.4 d), though a ratio of 0.41 is expected based on the OxAc composition.

### 3.3.3. Analysis of OxAc Contamination

Low molecular weight dicarboxylic acids are water soluble organic compounds (WSOC) that can comprise for a significant fraction of the OM in atmospheric particles [*Sempére and Kawamura*, 1994]. Their impact on the hygroscopic properties of aerosol particles is of major interest [*Yu*, 2000]. Oxalic acid as the most abundant dicarboxylic acid was found in field studies all over the world [*Fisseha et al.*, 2009], [*Kawamura and Sakaguchi*, 1999; *Khwaja*, 1995] and is the preferred compound in CCN laboratory investigations of WSOC [*Peng and Chan*, 2001; *Peng et al.*, 2001; *Prenni et al.*, 2001]. Due to the detected contamination of oxalic acid presented in the previous chapters, further investigations are performed to determine its source.

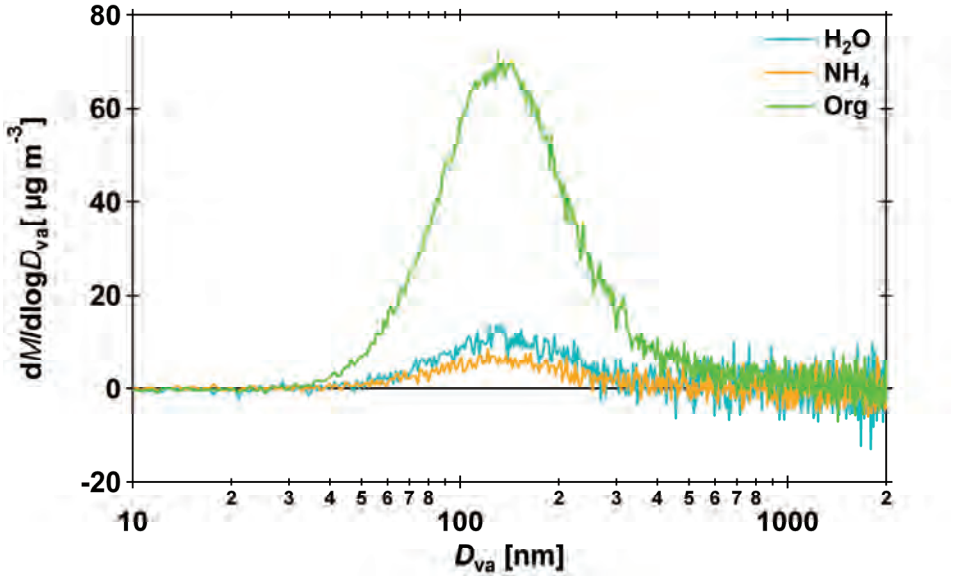


Figure 3.5. Size resolved particle composition of oxalic acid.

Figure 3.5 shows the average mass distribution of water, ammonium and organic of OxAc. The distributions of these three compounds are similar, peaking at the same vacuum aerodynamic particle diameter (134 nm). That means the signals of the different components originate from internally mixed aerosol particles. This finding supports the assumption of an ammonium contamination of OxAc.

The average mass spectrum, the mass dependent analysis, and the size resolved measurements all indicate a contamination of OxAc with ammonium. The Q-MS has the ability to scan a wide range of mass to charge ratios in one amu resolution. Therefore, it is not possible to separate ammonium and water directly with the quadrupole AMS used in the preceding analysis.

A High-Resolution Time-of-Flight Aerosol Mass Spectrometer (Aerodyne HR-ToF AMS [*Canagaratna et al.*, 2007; *Drewnick et al.*, 2005]) was used to get further insights to the exact loadings of water, ammonium and organics in OxAc. The overall set-up of the HR-ToF AMS is identical to the set-up of the Q-AMS. The major difference is the employed mass spectrometer with a resolving power of up to 4000. The HR-ToF AMS allows a clear separation of the ammonium and water signals at the according *m*/*z*'s (Figure 3.6). Shown are the high resolution mass spectra of OxAc (lower panel) and AmOx (upper panel) for comparison.

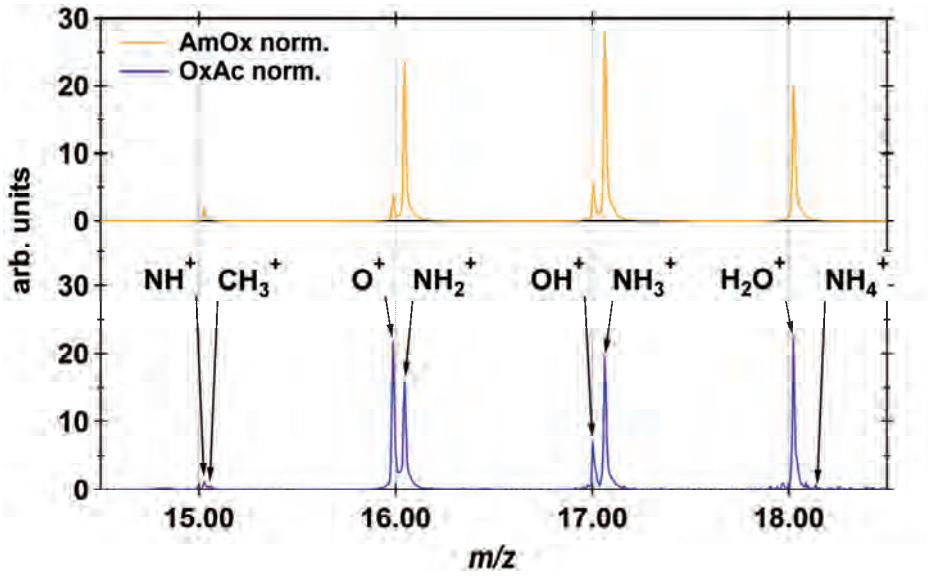


Figure 3.6: High resolution analysis of oxalic acid (lower panel) and ammonium oxalate (upper panel).

A series of experiments shows that even OxAc solutions produced with OxAc taken from factory sealed containers can be contaminated with ammonium. The ammonium contamination increases for both, solid OxAc and OxAc solution after storage for about 1 day in screw cap containers. This means that even the OxAc salt itself absorbs ammonium from the air and partly implements it into its molecular structure, resulting in a molecular mixture of AmOx and OxAc.

Since OxAc implements ammonium from air by unknown processes, the exact composition of different OxAc solutions will differ, depending on the degree of contamination. In our case presented here, an ammonium to oxalate mass ratio of 0.09 and a water to oxalate mass ratio of 0.16 were determined. Assuming a mixture of pure ammonium oxalate and oxalic acid, different rough calculations on the basis of ammonium and water, respectively can be performed to determine the contribution of each compound.

Calculations on the basis of ammonium would result in a 22.5 % contribution of AmOx to the investigated OxAc aerosol particles. Consequently, 77.5 % of the aerosol particles should be OxAc. This assumption would result in a water to organic mass ratio of 0.35, which is about double the amount actually detected.

If the detected water to organic mass ratio is taken as basis for the composition calculations, only 28.75 % of the aerosol particles should originate from OxAc, which in turn demands an ammonium to organic mass ratio of 0.29. This value is more than three times higher than the detected ammonium ratio.

Both calculations point towards a significant water deficit in the investigated aerosol particles. Hence, a mixture of OxAc and AmOx side by side is very unlikely. An explanation for the water deficit can be a ternary mixture of AmOx, the standard di-hydrated OxAc and a crystal water-free OxAc modification. Based on the ammonium and water abundance in the investigated OxAc particles, about 25 % would be AmOx, another 25 % would be the standard OxAc and the remaining 50 % would be the water-free OxAc modification. The water-free OxAc modification has a bulk density of 1.9 g/cm$^3$ [*Lide*, 2009], which is higher than the density of AmOx (1.50 g/cm$^3$) and OxAc (1.65 g/cm$^3$). This approach would also explain the high measured effective density of 1.78 g/cm$^3$ for OxAc particles presented in chapter 3.3.1 The integration of gas phase ammonium or ammonia into the OxAc crystal or solution seems to result in a complex mixed crystal system which potentially will influence the particles ability to take up water and act as CCN.

## 3.4. Summary and Conclusions

Oxalic acid and three of its salts were analyzed with a Quadrupole Aerosol Mass Spectrometer to determine the relative ionization efficiency (*RIE*) of water within this kind of instrument. Knowledge of the *RIE* is the basis for the quantitative determination of a particulate phase species. Due to their simple fragmentation pattern and their defined crystal water content, the sodium, potassium and ammonium salts of oxalate served as ideal substances to investigate this topic. Combined size and mass resolved measurements were performed to determine the effective density of the different aerosol particles, complying with the bulk densities of the substances within 9 %. The aerosol beam divergence was used to investigate the particles morphology. The results confirmed that the particles shape deviated significantly from spheres and in combination with the measured relative humidity of the overall aerosol stream, which was below 0.2 %, dry crystalline particles were assumed in further investigations on.

The *RIE* of particulate water in an AMS was found to be 2. This finding was consistent for the two crystal water containing oxalate salts. The new $RIE_{H2O}$ can always be applied to the detected water signal, since the detection after vaporization and the fragmentation of the water ion is source independent [*Allan et al.*, 2004]. The analysis of oxalic acid revealed a significant contamination of the solid acid as well as its solutions with ammonium incorporated from the gas phase. Application of the new $RIE_{H2O}$ resulted in a water deficit within the molecular structure of the oxalic acid aerosol particles. The

detected water deficit leads to the assumption that a complex mixed crystal system of oxalic acid and ammonium oxalate is formed as soon as oxalic acid is exposed to ammonium or ammonia containing air. Extraordinary diligence in the handling of oxalic acid is required to assure the investigation of pure oxalic acid. The processes leading to the contamination of oxalic acid with ammonium and the degree of contamination depending on the experimental conditions need to be investigated in the future.

For an accurate determination of the water content of atmospheric aerosol particles with an AMS the loss processes in the aerodynamic lens and interferences form other substances must be known and are a topic of further investigations. Still, the knowledge of the correct $RIE_{H2O}$ is already essential for the investigation of the two open questions mentioned above. The new $RIE_{H2O}$ will be applied to field measurement data presented in chapter 5.

# 4. Chamber Study - Organic Nitrate Detection in an AMS

The reaction scheme of BVOC + anthropogenic associated $NO_3$ is another important building block on the way to fully understand secondary organic aerosol (SOA) formation. While gas phase and particulate SOA is dominated by biogenic carbon, SOA formation can be strongly correlated to anthropogenic tracers such as $NO_x$ [*Finlayson-Pitts and Pitts*, 2000]. The contribution of fossil and contemporary carbon to the organic and total carbon budget of aerosols can be determined by radiocarbon analysis ($^{14}C$) [*Weber et al.*, 2007]. The fossil carbon fraction originating from anthropogenic use of fossil energy sources such as fuel, coal, and gas is depleted in the heavy $^{14}C$ isotope compared to contemporary carbon originating from biogenic sources. The contribution of fossil carbon to the total carbon budget can be as low as 0 % in remote areas in the summer time and range up to 50 % in urban areas in the winter time [*Schichtel et al.*, 2008; *Weber et al.*, 2007]. The oxidation of mainly anthropogenic produced $NO_2$ with $O_3$ leads to $NO_3$, hence $NO_3$ can be considered as anthropogenic oxidant. The $NO_3$ oxidation of VOCs is a dominant oxidation and SOA formation pathway in night time chemistry. $NO_3$ causes an even shorter live time of e.g. $\beta$-pinene than OH radicals during day time due to its high average concentration in the night time of about 10 ppt [*Geyer et al.*, 2003] and usually larger rate coefficients with BVOC. Kanakidou et al. [*Kanakidou et al.*, 2005] report a significant gap between measured and modeled global particulate SOA concentrations. The above biogenic - anthropogenic cross reaction might contribute to the closure of that gap but even more explain the high modern carbon content of aerosols and the correlation with anthropogenic tracers.

The connecting link between isolated laboratory experiments and complex field measurements are simulation chamber studies. Laboratory experiment results can be investigated in an up-scaled but controlled environment. Depending on the chamber facilities, conditions close to the real atmosphere in terms of oxidants, VOCs, and particle concentrations can be achieved. Some chambers even allow the investigation of aging processes over several days. The closed and controlled environment reduces the complexity significantly compared to field studies. The type of reactions, the reactivity, the speed, and the degree of the reaction processes can be controlled to a certain level by setting the experimental parameters. Still, not all reactions, pathways, and results that have

been observed in chamber studies so far are fully understood. In other words, the boundary conditions/sources and sinks are known and set, but chamber studies results still reveal an enormous complexity. They are a tool for atmospheric investigation combining an up-scaled laboratory experiment and down-scaled field measurements at the same time.

## 4.1. SAPHIR

The SAPHIR (Simulation of Atmospheric PHoto chemistry In a large Reaction chamber) chamber is an atmospheric simulation chamber, located at the Forschungszentrum Jülich ICG-2. It is a large flourine-ethene-propene (FEP) bag of cylindrical shape with a diameter of 5 m and a length of 18 m resulting in a volume of about 270 $m^3$ (Figure 4.1). The FEP foil has about 85 % light transmission for visible, UV-A and UV-B light so that photolytic production or degradation of substances can be investigated. The chamber is equipped with movable blinds, which can be closed to simulate night time conditions and opened to simulate daytime chemistry including OH radical formation and oxidation. The chamber is operated with high purity (6.0) synthetic air, which allows VOC and oxidants concentration to be as low as a few ppb or even down to ppt concentrations. Its size and the fact that real sunlight can be used for the reactions generate an environment very close to boundary layer of the troposphere.

Figure 4.1 SAPHIR chamber

The chamber is equipped with a wide range of field proven instruments to measure gas and particulate phase components. The instruments of interest in the discussed

experiments are presented in chapter 4.2. Further details on the chamber are given by [*Schlosser et al.*, 2007].

The SAPHIR chamber was the venue of the ACCENT (Atmospheric Composition Change - The European Network of Excellence) $NO_3$-$N_2O_5$ intercomparison workshop in summer 2007. The main idea of this workshop was to compare ten different instruments for $NO_3$ and/or $N_2O_5$ measurement facilitating different measurement techniques [*Dorn et al.*, 2009; *Fuchs et al.*, 2009]. A lot of other interesting topics could be investigated within that framework. SOA formation from the reaction of BVOC with $NO_3$ was investigated [*Fry et al.*, 2009; *Rollins et al.*, 2009] and the mass spectrometric results will be presented in the following.

## 4.2. Experiments

The $NO_3$ oxidation of isoprene, limonene and $\beta$-pinene (Table 4.1) was investigated during the ACCENT $NO_3$-$N_2O_5$ inter-comparison workshop. Isoprene is the most abundant non-methane BVOC in the atmosphere with a production rate of about 550 Tg C/a. [*Guenther et al.*, 2006]. Therefore isoprene comprises almost 50 % of the total global non-methane BVOC (~1150 Tg C/a) [*Guenther et al.*, 1995]. Limonene and $\beta$-pinene are among the most abundant BVOC within the group of monoterpenes, which account for about 11 % of the non-methane BVOCs. Furthermore, both limonene and b-pinene are fully described by the Master Chemical Mechanism (MCM v3, [*Saunders et al.*, 2003]) allowing for a good comparison of the experimental results with theory.

Table 4.1 Molecular structure of limonene, isoprene, and $\beta$-pinene.

| isoprene | limonene | $\beta$-pinene |
|---|---|---|
| 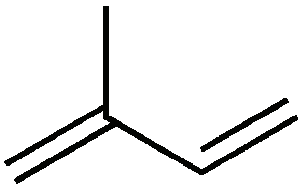 | 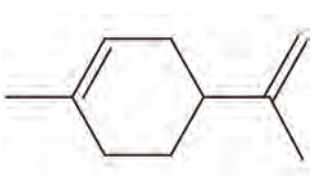 | 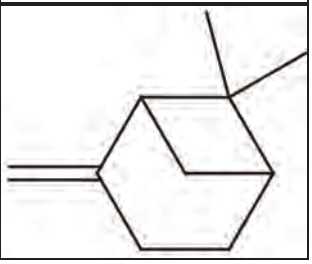 |

The production and composition of particulate SOA was investigated in 4 separate experiments while the concentration of several gas phase components was monitored. Gas

phase $NO_3$ concentrations presented here were measured by a Pulsed Cavity Ring-Down Spectrometer (PulsedCRDS, [*Dubé et al.*, 2006]). Since, this campaign was aimed to compare different $NO_3/N_2O_5$ instruments and measurement techniques, $NO_3$ concentration was determined by several instrument. The results of the individual instruments agreed well [*Dorn et al.*, 2009]. $O_3$ and VOC concentrations were also measured by more than one instrument, and again the results agreed well. Therefore, only these instruments, which data was used for the upcoming analysis are presented here. The $O_3$ concentration was measured by chemiluminescence (ECO Physics CLD AL 700, [*Ridley et al.*, 1992]) and the VOC concentrations were measured by Proton Transfer Reaction Mass Spectrometry (PTR-MS, [*Lindinger et al.*, 1998]). The total gas and particulate phase alkyl nitrate concentration was determined by $NO_2$-Thermal Dissociation - Laser Induced Fluorescence ($NO_2$-TD-LIF, [*Day et al.*, 2002; *Day et al.*, 2009]) by detection of $NO_2$ from the stepwise dissociation of peroxynitrates, alkyl and multifunctional nitrates, and nitric acid. The $NO_2$-TD-LIF is equipped with four ovens operating at different temperatures (ambient temperature, 180 °C, 350 °C and 600 °C). Total dissociation of gaseous and semivolatile aerosol phase nitrates is expected [*Fry et al.*, 2009]. Aerosol particle properties were measured by an SMPS, a CPC, and a High-Resolution Time of Flight Aerosol Mass Spectrometer (HR-ToF AMS) [*Canagaratna et al.*, 2007; *Jayne et al.*, 2000].

The $NO_3$ oxidation of the three BVOCs was performed in four separate experiments (see Table 4.2 for details). One experiment was the oxidation of limonene under dry condition with two BVOC additions. The particles generated during the first limonene oxidation served as organic seed particles when limonene was added 8.5 h after the first injection. The same holds for the isoprene experiment, since isoprene was also added twice with more then 8.5 h between both injections. Additionally, $(NH_4)_2SO_4$ seed aerosol particles were introduced into the chamber 54 min before the first isoprene injection. The relative humidity was set to 57 % for this experiment. Two $\beta$-pinene experiments were performed; one in dry conditions and one at 50 % *RH*. $\beta$-pinene was only added once in both experiments and no inorganic seed particles were used. The actual oxidant $NO_3$ was produced according to equation (1.1 a). In case of a $NO_3$ depletion, $N_2O_5$ decomposes and serves as an additional $NO_3$ source (equation (1.1 b)). The detailed list of BVOC and oxidant additions for the four experiments is given in Table 4.2 a) to d).

Table 4.2 a-c: Experiment progression. Amount in ppbv and time of BVOC and oxidant addition in hours. The first BVOC addition is set to be 0:00.

| a) limonene | | | |
|---|---|---|---|
| Δ time | BVOC [ppbv] | $NO_2$ [ppbv] | $O_3$ [ppbv] |
| -0:06 | | 30 | |
| 0:00 | 20 | | |
| 2:16 | | 8 | |
| 2:23 | | | 40 |
| 8:17 | | | 40 |
| 8:22 | | 20 | |
| 8:31 | 20 | | |

| b) isoprene | | | |
|---|---|---|---|
| Δ time | BVOC [ppbv] | $NO_2$ [ppbv] | $O_3$ [ppbv] |
| -0:40 | | 8 | |
| 0:00 | 10 | | |
| 1:08 | | 16 | |
| 1:10 | | | 38 |
| 6:41 | | 16 | |
| 6:54 | | | 30 |
| 8:32 | 10 | | |

| c) $\beta$-pinene (dry) | | | |
|---|---|---|---|
| Δ time | BVOC [ppbv] | $NO_2$ [ppbv] | $O_3$ [ppbv] |
| -2:42 | | 80 | |
| -2:19 | | | 15 |
| -0:30 | | | 80 |
| 0:00 | 15 | | |

Table 4.2 d: Experiment progression. Amount in ppbv and time of BVOC and oxidant addition continued.

| d) $\beta$-pinene (humid) | | | |
|---|---|---|---|
| $\Delta$ time | BVOC [ppbv] | $NO_2$ [ppbv] | $O_3$ [ppbv] |
| -4:11 | | | 160 |
| -3:59 | | 1 | |
| -1:10 | | 80 | |
| 0:58 | | | 90 |
| 0:00 | 15 | | |

## 4.3. Results

Additional to the information in Table 4.2, the experiments are presented in the graphs a) to d) of Figure 4.2. Prior to and after every experiment the chamber was flushed with clean and dry synthetic air over night. A dew point temperature of -55 °C, a $NO_x$ concentration of less then 50 pptv, and an $O_3$ concentration of less then 0.5 ppbv were achieved. Gas phase measurements are shown in the top ($NO_2$, light blue upright triangles, and $O_3$, black stars) and middle panel (BVOC, yellow diamonds, and $NO_3$, blue squares) of the graphs. The first BVOC addition time is always labeled as 0:00. The lower panels show the time evolution of different particulate components. The particulate total (black), organic (green), and nitrate (blue) aerosol mass concentrations measured by the AMS are given as solid lines. Also presented by red dots is the total gas and semivolatile particulate alky nitrate concentration measured by the $NO_2$-TD-LIF.

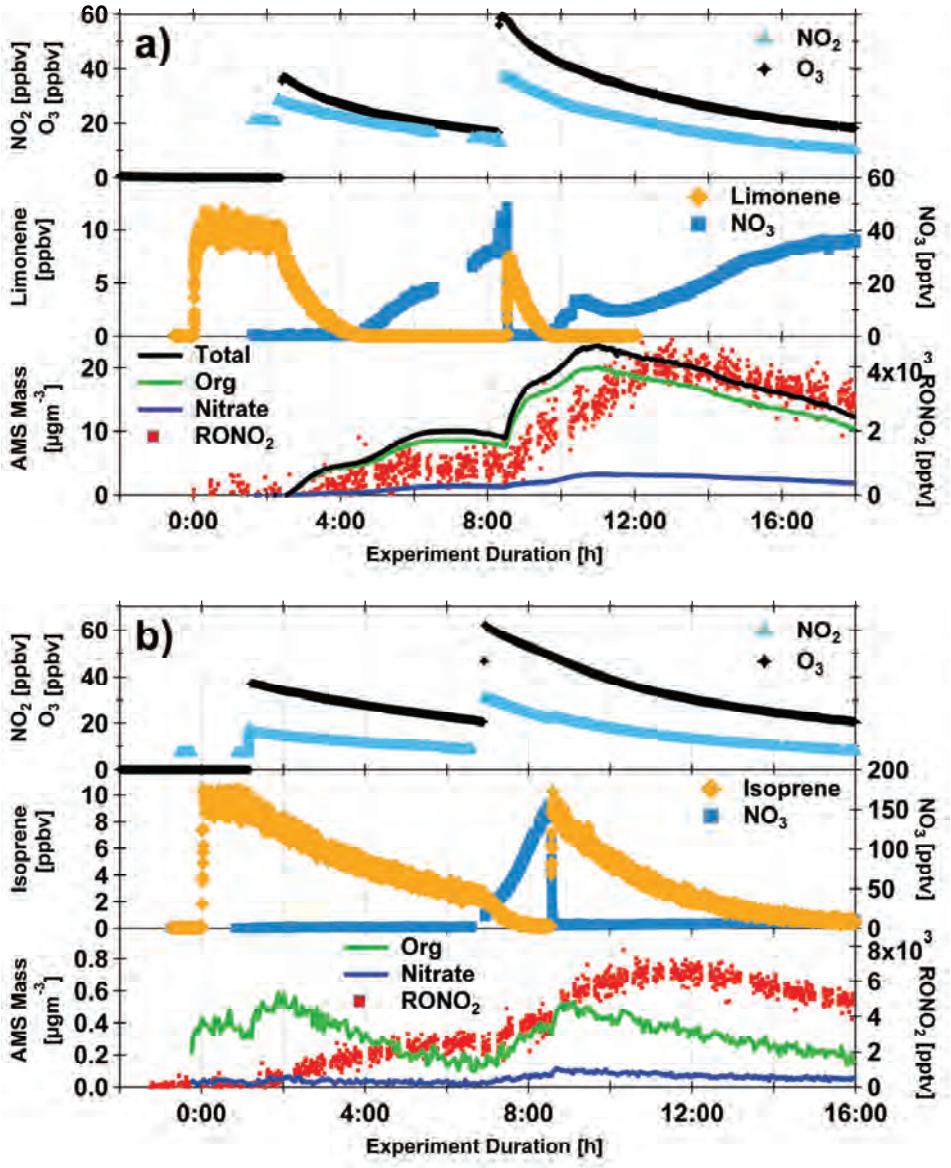


Figure 4.2 a-bTime series of $NO_3$ oxidation experiment of limonene (a) and isoprene (b). Top panel in both graphs: $NO_2$ (light blue triangles) and $O_3$ (black stars) concentrations. Middle panel graph a: Gas phase $NO_3$ (blue squares) and limonene concentration (yellow diamonds). Middle panel in graph b: Gas phase $NO_3$ (blue squares) and isoprene concentration (yellow diamonds). Bottom panel in both graphs: Total aerosol (black line, only in a), particulate organic (green) and nitrate mass (blue line), and total alky nitrate concentration (red dots).

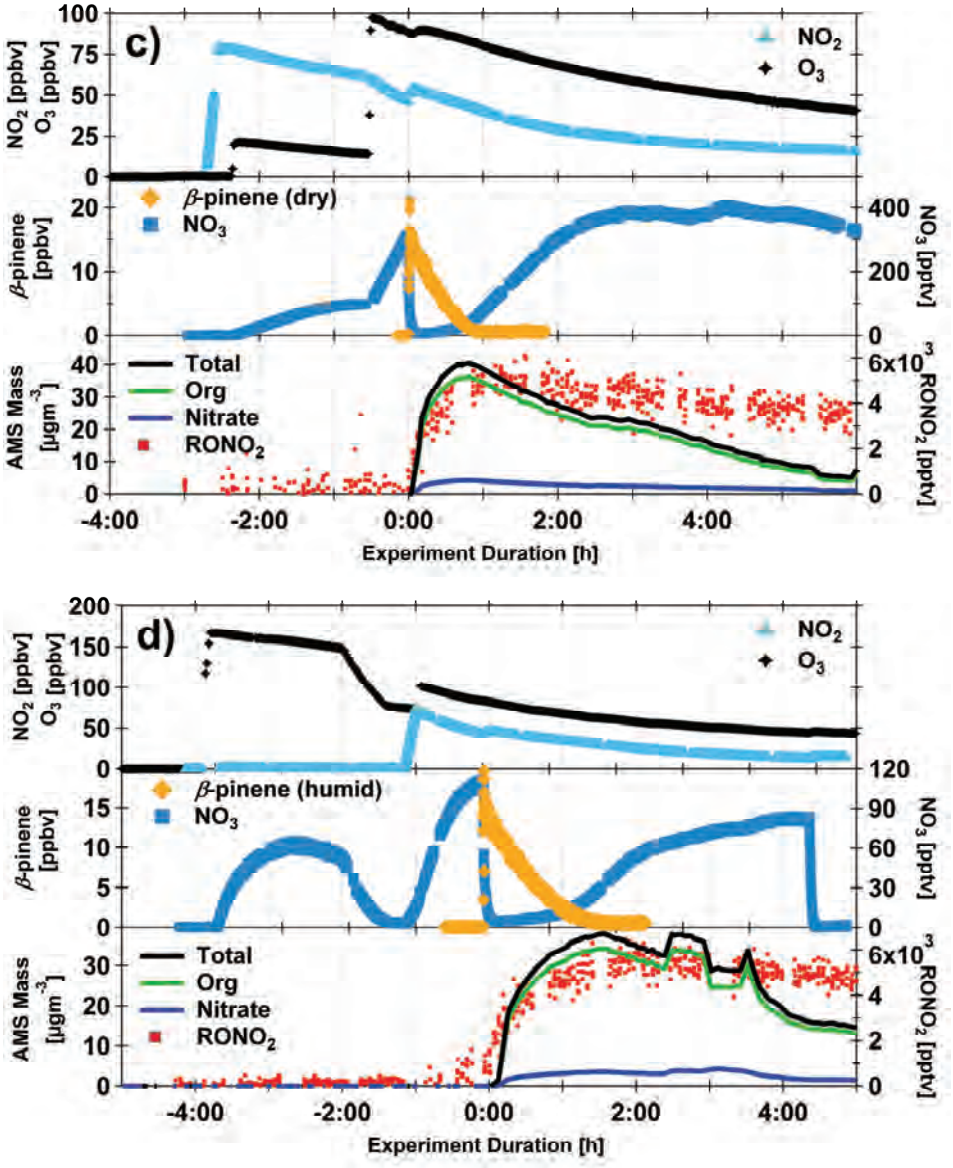


Figure 4.2 c-dTime series of $NO_3$ oxidation experiment of $\beta$-pinene dry (c) and humid (d). Top panel in both graphs: $NO_2$ (light blue triangles) and $O_3$ (black stars) concentrations. Middle panel in both graphs: Gas phase $NO_3$ (blue squares) and $\beta$-pinene concentration (yellow diamonds). Bottom panel in both graphs: Total aerosol (black line), particulate organic (green) and nitrate mass (blue line), and total alky nitrate concentration (red dots).

The average particulate SOA mass yields ($Y$, equation (4.1)) ranged from 10 % for isoprene up to 50 % for both $\beta$-pinene experiments:

$$\frac{\Delta\text{SOA mass}}{\Delta\text{BVOC mass}} = Y \,. \qquad \textbf{(4.1)}$$

Here, ΔSOA is the measured in SOA mass loading and ΔBVOC the total reacted BVOC. The mass yield of limonene + $NO_3$ was found to depend sharply on the existence of seed particles. While the mass yield was only 25 % in the absence of seed particles, *Y* was 85 % in the presence of seed particles [*Fry et al.*, in preparation]. Different yields were also observed for the isoprene experiment depending on the degree of oxidation. The degree of oxidation was called first generation, if only one double bond was oxidized and second generation, when both double bonds were oxidized (see Table 4.1). *Y* of the first generation products was < 0.7 %, while *Y* of the second generation products was 14 % [*Rollins et al.*, 2009]. The mass yield in both *β*-pinene experiments was ~50 % indicating the independence of the particle formation from the *RH*.

For isoprene and limonene, which both have two double bonds (Table 4.1), the results indicate that mainly second order oxidation products are the components which actually nucleate/condensate. The products resulting from the oxidation of the first double bond seem to be too volatile to condensate. A significant condensation of SOA products can only be observed after the oxidation of both double bonds, here called second order oxidation [*Rollins et al.*, 2009]. The particle formation in both *β*-pinene experiments was prompt after the VOC addition to the reaction chamber (Figure 4.2 c and d). That indicates vapor pressures of the first order oxidation products to be low enough to promote nucleation and particle growth [*Fry et al.*, 2009].

The AMS analysis of the experiments revealed two interesting facts. First, the here investigated organic nitrates have a higher vapor pressure than the other particulate secondary organic components produced during the reactions (chapter 4.3.1). Second, the fragmentation pattern of organic nitrate differs significantly from the fragmentation pattern of nitrate from $NH_4NO_3$ (chapter 4.3.2).

### 4.3.1. Vapor Pressure of Organic Nitrates

The only particulate species detected in the AMS analysis of all BVOC-$NO_3$ oxidation experiments were organics and nitrate. No ammonium, sulfate or chloride could be detected except for the isoprene experiment, when $(NH_4)_2SO_4$ was added as seed particles. This result was expected since the experiments were conducted in the controlled environment of the SAPHIR chamber.

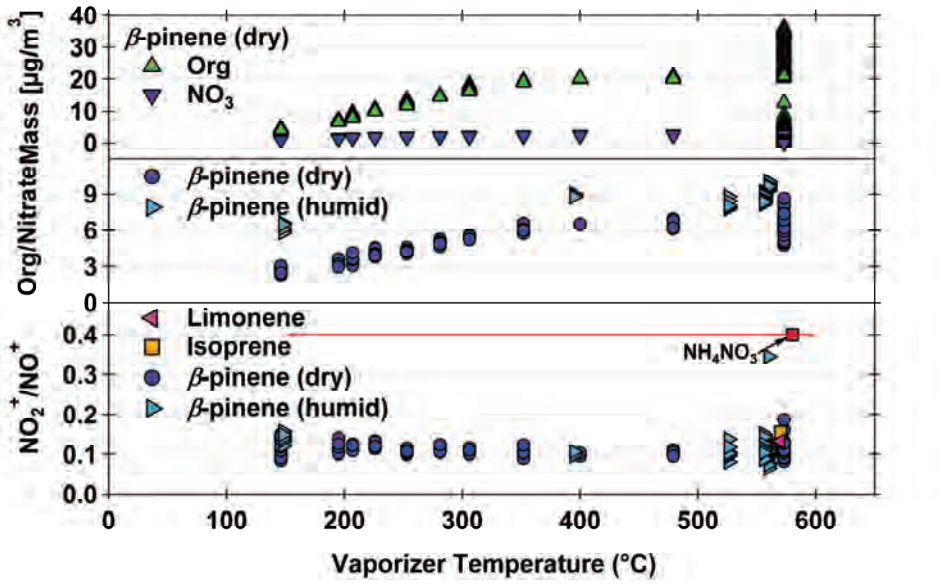


Figure 4.3 Mass of detected organics and nitrate (top panel), ratio of particulate organic to nitrate (middle panel), and fragmentation ratio of particulate nitrate into $NO_2^+$ and $NO^+$ (bottom panel) vs. vaporizer temperature

The vaporizer temperature was modulated in the two β-pinene experiments to investigate the temperature dependence of different compounds within the particulate aerosol phase. The temperature was decreased stepwise from 580 °C to 150 °C and towards the end of the experiment raised again to 580 °C. The high temperatures at the end of the experiment were applied to ensure, that the findings were due to the thermogramm and not due to aging processes in the chemical composition of the aerosol particles. Figure 4.3 (upper panel) shows detected organic (green upright triangles) and nitrate (blue downwards triangles) mass in dependence of the vaporizer temperature for the dry β-pinene experiment. The detected mass of both species decreases with decreasing vaporizer temperature. The detected organic mass decreases significantly below 350 °C. Further insight can be gained from the detected organic to nitrate mass ratio. A clear temperature dependence of that ratio can be seen for temperatures below 350 °C (Figure 4.3 middle panel). No significant difference can be observed between the dry (dark blue dots) and the humid (light blue rightwards triangles) β-pinene experiment. The ratio is constant for temperatures above 350 °C and decreases significantly for temperatures below this 350 °C. The ratio went up to the starting value when the temperature was raised back to 580°C at the end of the experiments. That means that at lower temperatures the nitrate containing fraction is more efficiently vaporized and therefore more efficiently detected

than the average organic fraction of the particles. Derived vapor pressures and molecular masses of organic nitrates are given in [*Fry et al.*, 2009] and [*Rollins et al.*, 2009] and in [*Fry et al.*, in preparation]

Table 4.3 Table of organic nitrate species molecular weight (*MW*) and vapor pressures ($p_{vap}$) inferred from the measurements. Also given are atmospheric lifetimes of the respective BVOC in the presence of the major atmospheric oxidants (taken from [*Atkinson and Arey*, 2003])

| Experiment | *MW* [g/mole] | $p_{vap}$ [Pa] | atmos. lifetime for reaction with* | | |
|---|---|---|---|---|---|
| | | | $NO_3$ | $O_3$ | OH |
| Limonene | - | - | 5 min | 2.0 h | 49 min |
| Isoprene | 226 | $5 - 10 \cdot 10^{-5}$ | 1.6 h | 1.3 d | 1.4 h |
| $\beta$-pinene dry | 229 | $5.33 \cdot 10^{-4}$ | 27 min | 1.1 d | 1.8 h |
| $\beta$-pinene humid | 215 - 231 | $6.67 \cdot 10^{-4}$ | 27 min | 1.1 d | 1.8 h |

Organic nitrates seem to have a higher vapor pressure, easily evaporating even at low temperatures like 150 °C without any changes in composition. This finding is supported by the temperature independence of the nitrate fragmentation ratio. The ratio is constant over the entire temperature range of the vaporizer investigated in these experiments (bottom panel in Figure 4.3), indicating that the evaporating nitrate containing fraction does not change in composition, but the composition of the entire organic fraction changes. That means that the remaining detected organic fraction is depleted by low volatile components.

The amount of organic nitrate in the particulate phase was estimated in two ways for the $\beta$-pinene experiments. Both are based on the assumption that organic nitrates were the only detected species at the lowest AMS vaporizer temperature (145 °C). In the first approach the molecular weights of these species were inferred based on the AMS measured ratio of organics to nitrate and the nitrate molecular weight (*MW* = 62 g/mole) Using the derived molecular weight of 215 g/mole- 231 g/mole a contribution of 32 % - 41 % of organic nitrates to the total aerosol mass was obtained. In the second approach, the ratio of mass measured by the AMS to mass derived from SMPS measurements calculated for the time period during which the AMS vaporizer temperature was set to 145 °C. The mass from SMPS measurements was derived by transferring size into volume distributions and multiplication of the resulting volume with a density of 1.6 g/cm$^3$. The density was determined by parallel mass (AMS) and size (SMPS) distribution measurements as

described in chapter 3.3.1. With the underlying assumption that the AMS measured organic nitrate only while the SMPS detected the total SOA in this period, the organic nitrate mass fraction was determined to be 39 %, well in agreement with the first approach.

### 4.3.2. Nitrate Fragmentation Ratio

The major fragments of the nitrate ion detected in the AMS are $NO_2^+$ on *m*/*z* 46 and $NO^+$ on *m*/*z* 30. The parenting $NO_3^+$ ion on *m*/*z* 62 is almost not existent due to the vaporizing/ionizing scheme of the AMS. Opposite to the water ion, which fragmentation pattern is independent of its origin (vapor, particulate phase or product of decomposition) [*Allan et al.*, 2004], the fragmentation of the nitrate ion is known to depend on the nitrate origin [*Alfarra*, 2004]. Nitrate originating from ammonium nitrate has an average $NO_2^+/NO^+$ ratio of about 0.40 (red square in the bottom panel of Figure 4.3 and red line Figure 4.4) as determined in independent measurements of $NH_4NO_3$.

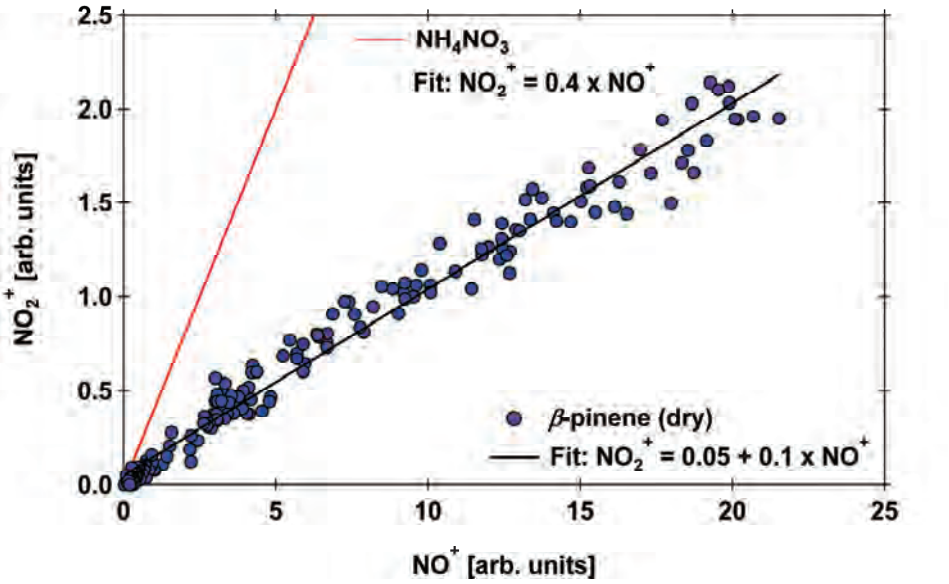


Figure 4.4 $NO_2^+$ versus $NO^+$ signal intensity for $NO_3$ from $NH_4NO_3$ (red line) and from high resolution analysis of the dry $\beta$-pinene experiment (blue dots).

Opposite to this, we found a ratio of about 0.1 for organic nitrate in all BVOC-$NO_3$ oxidation experiments [*Fry et al.*, 2009; *Fry et al.*, in preparation; *Rollins et al.*, 2009], which was independent from the BVOC and the operating temperature of the vaporizer (bottom panel of Figure 4.3). The $NO_2^+/NO^+$ ratio is also presented in Figure 4.4. The red line represents the average ratio for $NH_4NO_3$. Also shown is data from high resolution

mass spectrometric analysis of the dry $\beta$-pinene experiment (blue dots). The ratio according to the applied linear fit (black line) is 0.1. The resolving power of the ToF AMS allows to clearly separating the ion peaks of interest from neighboring signals on the same nominal mass (Figure 4.5 a and b).

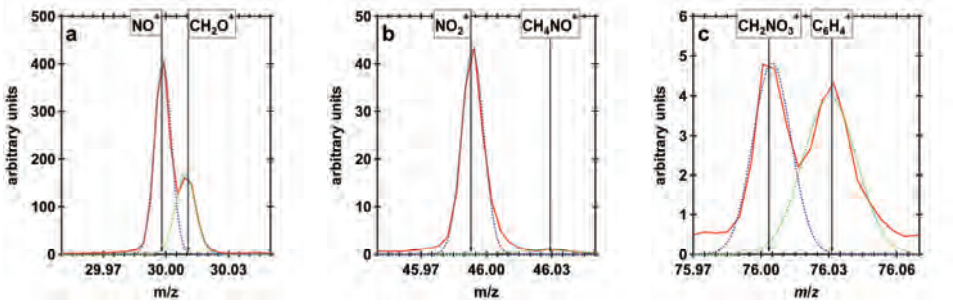


Figure 4.5 Ions in a high resolution mass spectrum at *m*/z 30, 46 and 76 from the dry $\beta$-pinene $NO_3$ oxidation experiment.

The nitrate fragmentation ratio ($NO_2^+/NO^+$) within an AMS can be used as a tool to detect organic nitrate in ambient measurements [*Alfarra et al.*, 2006; *Allan et al.*, 2006; *Drewnick et al.*, 2007]. In addition to a lowered ratio compared to the ratio of inorganic nitrate from $NH_4NO_3$ for example, further analysis and/or additional measurements are needed. High resolution analysis could be performed to determine the existence of nitrate containing organics e.g. on *m*/z 76 (Figure 4.5 c) or accompanying measurements of other instruments can be used to determine the abundance of other inorganic nitrate containing compounds like $NaNO_3$ or $Mg(NO_3)_2$. Depending on the combination of analytical methods, it might be even possible to determine the percentage of nitrate containing organics form the overall fragmentation ratio.

## 4.4. Summary and Conclusions

The oxidation of BVOC by an anthropogenic associated oxidant was investigated by means of $NO_3$ reaction with isoprene, limonene, and $\beta$-pinene, respectively in an atmospheric simulation chamber. The data obtained by AMS and NO2-TD-LIF measurements were used to gain insights to the formation and the properties of organic nitrates. The analysis of thermogramm measurements, achieved by modulation of the AMS vaporizer temperature, revealed a higher vapor pressure of organic nitrates than pure organics produced in the same reaction. A $NO_2^+/NO^+$ ratio of 0.1 was determined for

organic nitrate from high resolution analysis of the nitrate fragmentation pattern. This value is significantly lower than the ratio of 0.4 which is found for nitrate originating from $NH_4NO_3$, the atmospherically most abundant nitrate compound. Both findings were independent of BVOC and *RH* conditions. The contribution of organic nitrates to the total particulate mass was estimated to be 32 % - 41 % for both $\beta$-pinene experiments. The specific fragmentation ratio of organic nitrate will be applied to ambient measurement to detect and investigate the abundance of organic nitrate in the atmosphere (chapter 5.5).

# 5. Ambient Measurements at Cabauw, NL

Two large field studies were accomplished during spring 2008 and winter 2009. In both cases, mass spectrometric measurements were performed within a network of several AMS' located all over Europe (Figure 5.1). Measurements were taken from 28th of April to 30th of May in 2008 as part of the European Integrated project on Aerosol Cloud Climate and Air Quality Interactions (EUCAARI, [*Kulmala et al.*, 2009]) Intensive Measurement Period (IOP). The second measurement period extended from 24th of February to 25th of March 2009 within the framework of the European Monitoring and Evaluation Programme (EMEP).

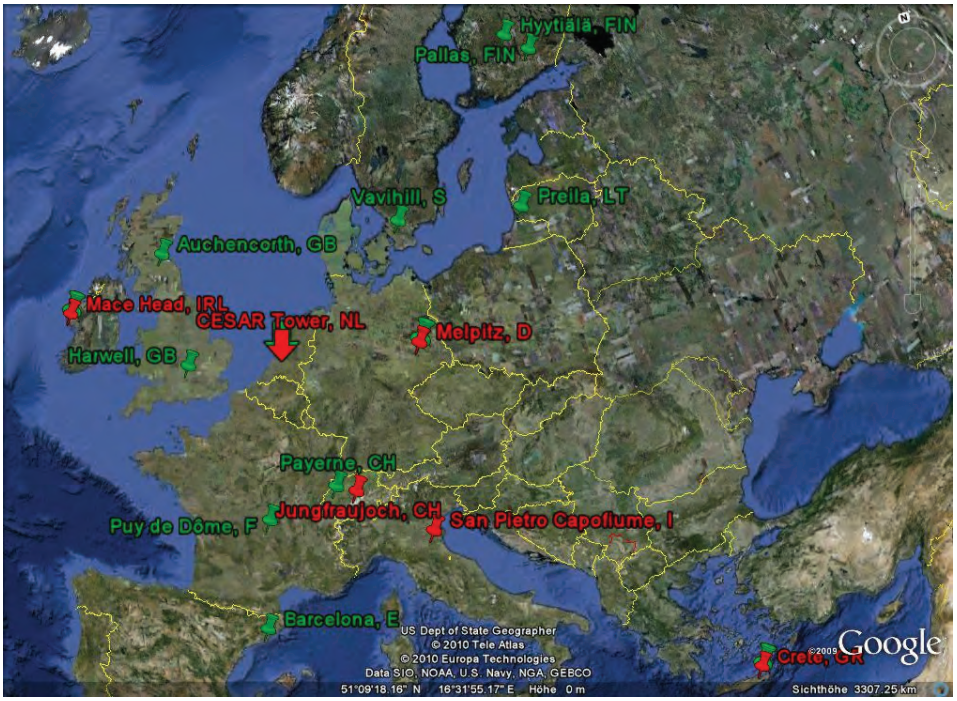


Figure 5.1 Network of AMS' over Europe for EUCCARI (2008, red) and EMEP (2009, green) campaigns.

## 5.1. Cabauw - CESAR Tower

The AMS measurements were performed at the Cabauw Experimental Site for Atmospheric Research (CESAR) Tower, The Netherlands. The tower is located in the center of the Netherlands on a grass land in Lopik, close to the city of Cabauw. Lopik is

about 20 km south-west of Utrecht and about 50 km south of Amsterdam. The geographic coordinates are lat. 51° 57'N, long. 4° 54' E, altitude -0.7 m a.s.l. The measurement site is representative for North West Europe and features continental and maritime conditions, depending of the wind direction. The plain geography of the Netherlands and especially in the area of Cabauw reduces ambiguities in terms of air parcel convection and turbulences.

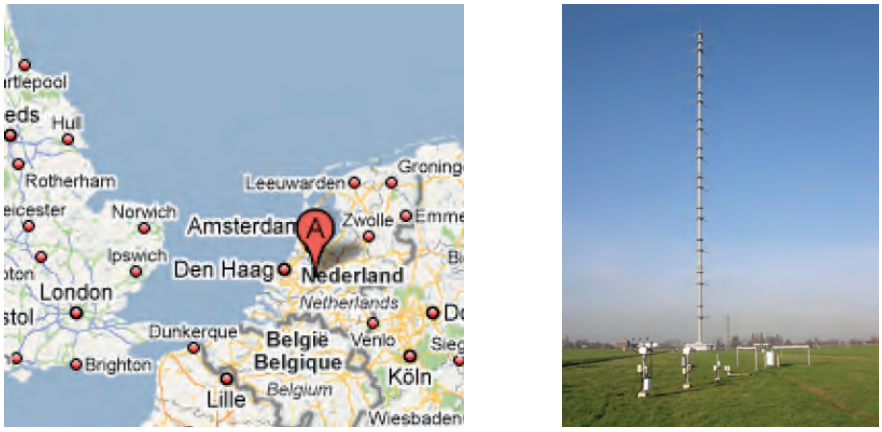


Figure 5.2 Location of CESAR Tower in map and picture of CESAR Tower.

The CESAR tower is run by the Royal Netherlands Meteorological Institute (KNMI), De Bilt, The Netherlands. It is equipped with standard measurement devices for outside temperature, dew point temperature, wind direction and speed at 200 m, 140 m, 80 m, 40 m, 20 m, 10 m, and 2 m height. Beside this, precipitation, cloud cover and height, radiation and a range of remote sensing, flux and concentration measurements of Green House Gases (GHG) are continuously performed [*Russchenberg et al.*, 2005].

The AMS was located in the basement of CESAR tower and connected to the main sampling line designed and installed for optimum aerosol particle measurements during the Intensive Measurement Period At Cabauw Tower (IMPACT) campaign. The sampling line consisted of stainless steal and had an outer diameter of ½" (= 1.27 cm). It was connected to an inlet at 60 m and ended in a manifold in the basement. The entire distance between tower inlet at 60 m height and AMS inlet was about 70 m. The aerosol stream was dried by two Naphion dryers at the tower inlet at 60 m and information on the temperature and relative humidity (*RH*) were recorded (Table 5.2). An aerosol flow rate of about 680 ml/min between manifold and AMS inlet was achieved by parallel sampling of the AMS (80 ml/min) and a water CPC (600 ml/min). 6 mm outer diameter stainless steel tubing was used to connect the manifold with a Swagelock cross in front of the AMS inlet.

Standard data acquisition included average mass spectra in V- and W-mode (chapter 2.4). Size distribution data was only acquired in V-mode, because the aerosol particulate loading was too low to get a good signal to noise ratio in W-mode. V- and W-mode were alternated and saved every five minutes. The vaporizer temperature was set to about 580 °C throughout both sampling periods. The AMS was run on remote control to enable permanent control of the instrument performance. Size and ionization efficiency calibrations were performed once a week and filter measurements were performed to determine the gas phase background signal (chapter 2.3).

In 2008 air was sampled through one HEPA filter for about half an hour after size and *IE* calibration. Two HEPA filters in a row were used to reduce the average particle loading controlled by the CPC during filter measurement from about 20 particles/cm$^3$ in 2008 to 0 particles/cm$^3$ in 2009. Additionally, an electronic 4-port valve was used to allow for automated filter sampling by remote controlled valve switching. Therefore, filter measurements could be performed at least every second day. The filter sampling time ranged from 15 to 20 min, to ensure that one entire V- and W-mode measurement were included and to minimize interruption of ambient measurements.

Due to the fact that CESAR tower is a permanent monitoring site and the campaigns were conducted European wide a whole range of instruments were collocated and even airborne measurements were performed. Only the instruments which data will be presented here are listed in Table 5.1

Table 5.1 Table of collocated instruments at CESAR Tower which data will be presented within this work.

| Instrument | Inlet Height | Aerosol Phase | Type of data | Operator |
|---|---|---|---|---|
| SMPS (3034) | 60 m | Particle | Size Distribution | TNO |
| MARGA/ MARGA Sizer♣ | 4 m | Gas + Particle | Mass Loading of Inorganic Species | ECN |
| MAAP (5012) | | Particle | Black Carbon | TNO |

♣only 2008

## 5.2. Measurement Results

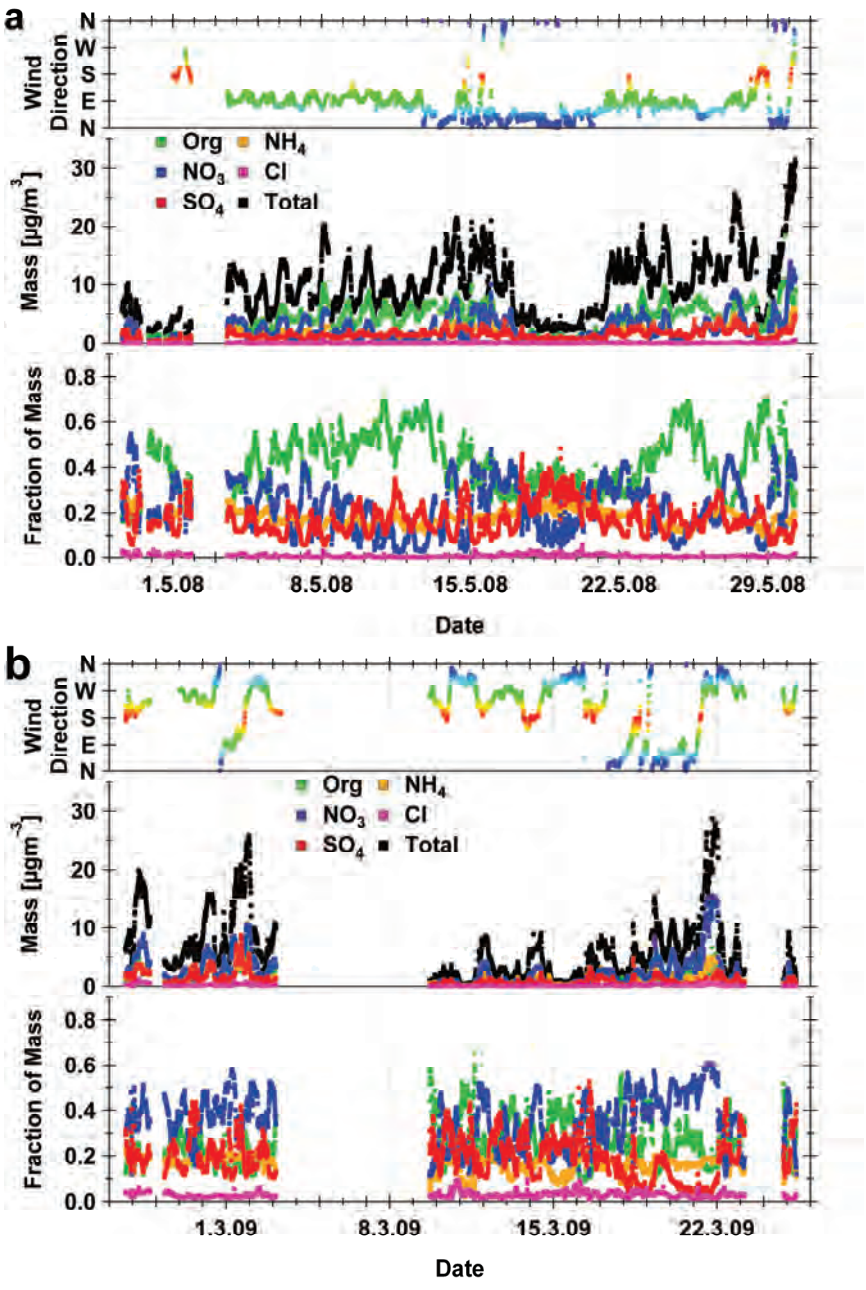


Figure 5.3 Campaign overview on the measurements from May 2008 (a) and March 2009 (b). Top panel in both graphs: Wind directions measured at 40 m height of the tower. Middle panel: Time series of AMS organic (Org), ammonium ($NH_4$), nitrate ($NO_3$), sulfate ($SO_4$), chloride (Cl) and total (Total) mass. Bottom panel in both graphs: Time series of the fractional abundance of the individual species.

Figure 5.3 shows the time series of the major components organics (Org, green), ammonium ($NH_4$, orange), nitrate ($NO_3$, blue), sulfate ($SO_4$, red) and chloride (Cl, pink). The sum (Total) of these species is additionally shown in black. The top graph (a) presents data from May 2008 and the bottom graph (b) data from March 2009. Gaps in the time series are due to instrument failure (2.5.08: lightning stroke the measurement tower, 3.5. – 9.5.2009: mass spectrometer problems (power supply)) or instrument maintenance, calibrations, or filter measurements.

The 2008 measurement period was dominated by easterly and south-easterly wind directions (top panel in Figure 5.3 a) transporting air masses from Eastern and Central Europe to the measurement site. This situation was disrupted from 17. – 20.05 by northerly winds transporting low mass loadings (< 5 µg/m$^3$) of aerosol due to precipitation scavenging from the North Sea. Though not reflected in the local wind profile, the meteorological background was dominated by long range transport of Sahara dust from North Africa from 29$^{th}$ of May on [Roelofs et al., in preparation]. The particulate aerosol mass loading reached maximum concentrations of more than 30 µg/m$^3$ during this period. Opposite to 2008, the measurement period in 2009 was dominated by westerly winds (top panel in Figure 5.3 b), almost uniformly covering the entire range from South to North. Only on 29$^{th}$ of February and in the period from 17.03.2009 to 21.03.2009 easterly winds predominantly north-easterly winds were present.

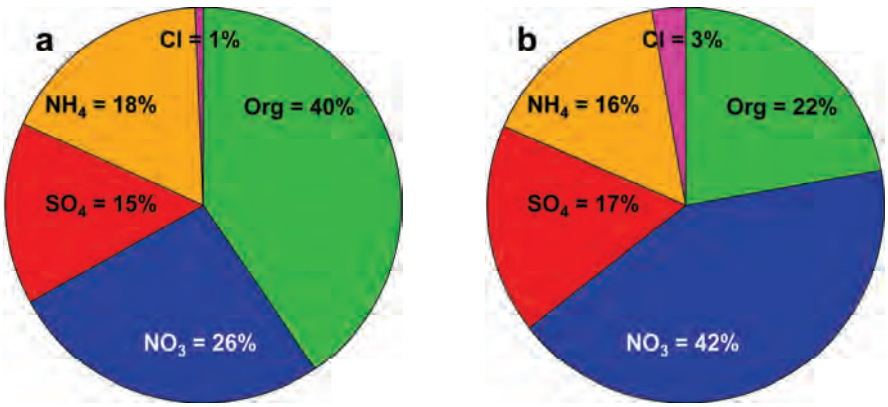


Figure 5.4 Pie charts of the average contribution of the individual species in (a) 2008 and (b) 2009.

The contributions of the individual species to the total mass are shown over time in the bottom panels of Figure 5.3 a and b and as campaign averages in Figure 5.4 a and b. Average particle concentrations of 9.72 µg/m$^3$ and 5.62 µg/m$^3$ were detected in 2008 and 2009, respectively. As can be seen, the Spring/Summer 2008 was dominated by organic,

while the winter 2009 was on average dominated by nitrate. Especially in 2008 a pronounced anti correlated fractional abundances of sulfate and nitrate was noticeable. The scavenged background situation was characterized by a high fractional abundance of sulfate and a very low fractional abundance of nitrate all over the period. The Sahara dust period towards end of May 2008 was dominated by a high nitrate contribution.

Table 5.2 Table of temperature [°C] and relative humidity [%] measured in the sampling line in 2008 and 2009.

| Year | *T* [°C] | | | *RH* [%] | | |
|---|---|---|---|---|---|---|
| | min. | max. | ave. | min. | max. | ave. |
| 2008 | 22.7 | 29.4 | 26.5 | 12.7 | 42.2 | 23.1 |
| 2009 | 16.5 | 22.4 | 18.5 | 23.2 | 57.4 | 37.3 |

*RH* and temperature were measured by a Vaisala (HMP 235) that was placed into the aerosol stream of the parallel sampling CPC close to the inlet of the AMS in 2008. This data reflects the actual temperature and *RH* of the aerosol stream in the basement. In 2009 temperature and *RH* data were collected by TNO (Built Environment and Geosciences Airquality & Climate, Uetrecht, The Netherlands) measured with a similar Vaisala at the tower inlet at 60 m height. Due to a positive temperature gradient between 60 m inlet and basement, the *RH* values are upper limits and the temperature values are lower limits in 2009 (Table 5.2).

Figure 5.5 shows the detected particulate water (lower panel) as well as the *RH* and temperature (upper panel) for the measurement campaigns in 2008 (a) and 2009 (b) at CESAR tower. In both years, the aerosol stream was dried by two naphion dryers at the inlet at 60 m height. Therefore, the reported *RH* values do not reflect the ambient *RH*. The *RH* time series were incorporated into the fragmentation wave of water in the fragmentation wave table (chapter 2.3) to apply a time dependent correction of the interfering signal contribution from gas phase water (*RH*) to the total water signal detected by the AMS. Furthermore, the new relative ionization efficiency of water ($RIE_{H2O}$) as determined in chapter 3 was applied. Due to the set-up of the AMS with an aerodynamic lens as inlet and the vacuum ($10^{-3}$ Pa) in the particle sizing chamber, semi-volatile components can be lost prior to their detection. Therefore, the reported water amounts must be considered as residual water that did not evaporate in the inlet and/or the sizing

chamber. The average detected residual water in 2008 was 0.64 µg/m$^3$ and 0.31 µg/m$^3$ in 2009. These amounts correspond to 6.6 % and 5.5 % of the average particulate mass reported for the corresponding year.

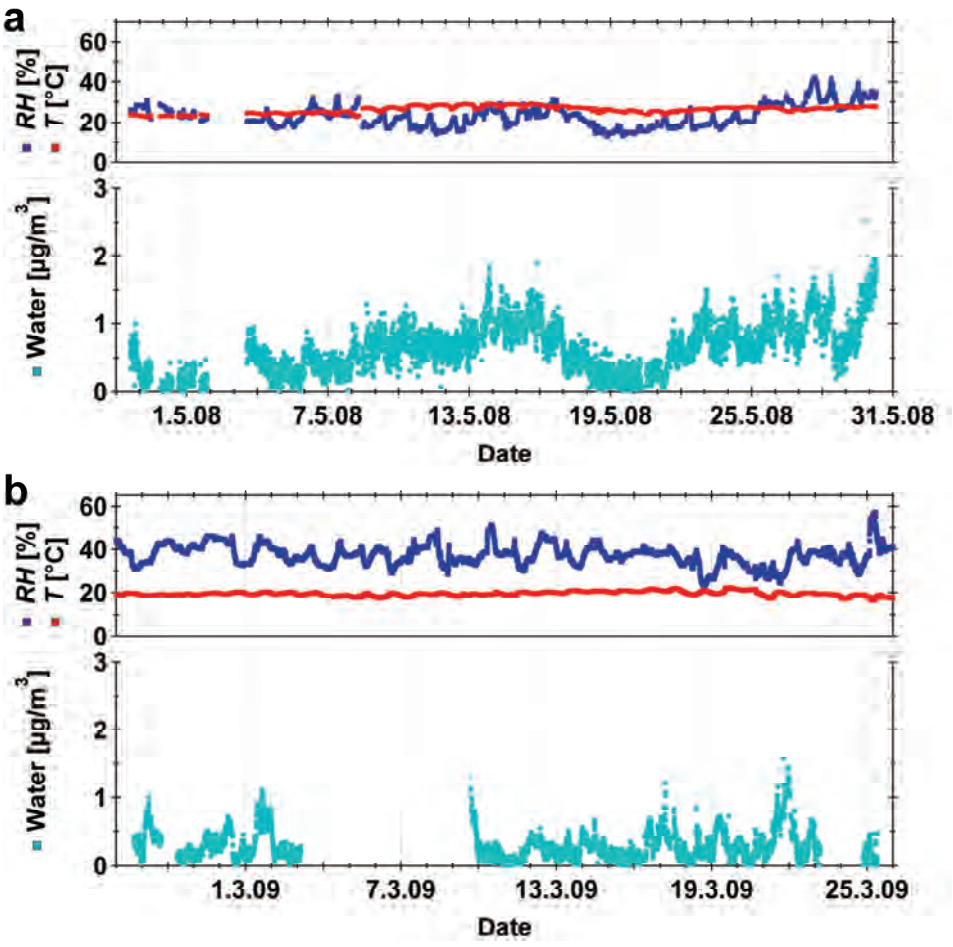


Figure 5.5 Particulate water detected by the AMS (bottom panel) and relative humidity and temperature (both top panel) at CESAR tower during the measurement campaigns in 2008 (a) and 2009 (b).

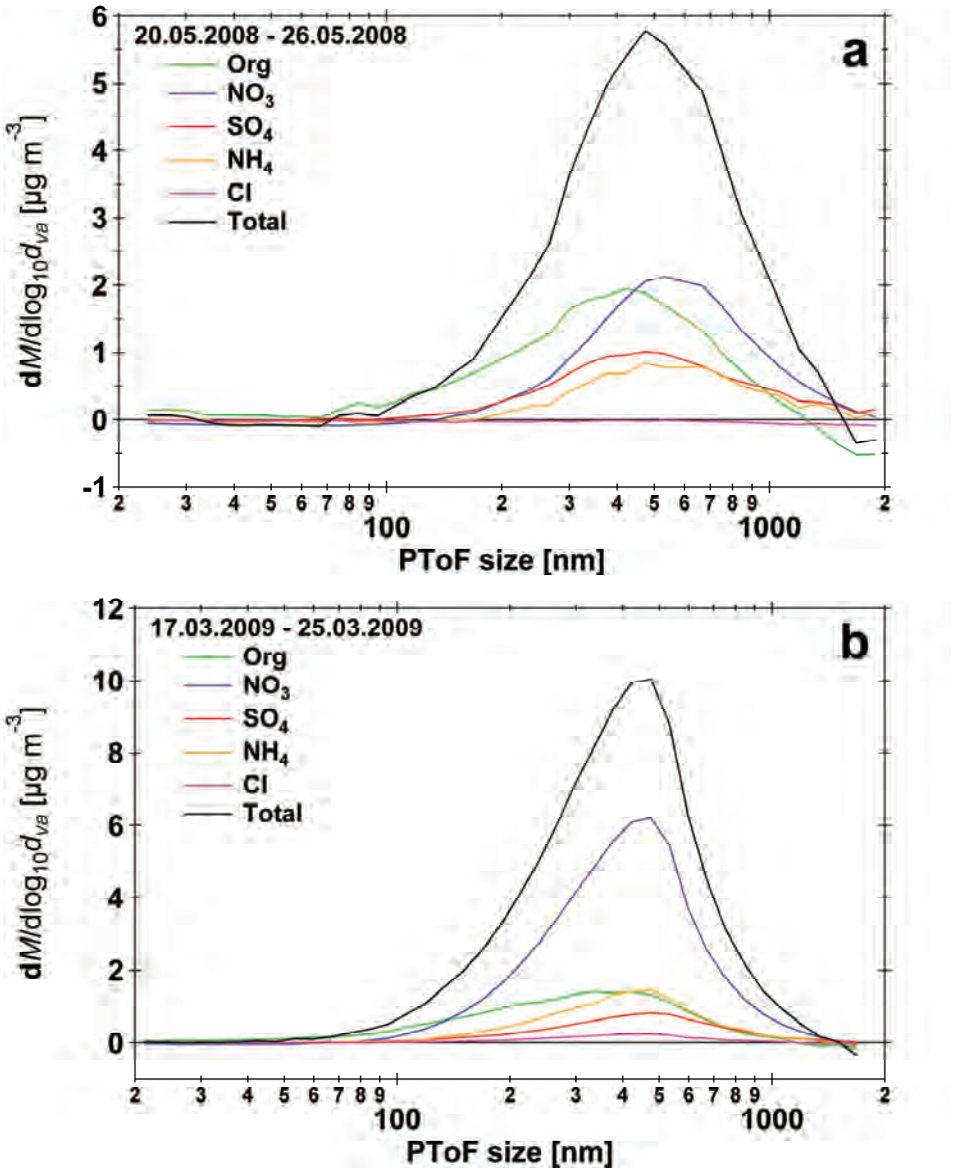


Figure 5.6 Averaged size distributions of the main species for the time period 20.05.2008 to 26.05.2008 (a) and 17.03.2009 to 25.03.2009 (b) measured at Cabauw, NL.

Chemically resolved size distributions as measured with the AMS at CESAR tower in 2008 and 2009 are shown in Figure 5.6 a and b. The averaging period was chosen to present representative measurement conditions. The mode diameter of the total mass (Total, black line) is about 450 nm in both measurement periods. Likewise are the size distributions of the individual species very similar. The inorganic species are

predominately detected in the larger size fraction while organic show a much broader size distribution extending into size fractions below 100 nm.

For details on the data analysis and additional AMS results see Appendix A.1 and A.2.

## 5.3. Instrument Comparisons

### 5.3.1. SMPS

An SMPS (TSI 3034) attached to the same sampling line as the AMS was operated by TNO from 14$^{th}$ of May 2008 to End of May 2008. Size distributions of the particles in the range from 9.36 nm to 515.6 nm diameter were measured separated into 70 $\log_{10}$ equal size bins. From the measured SMPS number distributions the aerosol mass was determined according to the following steps. The number distribution is transferred into a volume distribution which together with information on the particle density obtained by the AMS yields the particle mass. In each measurement interval the fractional abundance of the individual species determined by the AMS was used to calculate the particle density. The mass of ammonium, nitrate, sulfate, and organics accounted on average for 99 % and 97 % of the total particulate mass detected by the AMS in 2008 and 2009, respectively (Figure 5.4). Assumptions on the species sources need to be drawn to actually calculate the density. If no further knowledge on the detailed composition is available, the most likely substances present in atmospheric particles are taken as reference. The density of the particles is then calculated with respect to the bulk densities of the reference substances (Table 5.3).

Table 5.3 Densities used to derive the particulate mass loading from SMPS measurements.

| Compound | Density [g/cm$^3$] |
|---|---|
| $NH_4NO_3$ | 1.72* |
| $(NH_4)_2SO_4$ | 1.77* |
| organics | 1.40$^{\#}$ |
| $Cl^-$ | 1.00$^{\clubsuit}$ |

*[*Lide*, 2009] $^{\#}$[*Hallquist et al.*, 2009] $^{\clubsuit}$[see text for explanation]

The chloride detected in the AMS needs to flash evaporate at a vaporizer temperature of about 600 °C. Hence, the probability that this chloride origins from an inorganic salt is very small. Especially in field campaigns, the source of the detected chloride is hard to determine. We set the density of the remaining chloride fraction to 1 g/cm$^3$ and expect only a minor impact on the average particle density in view of the low fractional abundance of 1 % and 3 %, respectively, in the two measurement periods.

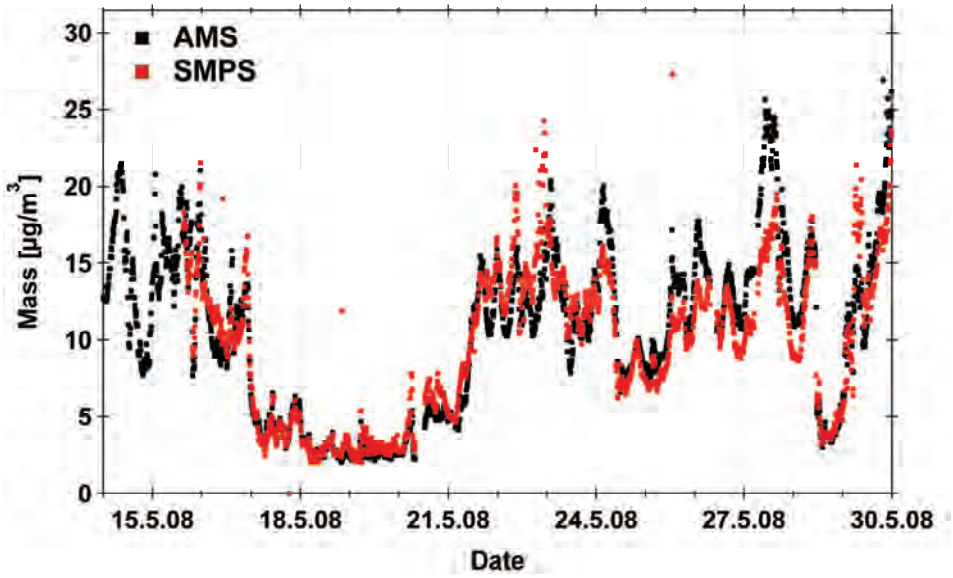


Figure 5.7 Time series of AMS and mass derived from SMPS measurements in 2008.

The chronological sequence of the total particulate mass loading of the AMS (black dots) and the mass loading derived from these SMPS measurements (red dots) is shown in Figure 5.7. The measurements show very good quantitative and qualitative agreement, since even small temporal loading variations are visible in both time series. Correlating the SMPS derived mass to the total AMS mass results in a slope of 0.93 ($R^2$ = 0.87, black solid line, Figure 5.8). The data is colored by time showing a scatter around unity (black dotted line) for almost the entire measurement period. High mass loadings (above 20 µg/m$^3$) were measured during the Sahara dust event. Since dust particles are expected in the coarse particle range (> 1 µm), this event exemplifies the different cut off sizes of SMPS and AMS. While the upper measurement range was 515.6 nm for the SMPS, the AMS is a $PM_1$ instrument. The size distribution of the SMPS data is presented in Appendix A.3.1.

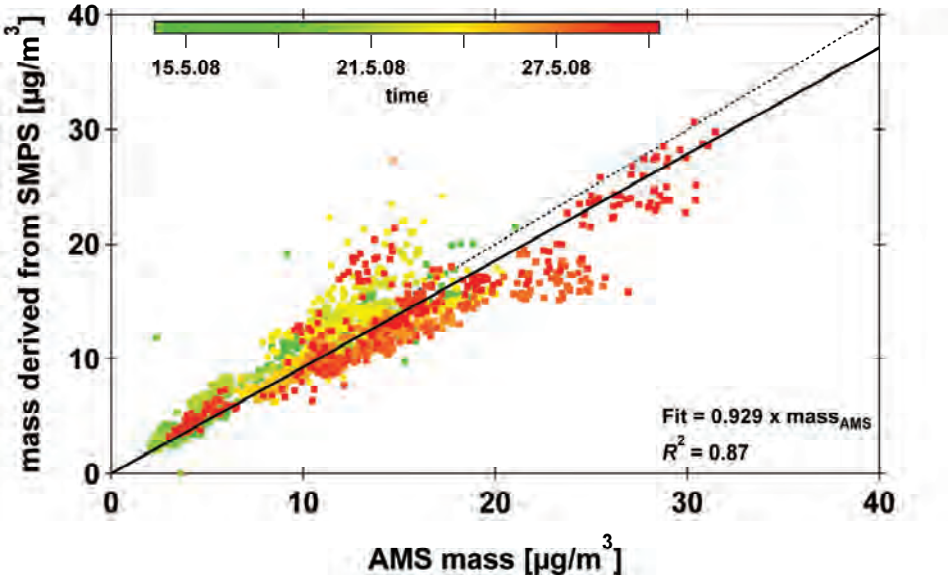


Figure 5.8 Particulate aerosol mass derived from SMPS measurements versus AMS total mass (colored by time) and fit trough the data (black solid line). As a guidance of the eye, unity is indicated (black dotted line).

### 5.3.2. MARGA

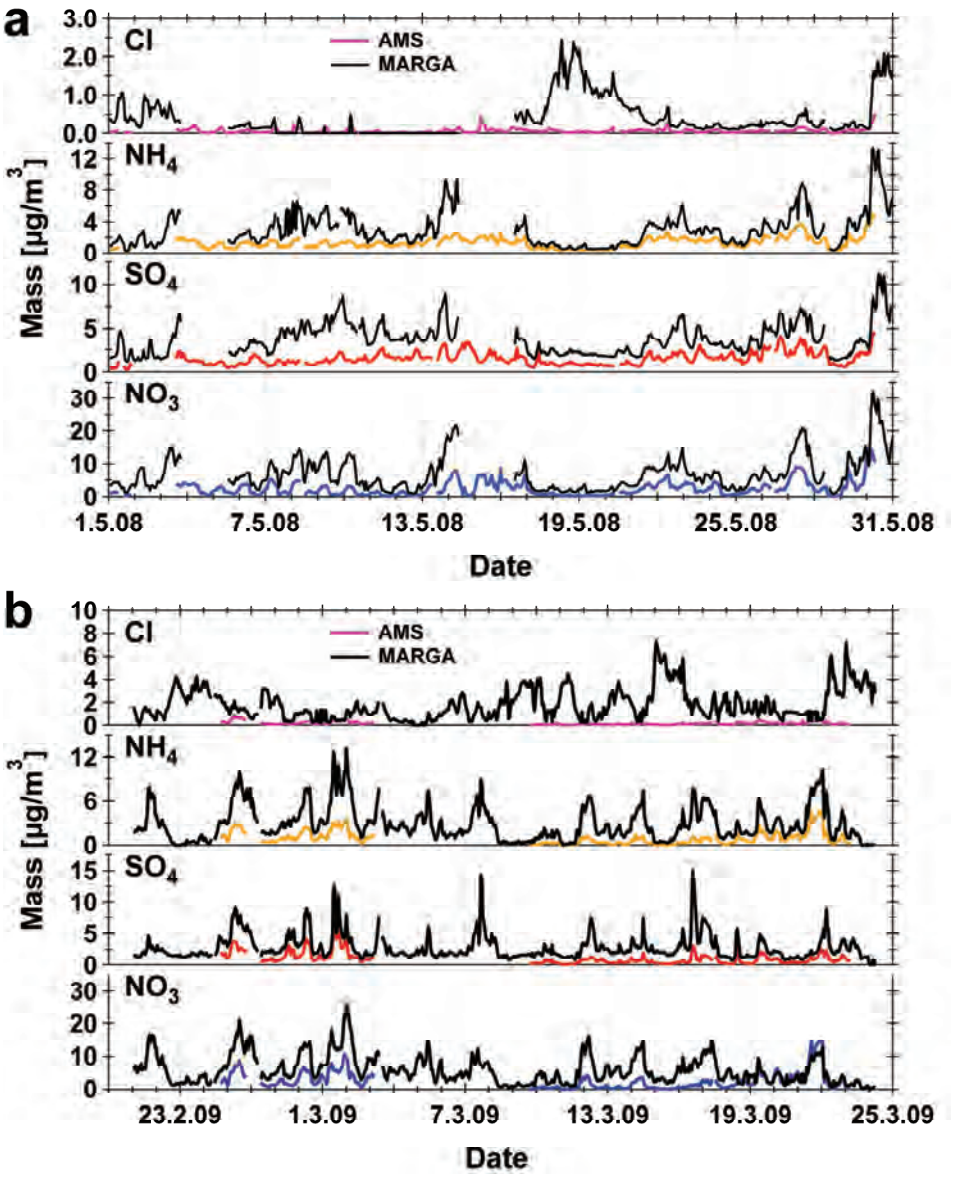


Figure 5.9 Time series of AMS (colored lines) and MARGA (black lines) chloride, ammonium, sulfate and nitrate mass in 2008 (a) and 2009 (b).

During the campaigns in 2008 and 2009 an instrument for Measuring AeRosols and GAses (MARGA) was deployed at the ground floor of CESAR tower. Here the first long term parallel measurement of the AMS and MARGA is presented. The MARGA instrument was attached to a separate inlet at 4 m height and sampled at ambient *RH* and

temperature. The MARGA is a combination of a Wet Annular Denuder (WAD) followed by a Steam Jet Aerosol Collector (SJAC, [*Slanina et al.*, 2001]) to facilitate the chemical online analysis of water soluble gases and particulate aerosol components at the same time [*Trebs et al.*, 2004]. The instrument can be run with different inlets to confine the particle size range. Data presented in Figure 5.9 were measured with a $PM_{10}$ sampling inlet. Figure 5.9 a and b are separated into four panels presenting from top to bottom the particulate chloride, ammonium, sulfate and nitrate concentrations measured by AMS (colored lines) and MARGA (black lines). Beside the different measurement ranges, the different measurement objectives of these two instruments must be kept in mind when comparing the data. While the AMS measures the non-refractory, the MARGA measures the water soluble components of aerosol particles. Still, a very good qualitative agreement especially for nitrate, sulfate and ammonium is achieved in 2008 and 2009 (see also Appendix A.3.2 and A.3.3). The different measurement techniques are partly reflected in the results of the chloride measurements. Major deviations are visible for the scavenged background situation middle of May 2008, when the source of chloride measured by MARGA is mainly sodium chloride, transported by air masses from the North Sea to the measurement site (top panel Figure 5.9 a). Sodium chloride is a substance that cannot be detected by the AMS at standard vaporizer temperatures of 580 °C to 600 °C. Still, both instruments seem to have measured the same chloride source from $6^{th}$ to $11^{th}$ of May 2008, when distinct spikes are visible in both time series. The 2009 measurement period was dominated by westerly winds (top panel in Figure 5.3), hence, air masses measured in Cabauw originated from the North Sea and the British Channel. Very different chloride time series for AMS and MARGA are presented in the top panel of Figure 5.9 b, since the major chloride source in $PM_{10}$ is supposedly sea salt.

### 5.3.3. MARGA-Sizer

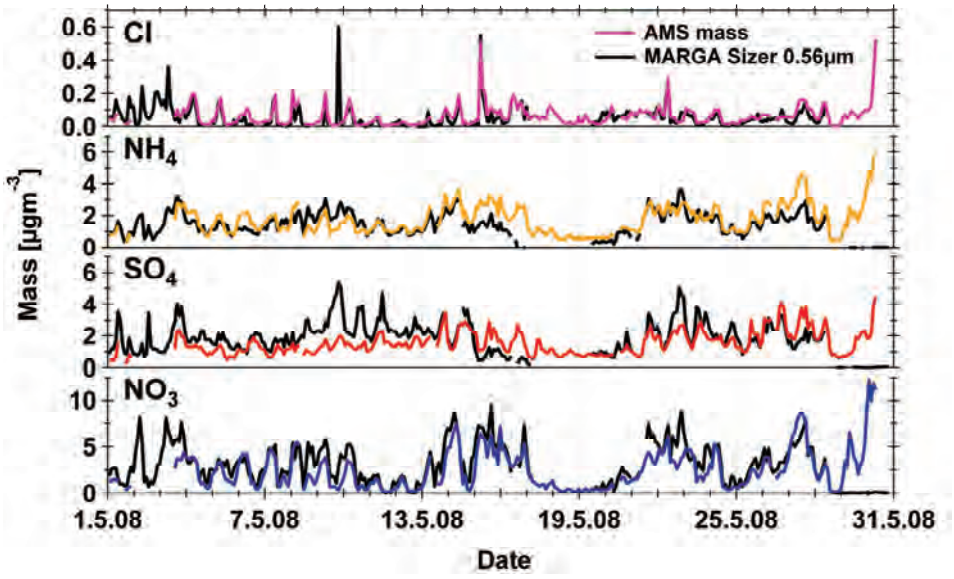


Figure 5.10 Time series of AMS and MARGA Sizer (0.56 µm channel) chloride, ammonium, sulfate and nitrate mass.

An enhanced version of the MARGA is the MARGA Sizer [*ten Brink et al.*, 2007], which was deployed at CESAR tower during May 2008. The instrument was located beside the MARGA and used the same tower inlet at 4 m height, sampling the aerosol at atmospheric temperature and *RH*. Key difference between the MARGA and MARGA Sizer is a pre-separator of parallel mounted impactors for size classification defining the measurement range of the particles by different cut off sizes. During May 2008 the MARGA Sizer was operated with impactors of the following cut off sizes: 0.18 µm, 0.32 µm, 0.56 µm, 1.00 µm, and 2.00 µm. Measurements through the different size classes were alternated, resulting in a semi-continuous measurement but gaining insights to the size distribution of the individual species. Additionally to the five impactor inlets, an inlet equipped with a particle filter was used to perform blank measurements and determine the background concentration of the compounds. The set up of the MARGA Sizer after the size-classification was identical to the MARGA set up, i.e. the aerosol stream passed through a wet annular denuder to remove the water soluble gas phase species and was then led through a SJAC for subsequent chemical analysis of the aerosol particles. Figure 5.10 shows the time series of particulate chloride, ammonium, sulfate and nitrate (from top to bottom) measured by the AMS (colored lines) and the MARGA Sizer (black lines)

presenting the results of the 0.56 µm channel. Additionally to the good qualitative agreement like in the comparison to the MARGA results (chapter 5.3.2) very good quantitative agreement is achieved for data size selected by the 0.56 µm impactor. Since the AMS is a $PM_1$ instrument best quantitative agreement was expected to the data obtained through the 1.00 µm channel. In fact, the measurement results of the 1.00 µm channel are on average a factor of two higher than the AMS results. Up to now, this discrepancy could not be resolved and further parallel measurements of the two instruments are needed in the future to clarify the causes of this observation.

Correlations to the 0.56 µm channel of the individual species (Figure 5.11 colored by time) show ratios ranging from 1.18 and 1.16 for nitrate and sulfate, respectively to 0.84 and 0.79 for chloride and ammonium, respectively. Correlations to the other sampling channels are presented in Appendix A.3.4.

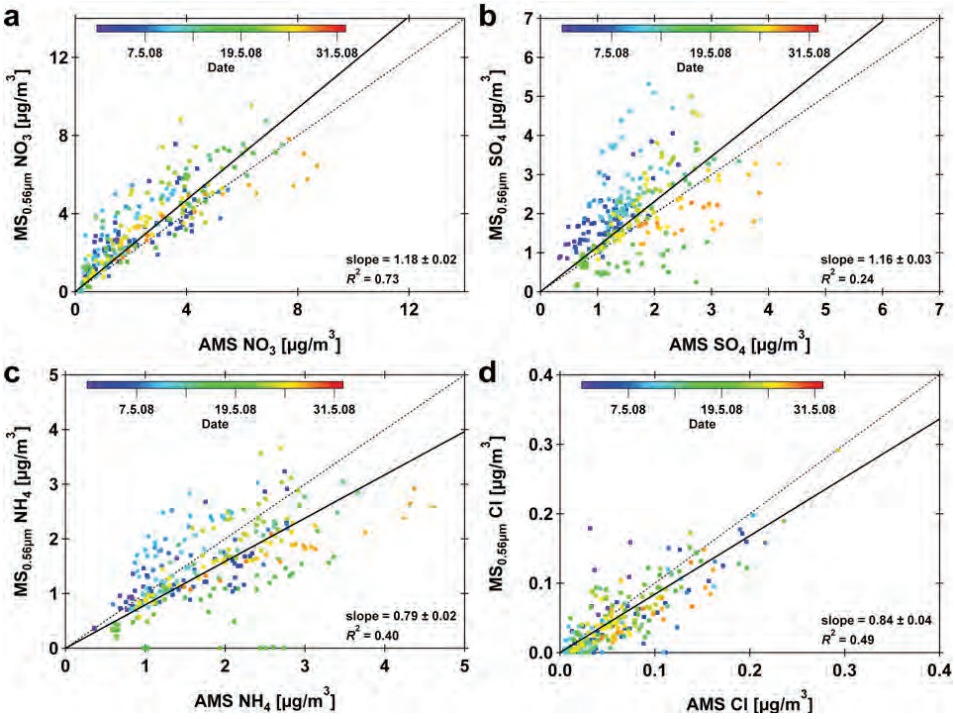


Figure 5.11 Correlation of MARGA Sizer (0.56 µm channel) and AMS for (a) nitrate, (b) sulfate, (c) ammonium and (d) chloride.

## 5.4. PMF Analysis of the Organic Particulate Aerosol

Positive Matrix Factorization (PMF, [*Paatero and Tapper*, 1994; *Paatero*, 1997]) is a variant of factor analysis that is a common analysis tool in atmospheric research for investigating big datasets of long term measurements (of several months) originating from different instruments [*Reff et al.*, 2007]. PMF is based on mass conservation and requires no a priori information. The constraint to positive solutions allows a good application to real datasets. Due to the combination of a large *m*/*z* space (in general 300 and more) and high time resolution, AMS measurements generate huge datasets even in UMR. Other statistical approaches such as multivariate linear regression models have been applied to deconvolve AMS mass spectra [*Zhang et al.*, 2005] but PMF is becoming a more and more prominent analysis technique in the AMS community [*Aiken et al.*, 2009; *Huffman et al.*, 2009; *Lanz et al.*, 2007; *Ulbrich et al.*, 2009].

The matrix ($\mathbf{X}_{ij}$) of a dataset can be expressed as the product of a matrix ($\mathbf{G}_{ip}$) and a matrix ($\mathbf{F}_{pj}$) plus a residuum matrix ($\mathbf{E}_{ij}$) containing the residuals not included in $\mathbf{G}\cdot\mathbf{F}$:

$$\mathbf{X}_{\mathrm{ij}} = \mathbf{G}_{ip} \cdot \mathbf{F}_{pj} + \mathbf{E}_{ij} \qquad \textbf{(5.1)}$$

In the case of AMS data generally the organic fraction of the mass spectra is analyzed by PMF. The rows of the matrix ($\mathbf{X}_{ij}$) represent the averaged mass spectra obtained at each single measurement point and the columns represent the time series of the individual *m*/*z* measured. The rows of the $\mathbf{F}_{pj}$ matrix are the factor profiles and the columns of matrix $\mathbf{G}_{ip}$ are the time series of the factors representing the contribution of each factor to the solution at that point in time. A scheme of the PMF concept is shown in Figure 5.12 to illustrate the application to AMS datasets.

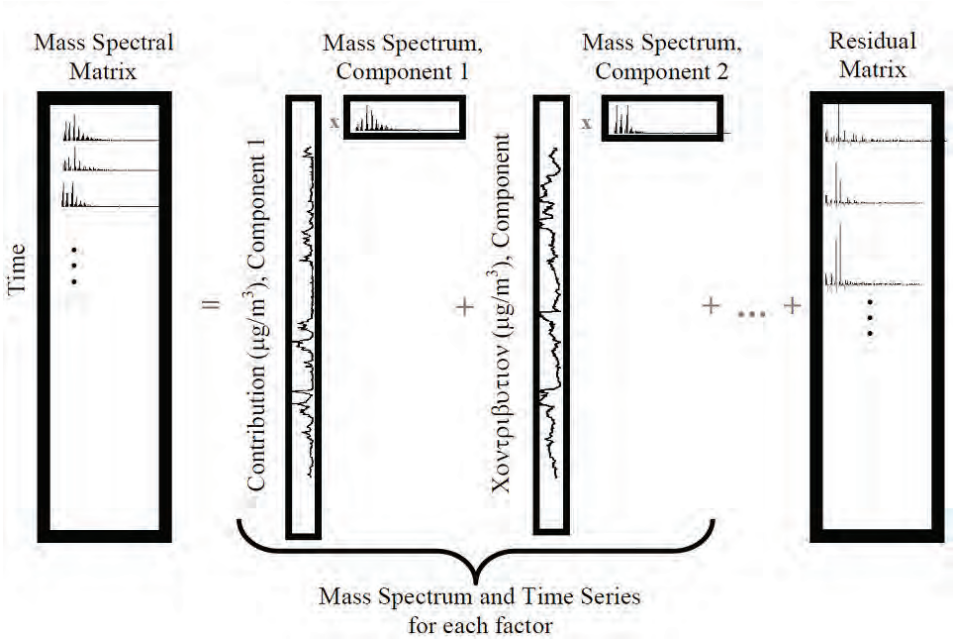


Figure 5.12 Schematic of PMF factorization of an AMS dataset. The time series of the factors make up the matrix G and the mass spectra of the factors make up the matrix F (taken from [*Ulbrich et al.*, 2009]).

The application of PMF analysis to the organic fraction of AMS mass spectra can be used for source apportionment of organic aerosol which is an important part of field data interpretation. The determination of factors i.e. sources must be based on on mathematical considerations such as a minimum residual but also on characteristics of the factors in our case mass spectra. If too few factors are chosen, the characteristics of several sources might be merged in one factor/MS. Too many factors can cause the splitting of a real factor into artificial factors, which cannot be assigned to a specific source. Each factor needs to be validated based on the knowledge of the mass spectrum characteristics and/or by correlation of the time dependence to so called tracers. Tracers are time series of compounds measured by the AMS itself e.g. the time series of $NO_3$, $SO_4$, $NH_4$, and Cl or data of gas phase species like $O_3$, $SO_2$, CO, and $NO_x$, or particulate species like black carbon (BC) or elemental carbon (EC) acquired by collocated instruments. The major sources of ambient organic aerosol (OA) are strongly dependent on the measurement environment, but generally oxidized organic aerosol (OOA) and hydrocarbon-like organic aerosol (HOA) are detected. These two classes themselves can be divided into sub classes. OOA for example can be divided into general sub classes such as highly oxidized OA (OOA-1 or low-volatile (LV-OA) and less oxidized OA (OOA-2 or semi-volatile (SV-OA)

[*Jimenez et al.*, 2009] or into specific sub classes like biomass burning [*Aiken et al.*, 2009], charbroiling [*Lanz et al.*, 2007] or levoglucosan [*Schneider et al.*, 2006]. Sub classes of HOA are for example diesel exhaust or lubricating oil [*Canagaratna et al.*, 2004]. A whole range of mass spectra obtained during laboratory, chamber, or field measurements is presented on the AMS mass spectral database [*Ulbrich et al.*] and can be used as reference spectra when presenting PMF results.

The results of PMF analysis and the validation of each determined factor for the two measurement periods at CESAR tower in May 2008 and March 2009 will be presented in the upcoming sections. While a 4-factor solution was chosen for the 2008 dataset characterized by high photo-oxidation activity, only 3 factors were determined for the dataset of 2009. In a first step, the mass spectra determined for the individual factors will be investigated and compared to published mass spectra from other research groups, which are available on the MS database [*Ulbrich et al.*]. The mass spectra are presented in Figure 5.13 and Figure 5.14.

Figure 5.13 shows the normalized mass spectra of the four factors F1 to F4 determined for the measurement period May 2008. The MS of the first factor (bottom of Figure 5.13) is dominated by the signals on *m*/*z* 44 and *m*/*z* 18. Significant signal intensity is assigned to *m*/*z* 43 and *m*/*z* 29, and distinctive signals are determined on *m*/*z* 41 and *m*/*z* 55. Mass spectra of this type are associated with LV-OOA and the mass spectra is very similar ($R^2$ = 0.98) to the OOA1 spectrum measured at an urban background site in Zurich, CH by [*Lanz et al.*, 2007]. The most dominant signal in the MS of factor 2 is on *m*/*z* 43 followed by the signals on *m*/*z* 29, *m*/*z* 18, *m*/*z* 44 and, *m*/*z* 27, as well as distinctive signal intensity on *m*/*z* 55 and *m*/*z* 91. SV-OOA are characterized by this mass spectrometric pattern. The MS of the third factor is dominated by peaks on *m*/*z* 27 and *m*/*z* 29, *m*/*z* 41 and *m*/*z* 43, and *m*/*z* 55 and *m*/*z* 57. These double peaks separated by 14 amus are characteristic for HOA and the MS shows some similarity to a diesel MS ($R^2$ = 0.79) measured by [*Mohr et al.*, 2009] and to a HOA MS ($R^2$ = 0.84) measured in Pittsburgh, USA in September 2002 by [*Zhang et al.*, 2005]. The fourth MS representing F4 is similar to F1 dominated by the peaks on *m*/*z* 18 and *m*/*z* 44 but the only other significant peaks are on *m*/*z* 17, *m*/*z* 29, and *m*/*z* 40 and no signal is assigned to peaks above *m*/*z* 44. This spectrum represents a highly oxygenated OA and is very similar to the MS of fulvic acid ($R^2$ = 0.97) acquired in a laboratory experiment by [*Alfarra*, 2004]. Correlations of the factor MS to the database mass spectra are presented in Appendix A.4.

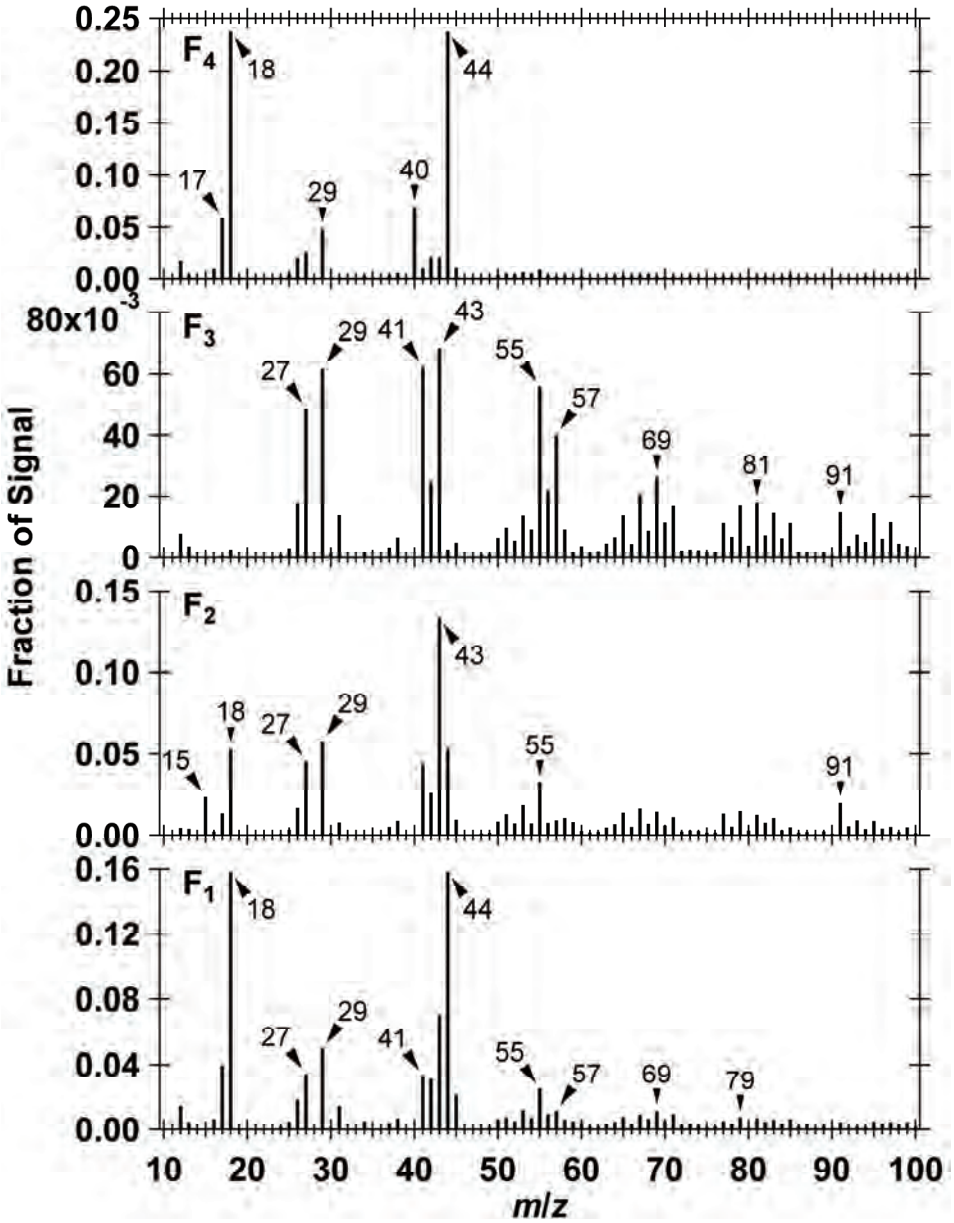


Figure 5.13 Normalized mass spectra of the four factors F1 to F4 (from bottom to top) determined by PMF analysis of the organic fraction of the 2008 measurements at CESAR tower.

The three PMF mass spectra determined for the March 2009 measurement period at CESAR tower are presented in Figure 5.14. Factor 1 exhibits a MS which resembles fulvic acid ($R^2 = 0.90$) and is highly similar ($R^2 = 0.98$) to the OOA MS determined for wintertime measurements in Zurich, CH by [*Lanz et al.*, 2008]. Alike the MS of factor 3 in

2008, the MS of factor 2 in 2009 corresponds to HOA, dominated by the double peak pattern on *m*/*z* 27 and *m*/*z* 29, *m*/*z* 41 and *m*/*z* 43, and *m*/*z* 55 and *m*/*z* 57. Quite some similarity is given to the mass spectra representing HOA in the publication of [*Lanz et al.*, 2008] ($R^2$ = 0.88) and [*Zhang et al.*, 2005] ($R^2$ = 0.94), respectively. The MS of factor 3 reflects a so far non specific OOA with major signal intensities on *m*/*z* 18 and *m*/*z* 44 and significant contributions on *m*/*z* 29, *m*/*z* 43, *m*/*z* 27, *m*/*z* 41, and *m*/*z* 55. Distinctive peaks are further assigned to *m*/*z* 55, *m*/*z* 69, and *m*/*z* 91. This MS shows no distinct similarity to any MS available on the MS database, but further analysis of the time series will give insights to the origin of this factor. Correlations of the factor MS to the database mass spectra are presented in Appendix A.4.

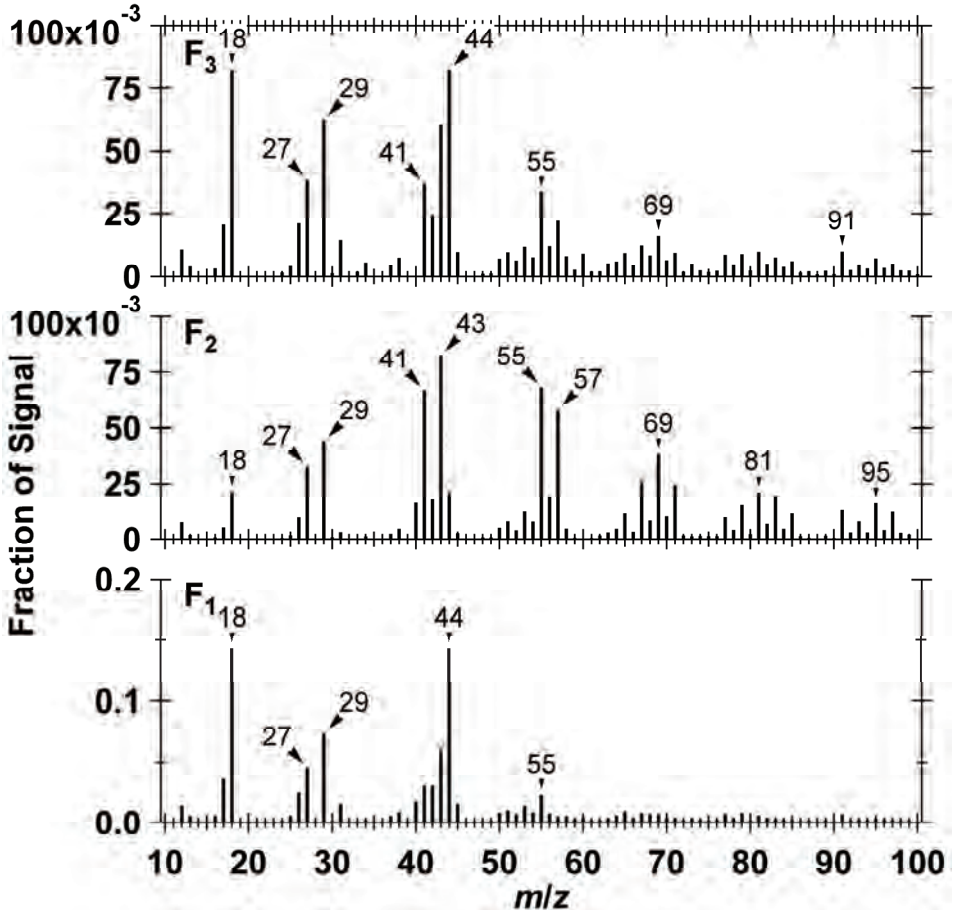


Figure 5.14 Normalized mass spectra of the three factors F1 to F3 (from bottom to top) determined by PMF analysis of the organic fraction of the 2009 measurements at CESAR tower

As already mention in the beginning of this section, the time series of the factors need to be investigated towards correspondence to specific tracers. While LV-OOA is generally associated with the particulate sulfate fraction, SV-OOA is associated with the particulate nitrate fraction both measured by the AMS [*Lanz et al.*, 2007]. The HOA time series shows generally a similar trend as gas phase CO, $NO_x$ or particulate black carbon (BC) representing combustion sources of primary OA (POA). The time series of the PMF factors and specific tracers are presented in Figure 5.15 for 2008 and in Figure 5.16 for 2009. In Figure 5.15 the time series of the four factors F1 to F4 (from bottom to top) are given together with corresponding tracers. The time series of Factor 1 (black line, bottom of Figure 5.15) corresponds well with the time series of particulate sulfate measured by the AMS (red line and axis) as expected for LV-OOA. The time series of the second organic factor determined by PMF analysis corresponds well with a specific particulate nitrate fraction (turquoise line and axis), which is associated with organic nitrate. A detailed explanation on the determination of organic nitrate from field data will be given in chapter 5.5. The time series of the third factor of the 2008 measurements is very similar to the time trace of BC (brown line and axis), which is expected for HOA. BC data was obtained from Multi Angle Absorption Photometer (MAAP 5012, [*Petzold and Schönlinner*, 2004]) operated by TNO. Attention must be paid to the potential misinterpretation of brown carbon as black carbon [*Andreae and Gelencsér*, 2006]. Brown carbon is light absorbing organic particulate matter like humic acid which is often found in biomass burning plumes [*Gustafsson et al.*, 2009]. The MS of F3 was correlated to the MS of humic acid obtained from laboratory measurements [*Alfarra*, 2004] and available on the MS database. An extreme low coefficient of determination ($R^2 = 0.089$) was found. This was expected, since significant biomass burning activity is very unlikely for the Cabauw area in particular and Western Europe in general. Neither other species measured by the AMS nor compounds determined by auxiliary measurements of collocated instruments provide corresponding tracers to the time series of the fourth factor, which MS resembles a highly oxygenated OA such as fulvic acid.

The time series of the three factors determined for the March 2009 measurement period are presented in Figure 5.16. Factor 1 which was characterized based on the MS as highly oxygenated OA reveals a temporal evolution, which is similar to the time series of particulate nitrate (dark blue line and axis) measured by the AMS itself. Though factor 2 is clearly representing HOA none of the typical tracers such as $NO_x$, CO or BC have a similar time trace. The time series of the third factor matches very well to the time series of the

specific nitrate fraction, which is associated with organic nitrate. Details on organic nitrates will be given in the following chapter.

Each factor determined by PMF for 2008 and 2009 could be validated by the characteristics of the mass spectra and/or the similar temporal behavior towards corresponding tracers.

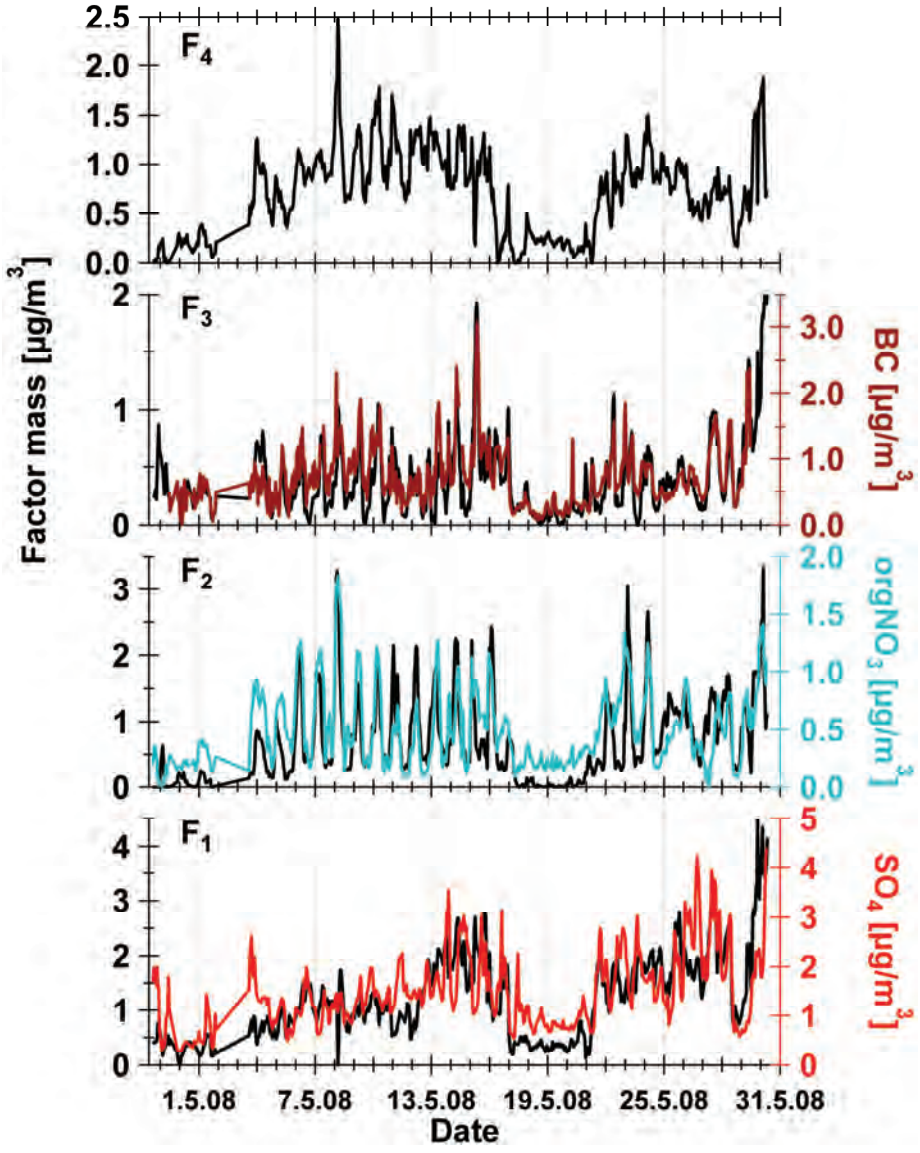


Figure 5.15 Time series of the PMF factors F1 to F4 (from bottom to top) determined for the organic mass fraction of the 2008 measurement period at CESAR tower. Factors (black lines, left axis) and the according tracers (colored lines, right axes matching the respective trace in terms of color) are given.

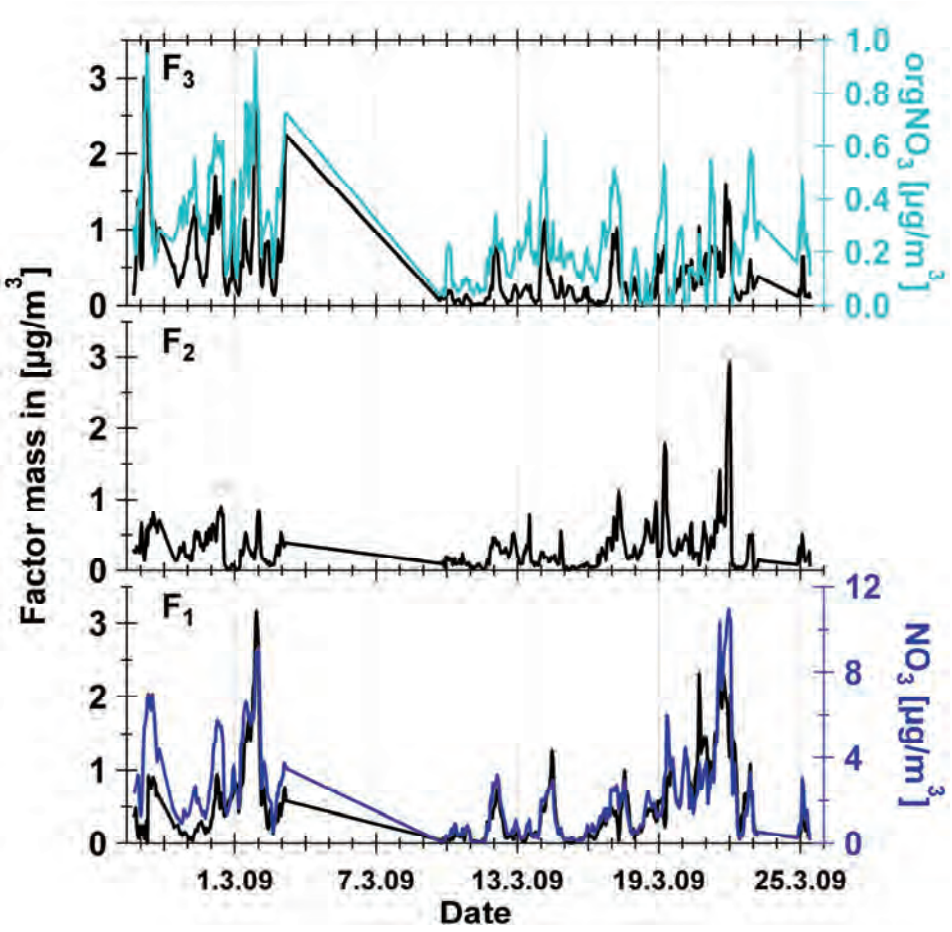


Figure 5.16 Time series of the PMF factors F1 to F3 (from bottom to top) determined for the organic mass fraction of the 2009 measurement period at CESAR tower. Factors (black lines, left axis) and the according tracers (colored lines, right axes matching the respective trace in terms of color) are given.

## 5.5. Organic Nitrates in Ambient Measurements

A tool for the determination of organic nitrates ($orgNO_3$) is the investigation of the nitrate fragmentation pattern as presented in chapter 4. The ratio of the major fragments $NO_2^+$ and $NO^+$ was found to be 0.1 for organic nitrates, which is significantly lower than the ratio of 0.4 of the generally most abundant nitrate originating from ammonium nitrate. But the existence of organic nitrate can not be determined on the fragmentation ratio alone, since other nitrate containing compounds have similar or even lower fragmentation ratios.

The fragmentation ratios of magnesium, sodium, and calcium nitrate in comparison to organic nitrate and ammonium nitrated are presented in Table 5.4.

Table 5.4 Table of nitrate fragmentation ratios partly taken from [*Alfarra*, 2004]*.

| Substance | $NO_2^+/NO^+$ ratio |
|---|---|
| $NH_4NO_3$ | 0.4 |
| $orgNO_3$ | 0.1 |
| $Mg(NO_3)_2$ | 0.09* |
| $NaNO_3$ | 0.03* |
| $Ca(NO_3)_2$ | 0.02* |

For the data collected at Cabauw, the nitrate fragmentation ratio was derived from high resolution analysis. The resolving power of the ToF AMS allows the clear separation of the ion peaks of interest from neighboring signals (Figure 4.5). Average nitrate fragmentation ratios of 0.31 and 0.33 were determined for May 2008 and March 2009, respectively. The ratio is clearly correlated to the fractional nitrate abundance ($NO_3$/Total) and exhibits a diurnal pattern in 2008. The fractional abundance of nitrate in turn is mainly driven by the abundance of ammonium nitrate, which is temperature dependent due to its high vapor pressure. The temperature variations between night and day in 2008 and the overall lower ambient temperatures in the winter/spring measurement period in 2009 are reflected in the $NO_3$/Total ratio. An interesting behavior of the nitrate fraction can be observed during the scavenged background situation from 17$^{th}$ of May to 21$^{st}$ of May 2008 with a nitrate fragmentation ratio of only 0.1. $NH_4NO_3$ is highly water soluble and can be easily washed out from the gas phase. Since the aerosol is the coexistence of gas and particulate phase by definition, the particulate concentration of volatile and semi volatile components is strongly driven by their gas phase concentration. A gas phase depletion of $NH_4NO_3$ causes a concentration gradient between gas and particulate phase. This gradient in turn leads to evaporation of $NH_4NO_3$ from the particulate aerosol phase and consequently to degradation within the particles causing the less volatile nitrate fraction in the form of organic nitrate to dominate in the particulate phase.

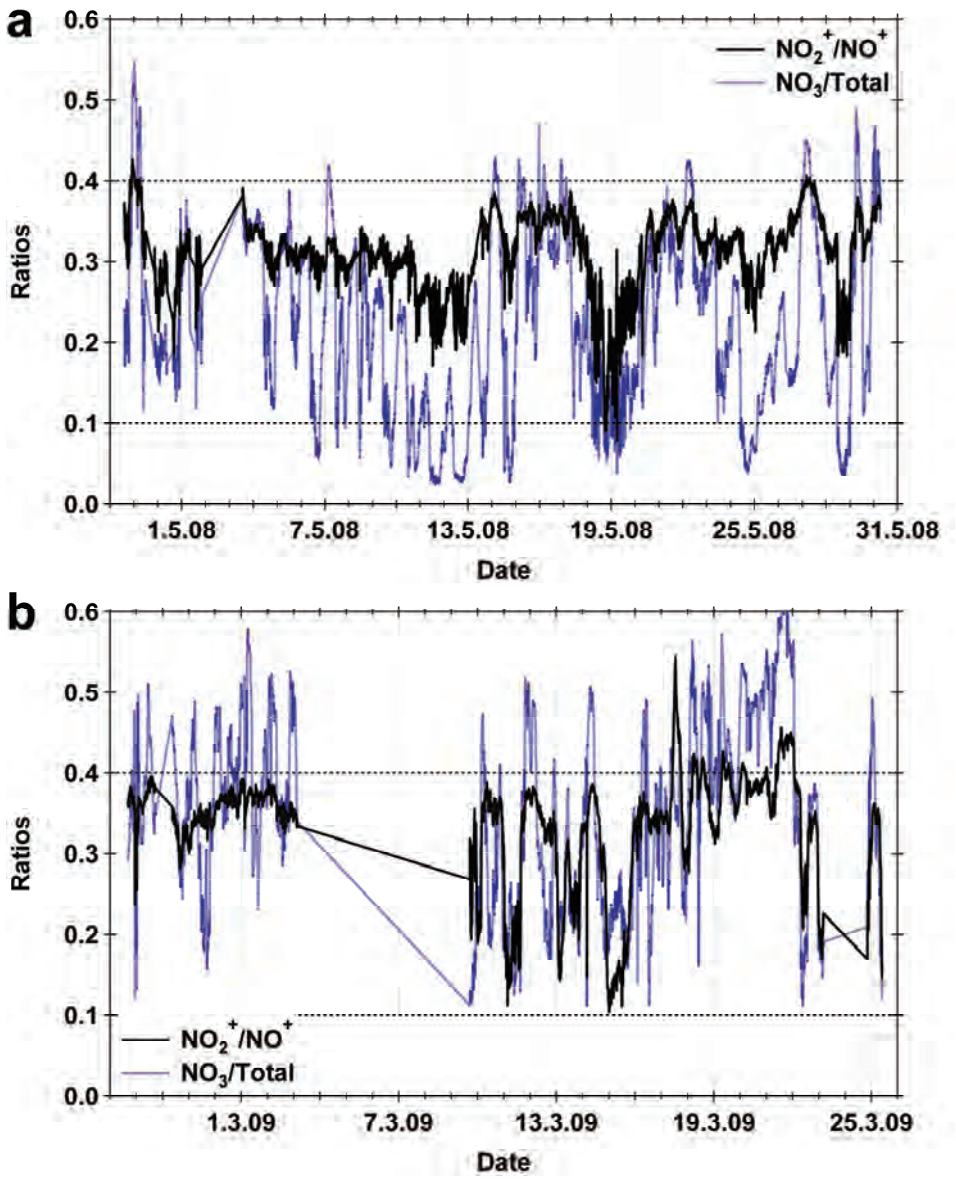


Figure 5.17 $NO_2^+/NO^+$ fragmentation ratio determined by high resolution analysis (black solid line) and fractional abundance of nitrate ($NO_3$/Total, blue line) for the measurement periods in 2008 (a) and 2009 (b) at CESAR tower. Indicated by dotted black lines are the fragmentation ratios of organic nitrate (0.1) and ammonium nitrate (0.4).

As already mentioned in the beginning of this section, other compounds have low $NO_2^+/NO^+$ fragmentation ratios, too, so they might interfere the classification of nitrate as organic nitrate. In 2008 the collocated MARGA Sizer was capable of measuring sodium in particle size fractions comparable to the measurement range of the AMS. Presented in

Table 5.5 are the molar concentrations of sodium, nitrate, ammonium and sulfate measured by the MARGA Sizer over the entire May 2008. Since special interest exists regarding the scavenged background period the concentrations for this time period are given in brackets.

Table 5.5 Molar concentrations of different species determined for the 0.56 µm, 1 µm, and 2 µm channel of the MARGA Sizer in May 2008. Concentrations representing only the scavenged background period are given in brackets.

| Species | Concentration [mol/m$^3$] | | |
|---|---|---|---|
| | 0.56 µm channel | 1 µm cannel | 2 µm cannel |
| Na | $2.3 \cdot 10^{-9}$ ($2.4 \cdot 10^{-9}$) | $2.3 \cdot 10^{-9}$ ($2.6 \cdot 10^{-9}$) | $2.8 \cdot 10^{-9}$ ($3.5 \cdot 10^{-9}$) |
| $NO_3$ | $2.9 \cdot 10^{-8}$ ($1.4 \cdot 10^{-8}$) | $4.8 \cdot 10^{-8}$ ($2.0 \cdot 10^{-8}$) | $5.1 \cdot 10^{-8}$ ($2.4 \cdot 10^{-8}$) |
| $NH_4$ | $4.9 \cdot 10^{-8}$ ($2.4 \cdot 10^{-8}$) | $7.8 \cdot 10^{-8}$ ($3.5 \cdot 10^{-8}$) | $9.5 \cdot 10^{-8}$ ($4.2 \cdot 10^{-8}$) |
| $SO_4$ | $1.3 \cdot 10^{-8}$ ($8.0 \cdot 10^{-9}$) | $1.8 \cdot 10^{-8}$ ($9.8 \cdot 10^{-9}$) | $2.1 \cdot 10^{-8}$ ($1.2 \cdot 10^{-8}$) |

The AMS is a so called $PM_1$ instrument, so the results of the 1 µm channel should be representative. Beside the fact, that there is not enough sodium to account for the nitrate concentration, there is no correlation between sodium and nitrate in this time range (slope = -0.003 ± 0.002).

A nitrate fragmentation ratio of 0.4 which indicates the abundance of pure $NH_4NO_3$ is reached on the 27.05.2007 between 02:00 h and 11:30 h. This period coincides with the arrival of Sahara dust from Northern Africa. The aerosol particles composition is dominated by nitrate (45%) followed by organics (22%), ammonium (21%) and sulfate (12%). This indicates that the nitrate transported to the Cabauw measurement site is dominated by inorganic $NH_4NO_3$. The Sahara dust transport is interrupted for one day at the 28.05.2008 due to meteorological conditions. This fact is clearly reflected by the sharp drop of the nitrate fragmentation ratio from 28.05.2008 10:00 h to 29.05.2008 01:00 h.

The behavior of the $NO_2^+/NO^+$ fragmentation pattern in 2009 can not be as easily interpreted as in 2008 as the AMS results generally lack the structured behavior of 2008. A $NO_2^+/NO^+$ ratio as low as 0.1 is determined for the nights of the 11$^{th}$ and 15$^{th}$ of March 2009. However, ratios above 0.4, which is up to now the highest fragmentation ratio known for nitrate, were measured repeatedly between 17$^{th}$ and 22$^{nd}$ of March. This fact cannot be explained by any auxiliary measurements and needs to be investigated by measurement of further nitrate containing compounds in the future.

Nevertheless, PMF analysis of the organic fractions yielded a factor which time series was very similar to the temporal abundance of organic nitrate for each measurement period (Figure 5.15 and Figure 5.16). The concentration of organic nitrate was calculated on the assumption that the entire nitrate consists solely of ammonium and organic nitrate. The contribution of the two nitrate specie was determined from the $NO_2^+/NO^+$ ratio at each measuring time according to equation (5.2). Fragmentation ratios as given in Table 5.4. were used for the calculation.

$$\left(NO_2^+/NO^+\right)_{measured} = a \cdot \left(NO_2^+/NO^+\right)_{NH_4NO_3} + b \cdot \left(NO_2^+/NO^+\right)_{OrgNO_3} \quad \textbf{(5.2)}$$

The fraction of organic nitrate within the particulate nitrate mass (factor *b* in equation (5.2)) over time for the measurements at CESAR tower are shown in Figure 5.18 a (2008) and b (2009). The average organic nitrate mass concentration of 0.5 µg/m$^3$ in 2008 corresponds to 34.9 % of the average nitrate and 5.2% of the average total mass in this measurement period. In 2009 an average organic nitrate concentration of 0.2 µg/m$^3$ was detected, which correspond to 9.7 % of the nitrate and 3.6 % of the total mass.

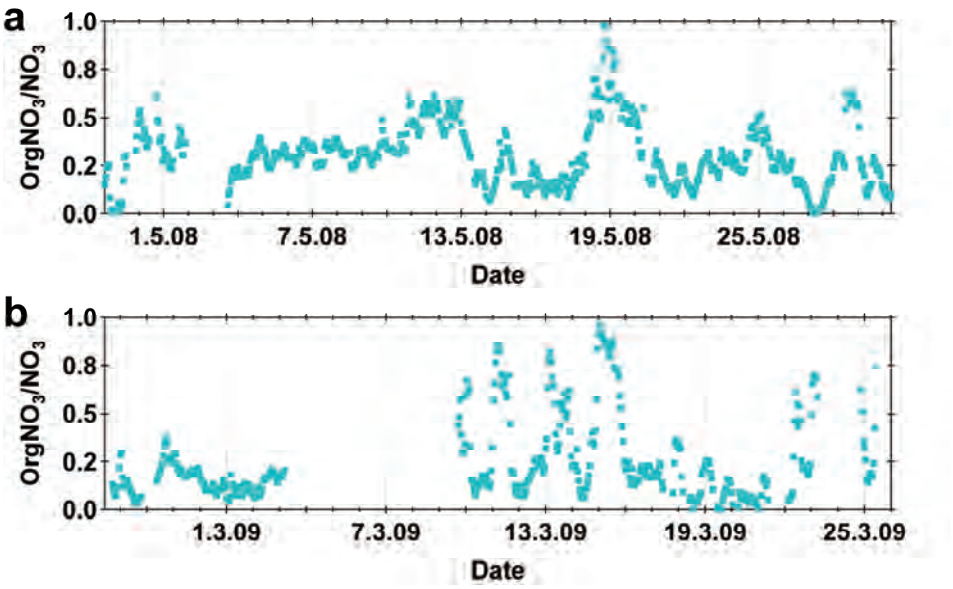


Figure 5.18 Fraction of organic nitrate in the particulate nitrate mass ($OrgNO_3/NO_3$) determined at CESAR tower in May 2008 (a) and March 2009 (b).

The contribution spans over the entire range from 0 to 1 in both years with an average contribution of 30 % in 2008 and 22 % in 2009. Maximal contributions are reached on 18.05.2008 and 15.03.2009 when almost the entire nitrate mass consists of organic nitrate.

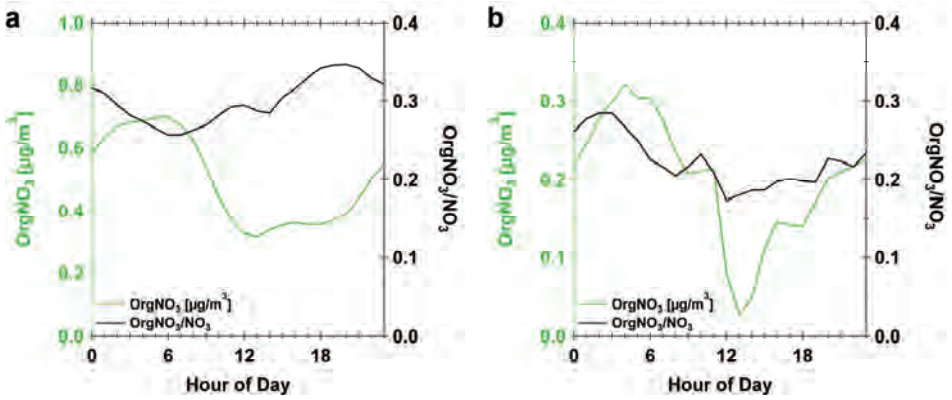


Figure 5.19 Diurnal averages of organic nitrate concentration (green, left axis) and fraction of organic nitrate in the nitrate mass (black, right axis) in May 2008 (a) and February 2009 (b).

In 2008 the average diurnal profile of the organic nitrate mass shows a maximum during night/early morning (green line on left axis) but the maximum contribution of organic nitrate to the nitrate mass is reached during evening hours (black line, right axis) as can be seen in Figure 5.19 a. The average diurnal profile of organic nitrate in 2009 not dominated by a diurnal pattern but rather by single events between 10.03.2009 and 16.03.2009. In contrast to 2008, not only the organic nitrate mass but also the fraction of organic nitrate within the total nitrate mass shows a minimum during midday.

## 5.6. Summary and Conclusions

Extensive AMS measurements over the course of several weeks were performed at CESAR tower, NL in May 2008 and February 2009. While the measurement period in 2008 was dominated by organics (40 %), nitrate was the dominant species detected in 2009 (42 %). In both years, nitrate was the most abundant inorganic specie detected in AMS and MARGA $PM_{10}$ measurements. The phenomenon of high nitrate fractional abundances is not only typical for the measurement location [*ten Brink et al.*, 2009] but is known to occur all over Europe [*Putaud et al.*, 2004; *ten Brink et al.*, 1997]. The average aerosol particulate mass loading was 9.72 µg/m$^3$ in 2008 and 5.62 µg/m$^3$ in 2009, which is in good

agreement with $PM_{2.5}$ concentrations determined at different rural European locations [*Van Dingenen et al.*, 2004]. The first application of the new $RIE_{H2O}$ for the determination residual particulate water in ambient aerosol particles is presented. Concentrations of 0.64 µg/m$^3$ and 0.31 µg/m$^3$ in 2008 and 2009, respectively, were found. Size resolved mass distribution measurements of the individual species detected in the AMS indicate a mode diameter at 400 nm to 500 nm for the total mass as well as for the inorganic species. The mass distribution of organics is much broader and extents into size ranges below 100 nm, Similar size distributions with inorganic species dominating in the larger size fraction and a bimodal behavior of organics is often the case in AMS measurements independent of location [*Alfarra et al.*, 2004; *Allan et al.*, 2003]. Comparison of AMS total mass to mass derived from SMPS measurements show high qualitative and quantitative agreement. The data of a collocated MARGA ($PM_{10}$) shows very good agreement within the comparability of the two measurement techniques. In 2008 an additional MARGA Sizer was operated at CESAR tower. Mass concentrations a factor of 2 higher than the AMS total mass loading were found for data measured through the $PM_1$ channel. Best quantitative agreement was obtained to the data sampled through the $PM_{0.56}$ channel but the correlation factors were better for the $PM_1$ channel. Since this data present the first comparison of AMS and MARGA Sizer of ambient aerosol particles, further parallel sampling campaigns are needed to investigate the presented discrepancy. PMF analysis was performed on the organic mass fractions determined in 2008 and 2009. While the 2008 organics could be characterized by 4 factors (LV-OOA, SV-OOA, HOA, and a fulvic acid like OOA) only three factors were needed to characterize the 2009 organics (LV-OOA, HOA, and an undefined OOA). The findings on the specific fragmentation ratio of organic nitrate gained by analysis of BVOC oxidation with $NO_3$ in an atmospheric simulation chamber (chapter 4) were applied to the two field datasets. A significant amount of organic nitrate was detected, with average contributions to the particulate nitrate of 30 % in 2008 and 22 % in 2009. Additionally, a PMF factor highly correlated to the time series of organic nitrate was determined for each measurement period.

# 6. Summary

Atmospheric aerosol particles currently comprise the major uncertainty in the assessment of future global climate. The scientific understanding of their physical, chemical and climate impact properties is still not sufficient. Atmospheric particles are composed of a huge variety of compounds, of which nitrate, sulfate, and ammonium are generally the major inorganic contributors to the fine fraction. The fractional abundance of organics compounds can account for 20 % to more than 80 % of the ambient particle mass, but the determination of individual organic species is still challenging even with the latest experimental techniques. The Aerodyne Aerosol Mass Spectrometer (AMS) is a commercially available online $PM_1$ instrument that facilitates the mass spectrometric and size resolved investigation of aerosol particles in the first instance but insights to the particles morphology and volatility can be gained additionally. Two different versions of the AMS a Quadrupol (Q-AMS) and a High Resolution Time of Flight (HR-ToF-AMS) instrument were used for the characterization and investigation of atmospheric particles presented in this thesis.

Atmospheric aerosols were investigated on three different scales of complexity and size. Laboratory experiments were performed to determine the relative ionization efficiency of water ($RIE_{H2O}$) in an AMS (chapter 3), simulation chamber experiments gave insight to the reaction products of BVOC-$NO_3$ oxidation products (chapter 4), and two field campaigns were used to apply the findings from the previous experiments (chapter 5).

The $RIE_{H2O}$ was determined by measuring the crystal water content of different oxalate salts. Sodium, potassium, and ammonium oxalate were investigated and a $RIE_{H2O}$ of 2 was determined (chapter 3.3.2). When this finding was applied to oxalic acid a considerable ammonium contamination was revealed even if oxalic acid was directly taken from factory sealed containers (chapter 3.3.3). Special care should be paid to the experimental conditions when oxalic acid is used. Further investigations are needed to determine the nature and processes leading to this contamination.

Isoprene, limonene, and $\beta$-pinene were separately oxidized by $NO_3$ in the "Simulation of Atmospheric PHoto oxidation In a large Reaction" (SAPHIR) chamber at Forschungszentrum Jülich, Germany. The volatility of oxidation products was investigated by modulation of the AMS vaporizer temperature. While the detected mass loading of organics decreased with decreasing vaporizer temperature, the detected nitrate mass loading was not affected. It was therefore concluded that organic nitrates have a higher

vapor pressure in comparison to the other organic oxidation products formed in the reactions (chapter 4.3.1). Organic nitrates were estimated to account for up to 41 % of the particulate phase. High resolution analysis of the organic nitrates revealed a characteristic nitrate fragmentation pattern. The ratio of $NO_2^+$ ions to $NO^+$ ions was found to be 0.1 (chapter 4.3.2), which is significantly lower than the ratio found for nitrate originating from $NH_4NO_3$, the major source of particulate nitrate in the troposphere. This fragmentation ratio can be used to determine and quantify the amount of organic nitrate in ambient measurements and successful application is presented (chapter 5.5).

In May 2008 and February 2009 ambient aerosol measurements were performed at the Cabauw Experimental Site for Atmospheric Research (CESAR) Tower, The Netherlands. Each campaign lasted three to four weeks. A high resolution AMS was deployed to measure dried aerosol particles which were sampled from an inlet at 60 m height. An average particle concentration of 9.72 µg/m$^3$ dominated by organics (40 %) was detected in May 2008. Particles in 2009 were dominated by nitrate (42 %) and had an average mass concentration of 5.62 µg/m$^3$. Investigations of the amount of residual water with application of the new $RIE_{H2O}$ gave concentrations of 0.64 µg/m$^3$ and 0.31 µg/m$^3$ in 2008 and 2009, respectively. A mode diameter ranging between 400 nm and 500 nm was found for the total mass and the inorganic species by chemically resolved size distribution measurements. In contrast to the inorganic species, organics showed a much broader distribution. Beside slightly lower modal diameters (300 nm – 400 nm), the distribution curve showed pronounced tailing towards sizes below 100 nm (chapter 5.2) indicative of new particle formation. The AMS measurement results were compared to a range of collocated instruments. Size distribution data measured by a SMPS were available for the second half of May 2008. Mass concentrations were derived from this data and good agreement was found to the total AMS mass ($R^2$ = 0.87) (chapter 5.3.1). Comparison the mass loadings of the inorganic species to data from a Measuring AeRosol and GAses (MARGA, $PM_{10}$) instrument showed high qualitative agreement in both years (chapter 5.3.2). In 2008, an enhanced version of the MARGA called MARGA Sizer was additionally deployed at CESAR tower. Interestingly, best quantitative agreement was found to the data obtained through the $PM_{0.56}$, though best agreement was expected for the $PM_1$ sampling channel since the AMS is referred to as $PM_1$ instrument (chapter 5.3.3). This issue needs to be further investigated. The organic particulate fraction detected by the AMS was investigated by Positive Matrix Factorization. Four different organic fractions could be determined for the May 2008 campaign and three for February 2009. In both

years a low volatile (LV) a semi volatile (SV) oxygenated organic aerosol (OOA) fraction as well as a hydrocarbon-like (HOA) fraction were determined. The mass spectrum of the forth factor in May 2008 showed high correlation to fulvic acid ($R^2$ = 0.97) and represents a highly oxygenated organic aerosol (chapter 5.4). The amount of organic nitrate in the ambient aerosol particles was determined by usage of the specific fragmentation pattern of nitrate as found in the simulation chamber experiments. After ruling out possible interferences from other inorganic nitrate species such as sodium, calcium, or magnesium nitrate, the contribution of organic nitrate to the particulate nitrate mass was found to be on average 34.9 % and 5.2 % in 2008 and 2009, respectively (chapter 5.5).

The combination of laboratory, simulation chamber, and field measurements for the investigation of atmospheric particles was presented in this thesis. It was shown that specific features determined in isolated laboratory or simulation chamber studies could be successfully applied to ambient measurements. On the basis of this thesis the need for the determination of further s is given, since only the knowledge of the individual *RIE*s allow the absolute mass determination of individual species with an AMS. The high resolution analysis of specific fragmentation patterns allows the detection and quantification of important sub-species such as organic nitrate in ambient datasets. This approach is worth following for sub-division of other species such as sulfate. The scientific knowledge on the characteristics, composition, and behavior of atmospheric aerosol particles is still limited and demands for further extensive investigation.

# 7. Literature


Ahmed, F. R., and D. W. J. Cruickshank (1953), A refinement of the crystal structure analyses of oxalic acid dihydrate, *Acta Crystallographica*, *6*(5), 385-392.

Aiken, A. C., et al. (2009), Mexico City aerosol analysis during MILAGRO using high resolution aerosol mass spectrometry at the urban supersite (T0) -- Part 1: Fine particle composition and organic source apportionment, *Atmos. Chem. Phys.*, *9*(17), 6633-6653.

Alfarra, M. R. (2004), Insights Into Athmospheric Organic Aerosols Using An Aerosol Mass Spectrometer, 2000 pp, University of Manchester, Manchester.

Alfarra, M. R., et al. (2004), Characterization of urban and rural organic particulate in the Lower Fraser Valley using two Aerodyne Aerosol Mass Spectrometers, *Atmospheric Environment*

The Pacific 2001 Air Quality Study, 38(34), 5745-5758.

Alfarra, M. R., et al. (2006), A mass spectrometric study of secondary organic aerosols formed from the photooxidation of anthropogenic and biogenic precursors in a reaction

chamber, Atmospheric Chemistry and Physics, 6(12), 5279 - 5293.

Allan, J. D., et al. (2003), Quantitative sampling using an Aerodyne aerosol mass spectrometer - 2. Measurements of fine particulate chemical composition in two U.K. cities, *Journal of Geophysical Research-Atmospheres*, *108*(D3).

Allan, J. D., et al. (2004), A generalised method for the extraction of chemically resolved mass spectra from Aerodyne aerosol mass spectrometer data, *Journal of Aerosol Science*, *35*(7), 909-922.

Allan, J. D., et al. (2006), Size and composition measurements of background aerosol and new particle growth in a Finnish forest during QUEST 2 using an Aerodyne Aerosol Mass Spectrometer, *Atmos. Chem. Phys.*, *6*(2), 315-327.

Andreae, M. O., and A. Gelencsér (2006), Black carbon or brown carbon? The nature of light-absorbing carbonaceous aerosols, *Atmos. Chem. Phys.*, *6*(10), 3131-3148.

Atkinson, R. (1997), Gas-Phase Tropospheric Chemistry of Volatile Organic Compounds: 1. Alkanes and Alkenes, *Journal of Physical and Chemical Reference Data*, *26*(2), 215-290.

Atkinson, R., and J. Arey (2003), Gas-phase tropospheric chemistry of biogenic volatile organic compounds: a review, *Atmospheric Environment*, *37*(Supplement 2), 197-219.

Baxter, G. P., and J. E. Lansing (2002), The Aqueous Pressure of Some Hydrated Crystals. Oxalic Acid, Strontium Chloride and Sodium Sulfate, *Journal of the American Chemical Society*, *42*(3), 419-426.

Canagaratna, M. R., et al. (2004), Chase Studies of Particulate Emissions from in-use New York City Vehicles, *Aerosol Science and Technology*, *38*(6), 555 - 573.

Canagaratna, M. R., et al. (2007), Chemical and microphysical characterization of ambient aerosols with the aerodyne aerosol mass spectrometer, *Mass Spectrometry Reviews*, *26*(2), 185-222.

Crosier, J., et al. (2007), Chemical composition of summertime aerosol in the Po Valley (Italy), northern Adriatic and Black Sea, *Quarterly Journal of the Royal Meteorological Society*, *133*(S1), 61-75.

Day, D. A., et al. (2002), A thermal dissociation laser-induced fluorescence instrument for in situ detection of NO2, peroxy nitrates, alkyl nitrates, and HNO3, *J. Geophys. Res.*, *107*.

Day, D. A., et al. (2009), Observations of NOx, ΣPNs, ΣANs, and HNO3 at a Rural Site in the California Sierra Nevada Mountains: summertime diurnal cycles, *Atmos. Chem. Phys.*, *9*(14), 4879-4896.

DeCarlo, P., et al. (2004), Particle Morphology and Density Characterization by Combined Mobility and Aerodynamic Diameter Measurements. Part 1: Theory, *Aerosol Science and Technology*, *38*(12), 1185 - 1205.

DeCarlo, P. F., et al. (2006), Field-Deployable, High-Resolution, Time-of-Flight Aerosol Mass Spectrometer, *Anal. Chem.*

Dorn, H. P., et al. (2009), Intercomparison of NO3 measurement techniques at the simulation chamber SAPHIR, *Atmos. Chem. Phys.*, *in preparation*.

Drewnick, F., et al. (2004), Measurement of Ambient Aerosol Composition During the PMTACS-NY 2001 Using an Aerosol Mass Spectrometer. Part I: Mass Concentrations, *Aerosol Science and Technology*, *38*(12 supp 1), 92 - 103.

Drewnick, F., et al. (2005), A New Time-of-Flight Aerosol Mass Spectrometer (TOF-AMS): Instrument Description and First Field Deployment, *Aerosol Science & Technology*, *39*(7), 637-658.

Drewnick, F., et al. (2007), Measurement of Ambient, Interstitial, and Residual Aerosol Particles on a Mountaintop Site in Central Sweden using an Aerosol Mass Spectrometer and a CVI, *Journal of Atmospheric Chemistry*, *56*(1), 1-20.

Dubé, W. P., et al. (2006), Aircraft instrument for simultaneous, in situ measurement of NO3 and N2O5 via pulsed cavity ring-down spectroscopy, *Review of Scientific Instruments*, *77*(3), 034101-034111.

Ehn, M., et al. (2007), Hygroscopic properties of ultrafine aerosol particles in the boreal forest: diurnal variation, solubility and the influence of sulfuric acid, *Atmospheric Chemistry and Physics*, *7*(1), 211 - 222.

Finlayson-Pitts, B. J., and J. N. Pitts (2000), *Chemistry of the Upper and Lower Troposphere*, Academic Press, San Diego, USA.

Fisseha, R., et al. (2009), Determination of primary and secondary sources of organic acids and carbonaceous aerosols using stable carbon isotopes, *Atmospheric Environment*, *43*(2), 431-437.

Fry, J. L., et al. (2009), Organic nitrate and secondary organic aerosol yield from NO3 oxidation of β-pinene evaluated using a gas-phase kinetics/aerosol partitioning model, *Atmos. Chem. Phys.*, *9*(4), 1431-1449.

Fry, J. L., et al. (in preparation), Chemical production and loss of limonene secondary organic aerosol (SOA) by reaction with $NO_3$, *Atmos. Chem. Phys.*

Fuchs, H., et al. (2009), Intercomparison of measurements of NO2 concentrations in the atmosphere simulation chamber SAPHIR during the NO3Comp campaign, *Atmos. Meas. Tech. Discuss.*, *2*(5), 2539-2586.

Geyer, A., et al. (2003), Nighttime formation of peroxy and hydroxyl radicals during the BERLIOZ campaign: Observations and modeling studies, *J. Geophys. Res.*, *108*.

Griffin, R. J., et al. (1999), Organic aerosol formation from the oxidation of biogenic hydrocarbons, *Journal of Geophysical Research-Atmospheres*, *104*(D3), 3555-3567.

Guenther, A., et al. (1995), A global model of natural volatile organic compound emissions, *J. Geophys. Res.*, *100*(D5), 8873 - 8892.

Guenther, A., et al. (2006), Estimates of global terrestrial isoprene emissions using MEGAN (Model of Emissions of Gases and Aerosols from Nature), *Atmos. Chem. Phys.*, *6*(11), 3181-3210.

Gustafsson, O., et al. (2009), Brown Clouds over South Asia: Biomass or Fossil Fuel Combustion?, *Science*, *323*(5913), 495-498.

Hallquist, M., et al. (1999), Aerosol and Product Yields from NO3 Radical-Initiated Oxidation of Selected Monoterpenes, *Environmental Science & Technology*, *33*(4), 553-559.

Hallquist, M., et al. (2009), The formation, properties and impact of secondary organic aerosol: current and emerging issues, *Atmos. Chem. Phys.*, *9*(14), 5155-5235.

Hämeri, K., et al. (2001), Hygroscopic and CCN properties of aerosol particles in boreal forests, *Tellus B*, *53*(4), 359-379.

Hinds, W. C. (1999), *Aerosol Technology*, John Wiley & Sons, New York.

Hoffmann, T., et al. (1997), Formation of organic aerosols from the oxidation of biogenic hydrocarbons, *Journal of Atmospheric Chemistry*, *26*(2), 189-222.

Hogrefe, O., et al. (2004), Development, Operation and Applications of an Aerosol Generation, Calibration and Research Facility *Aerosol Science and Technology*, *38*(12 supp 1), 196 - 214.

Huffman, J. A., et al. (2005), Design, Modeling, Optimization, and Experimental Tests of a Particle Beam Width Probe for the Aerodyne Aerosol Mass Spectrometer., *Aerosol Science & Technology*, *39*(12), 1143-1163.

Huffman, J. A., et al. (2009), Chemically-resolved aerosol volatility measurements from two megacity field studies, *Atmos. Chem. Phys.*, *9*(18), 7161-7182.

IPCC (2007), Intergovernmental Panel on Climate Change: Climate Change 2007: The Physical Science Basis, Cambrige University Press, UK, 2007.

Jayne, J. T., et al. (2000), Development of an aerosol mass spectrometer for size and composition analysis of submicron particles, *Aerosol Science and Technology*, *33*(1-2), 49-70.

Jeffrey, G. A., and G. S. Parry (1954), The Crystal Structure of Sodium Oxalate, *Journal of the American Chemical Society*, *76*(21), 5283-5286.

Jimenez, J. L., et al. (2003), Ambient aerosol sampling using the Aerodyne Aerosol Mass Spectrometer, *Journal of Geophysical Research-Atmospheres*, *108*(D7).

Jimenez, J. L., et al. (2009), Evolution of Organic Aerosols in the Atmosphere, *Science*, *326*(5959), 1525-1529.

Johnson, D. L., et al. (1987), Drag on non-spherical, orthotropic aerosol particles, *Journal of Aerosol Science*, *18*(1), 87-97.

Kanakidou, M., et al. (2005), Organic aerosol and global climate modelling: a review, *Atmos. Chem. Phys.*, *5*(4), 1053-1123.

Kawamura, K., and F. Sakaguchi (1999), Molecular distributions of water soluble dicarboxylic acids in marine aerosols over the Pacific Ocean including tropics, *J. Geophys. Res.*, *104*(D 3), 3501 - 3509.

Khwaja, H. A. (1995), Atmospheric concentrations of carboxylic acids and related compounds at a semiurban site, *Atmospheric Environment*, *29*(1), 127-139.

Koehler, K. A., et al. (2006), Water activity and activation diameters from hygroscopicity data - Part II: Application to organic species, *Atmospheric Chemistry and Physics*, *6*, 795-809.

Kulmala, M., et al. (2009), Introduction: European Integrated Project on Aerosol Cloud Climate and Air Quality interactions (EUCAARI) - integrating aerosol research from nano to global scales, *Atmos. Chem. Phys.*, *9*(8), 2825-2841.

Lanz, V. A., et al. (2007), Source apportionment of submicron organic aerosols at an urban site by factor analytical modelling of aerosol mass spectra, *Atmos. Chem. Phys.*, *7*(6), 1503-1522.

Lanz, V. A., et al. (2008), Source Attribution of Submicron Organic Aerosols during Wintertime Inversions by Advanced Factor Analysis of Aerosol Mass Spectra, *Environmental Science & Technology*, *42*(1), 214-220.

Lide, D. R. (Ed.) (2009), *CRC Handbook of Chemistry and Physics*, 89 ed., CRC Press/Taylor and Francis, Boca Ralton.

Lindinger, W., et al. (1998), Proton-transfer-reaction mass spectrometry (PTR-MS): on-line monitoring of volatile organic compounds at pptv levels, *Chemical Society Reviews*, *27*(5), 347-354.

Liu, P., et al. (1995a), Generating Particle Beams of Controlled Dimensions and Divergence: II. Experimental Evaluation of Particle Motion in Aerodynamic Lenses and Nozzle Expansions, *Aerosol Science & Technology*, *22*(3), 314-324.

Liu, P., et al. (1995b), Generating Particle Beams of Controlled Dimensions and Divergence: I. Theory of Particle Motion in Aerodynamic Lenses and Nozzle Expansions, *Aerosol Science & Technology*, *22*(3), 293-313.

Liu, P. S. K., et al. (2007), Transmission Efficiency of an Aerodynamic Focusing Lens System: Comparison of Model Calculations and Laboratory Measurements for the Aerodyne Aerosol Mass Spectrometer, *Aerosol Science and Technology*, *41*(8), 721 - 733.

Matthew, B. M., et al. (2008), Collection Efficiencies in an Aerodyne Aerosol Mass Spectrometer as a Function of Particle Phase for Laboratory Generated Aerosols, *Aerosol Science and Technology*, *42*(11), 884 - 898.

McLafferty, F. W., and F. Turecek (1993), *Interpretation of Mass Spectra*, University Science Books, Sausolito.

Mielniczek-Brzóska, E., and K. Sangwal (1995), Study of the Growth Morphology of Ammonium Oxalate Monohydrate Crystals Obtained from Aqueous Solutions, *Crystal Research and Technology*, *30*(6), 807-811.

Mohr, C., et al. (2009), Characterization of Primary Organic Aerosol Emissions from Meat Cooking, Trash Burning, and Motor Vehicles with High-Resolution Aerosol Mass Spectrometry and Comparison with Ambient and Chamber Observations, *Environmental Science & Technology*, *43*(7), 2443-2449.

Moolgavkar, S. H., et al. (1994), Air Pollution and Mortality, *The New England Journal of Medicine*, *330*(17), 1237-1238.

Nazarenko, L., and S. Menon (2005), Varying trends in surface energy fluxes and associated climate between 1960 and 2002 based on transient climate simulations, *Geophysical Research Letters*, *32*(22).

Neusüß, C., et al. (2002), Characterization and parameterization of atmospheric particle number-, mass-, and chemical-size distributions in central Europe during LACE 98 and MINT, *J. Geophys. Res.*, *107*(D21).

Nober, F. J., et al. (2003), Sensitivity of the global circulation to the suppression of precipitation by anthropogenic aerosols, *Global and Planetary Change*

Evaluation, Intercomparison and Application of Global Climate Models, 37(1-2), 57-80.

Norris, J. R., and M. Wild (2007), Trends in aerosol radiative effects over Europe inferred from observed cloud cover, solar "dimming" and solar "brightening", *Journal of Geophysical Research-Atmospheres*, *112*(D8).

Paatero, P., and U. Tapper (1994), Positive matrix factorization: A non-negative factor model with optimal utilization of error estimates of data values, *Environmetrics*, *5*(2), 111-126.

Paatero, P. (1997), Least squares formulation of robust non-negative factor analysis, *Chemometrics and Intelligent Laboratory Systems*, *37*(1), 23-35.

Peng, C., and C. K. Chan (2001), The water cycles of water-soluble organic salts of atmospheric importance, *Atmospheric Environment*, *35*(7), 1183-1192.

Peng, C., et al. (2001), The Hygroscopic Properties of Dicarboxylic and Multifunctional Acids: Measurements and UNIFAC Predictions, *Environmental Science & Technology*, *35*(22), 4495-4501.

Petzold, A., and M. Schönlinner (2004), Multi-angle absorption photometry - a new method for the measurement of aerosol light absorption and atmospheric black carbon, *Journal of Aerosol Science*, *35*(4), 421-441.

Pope , C. A., et al. (2002), Lung Cancer, Cardiopulmonary Mortality, and Long-term Exposure to Fine Particulate Air Pollution, *JAMA*, *287*(9), 1132-1141.

Prenni, A. J., et al. (2001), The Effects of Low Molecular Weight Dicarboxylic Acids on Cloud Formation, *The Journal of Physical Chemistry A*, *105*(50), 11240-11248.

Putaud, J.-P., et al. (2004), A European aerosol phenomenology--2: chemical characteristics of particulate matter at kerbside, urban, rural and background sites in Europe, *Atmospheric Environment*, *38*(16), 2579-2595.

Quinn, P. K., et al. (2006), Impacts of sources and aging on submicrometer aerosol properties in the marine boundary layer across the Gulf of Maine, *Journal of Geophysical Research*, *111*(D23).

Ramanathan, V., et al. (2007), Atmospheric brown clouds: Hemispherical and regional variations in long-range transport, absorption, and radiative forcing, *Journal of Geophysical Research-Atmospheres*, *112*(D22).

Reff, A., et al. (2007), Receptor modeling of ambient particulate matter data using positive matrix factorization: Review of existing methods, *Journal of the Air & Waste Management Association*, *57*(2), 146-154.

Reimer, D. (2007), Umgang mit dem Quadrupol-Aerosolmassenspektrometer un Aerosolkammer-Untersuchungen, Praktikumsbericht (Spezialpraktikum), Forschungszentrum Jülich, ICG-2, Jülich.

Ridley, B. A., et al. (1992), A Small High-Sensitivity, Medium-Response Ozone Detector Suitable for Measurements from Light Aircraft, *Journal of Atmospheric and Oceanic Technology*, *9*(2), 142-148.

Roelofs, G.-J., et al. (in preparation), Simulation of aerosol optical thickness during IMPACT (MAY 2008, The Netherlands) with ECHAM5/HAM

Rogge, W. F., et al. (1993), Quantification of urban organic aerosols at a molecular level: Identification, abundance and seasonal variation, *Atmospheric Environment. Part A. General Topics*, *27*(8), 1309-1330.

Rollins, A. W., et al. (2009), Isoprene oxidation by nitrate radical: alkyl nitrate and secondary organic aerosol yields, *Atmos. Chem. Phys.*, *9*(18), 6685-6703.

Romanou, A., et al. (2007), 20th century changes in surface solar irradiance in simulations and observations, *Geophysical Research Letters*, *34*(5).

Russchenberg, H., et al. (2005), Ground-Based Atmospheric Remote Sensing in the Netherlands: European Outlook, *The Institute of Electronics, Information and Communication Engineers*, *E88–B*(6).

Saunders, S. M., et al. (2003), Protocol for the development of the Master Chemical Mechanism, MCM v3 (Part A): tropospheric degradation of non-aromatic volatile organic compounds, *Atmos. Chem. Phys.*, *3*(1), 161-180.

Saxena, P., and L. M. Hildemann (1996), Water-soluble organics in atmospheric particles: A critical review of the literature and application of thermodynamics to identify candidate compounds, *Journal of Atmospheric Chemistry*, *24*(1), 57-109.

Schichtel, B. A., et al. (2008), Fossil and contemporary fine particulate carbon fractions at 12 rural and urban sites in the United States, *J. Geophys. Res.*, *113*.

Schlosser, E., et al. (2007), Intercomparison of Two Hydroxyl Radical Measurement Techniques at the Atmosphere Simulation Chamber SAPHIR, *Journal of Atmospheric Chemistry*, *56*(2), 187-205.

Schneider, J., et al. (2006), Mass spectrometric analysis and aerodynamic properties of various types of combustion-related aerosol particles, *International Journal of Mass Spectrometry*, *258*(1-3), 37-49.

Sempére, R., and K. Kawamura (1994), Comparative distributions of dicarboxylic acids and related polar compounds in snow, rain and aerosols from urban atmosphere, *Atmospheric Environment*, *28*(3), 449-459.

Skov, H., et al. (1992), Products and mechanisms of the reactions of the nitrate radical (NO3) with isoprene, 1,3-butadiene and 2,3-dimethyl-1,3-butadiene in air, *Atmospheric Environment. Part A. General Topics*, *26*(15), 2771-2783.

Slanina, J., et al. (2001), The continuous analysis of nitrate and ammonium in aerosols by the steam jet aerosol collector (SJAC): extension and validation of the methodology, *Atmospheric Environment*, *35*(13), 2319-2330.

Sun, J., and P. A. Ariya (2006), Atmospheric organic and bio-aerosols as cloud condensation nuclei (CCN): A review, *Atmospheric Environment*, *40*(5), 795-820.

Tao, W. K., et al. (2007), Role of atmospheric aerosol concentration on deep convective precipitation: Cloud-resolving model simulations, *Journal of Geophysical Research-Atmospheres*, *112*(D24).

ten Brink, H., et al. (2007), An instrument for semi-continuous monitoring of the size-distribution of nitrate, ammonium, sulphate and chloride in aerosol, *Atmospheric Environment*, *41*(13), 2768-2779.

ten Brink, H., et al. (2009), Monitoring of the ratio of nitrate to sulphate in size-segregated submicron aerosol in the Netherlands, *Atmospheric Research*, *92*(2), 270-276.

ten Brink, H. M., et al. (1997), Composition/size of the light-scattering aerosol in the Netherlands, *Atmospheric Environment*, *31*(23), 3955-3962.

Trebs, I., et al. (2004), Real-time measurements of ammonia, acidic trace gases and water-soluble inorganic aerosol species at a rural site in the Amazon Basin, *Atmos. Chem. Phys.*, *4*(4), 967-987.

Ulbrich, I. M., et al. http://cires.colorado.edu/jimenez-group/AMSsd/

Ulbrich, I. M., et al. (2009), Interpretation of organic components from Positive Matrix Factorization of aerosol mass spectrometric data, *Atmos. Chem. Phys.*, *9*(9), 2891-2918.

Van Dingenen, R., et al. (2004), A European aerosol phenomenology--1: physical characteristics of particulate matter at kerbside, urban, rural and background sites in Europe, *Atmospheric Environment*, *38*(16), 2561-2577.

Vaughan T. J. Phillips, T. W. C., Alan M. Blyth, John Latham, (2002), The influence of aerosol concentrations on the glaciation and precipitation of a cumulus cloud, *Quarterly Journal of the Royal Meteorological Society*, *128*(581), 951-971.

Volkamer, R., et al. (2006), Secondary organic aerosol formation from anthropogenic air pollution: Rapid and higher than expected, *Geophysical Research Letters*, *33*.

Weber, R. J., et al. (2007), A study of secondary organic aerosol formation in the anthropogenic-influenced southeastern United States, *J. Geophys. Res.*, *112*.

Yu, S. (2000), Role of organic acids (formic, acetic, pyruvic and oxalic) in the formation of cloud condensation nuclei (CCN): a review, *Atmospheric Research*, *53*(4), 185-217.

Zhang, Q., et al. (2005), Deconvolution and Quantification of Hydrocarbon-like and Oxygenated Organic Aerosols Based on Aerosol Mass Spectrometry, *Environ. Sci. Technol.*, *39*(13), 4938-4952.

Zhang, Q., et al. (2007), Ubiquity and dominance of oxygenated species in organic aerosols in anthropogenically-influenced Northern Hemisphere midlatitudes, *Geophys. Res. Lett.*, *34*(13).

Zhang, X., et al. (2004), Numerical Characterization of Particle Beam Collimation: Part II Integrated Aerodynamic-Lens-Nozzle System, *Aerosol Science and Technology*, *38*(6), 619 - 638.

# Appendix

## A.1 Data Analysis

### A.1.1 Software used

2008: Squirrel 1.44, Pika 1.06, PMF 2.03A

2009: Squirrel 1.47, Pika 1.06, PMF 2.03A

### A.1.2 *m*/*z* Fitting

List of masses (Diff spectra) used in 2008 and 2009:

$C^+$, $N^+$, $O^+$, $O_2^+$, $Ar^+$, $^{182}W^+$, $^{184}W^+$, $^{186}W^+$

### A.1.3 Baseline

Mass defect wave set to CH

R0 = 420

Table A 1 Changed center peak positions in baseline correction in 2008 and 2009 (*only).

| m/z | m/z | m/z |
|---|---|---|
| 79.0650 | 130.0500 | 150.1300 |
| 80.000 | 132.0500 | 242.000 |
| 81.0300 | 133.025 | 244.0600 |
| 85.0180 | 134.0300 | 246.0600 |
| 87.0050 | 136.0300 | 474.3850 |
| 98.0400 | 138.0400 | |
| 127.0400* | 149.0500 | |

### A.1.4 DC marker

Region 1: 166 µs – 1250 µs

Region 2: 4980 µs – 5520 µs

DC marker for *m*/*z* 30 set to region 2 only

### A.1.5 Fragmentation Wave

Table A 2 Fragmentation wave correction factors applied in 2008.

| m/z | frag_air | frag_CO2 | frag_O16 | frag_RH | frag_organic |
|---|---|---|---|---|---|
| 16 | | | 0.82153 | | |
| 18 | | | | 2.83e-4*RH | |
| 29 | 0.923995 | | | | |
| 33 | | | | | 33, -frag_air[33] |
| 34 | | | | | 34, -frag_air[34] |
| 40 | 1.20714 | | | | 40, -frag_air[40] |
| 44 | | 0.977237 | | | |

Table A 3 Fragmentation wave correction factors applied in 2009.

| m/z | frag_air | frag_CO2 | frag_O16 | frag_RH | frag_organic |
|---|---|---|---|---|---|
| 16 | | | 0.92068 | | |
| 18 | | | | 1.22e-4*RH | |
| 29 | 0.926238 | | | | |
| 33 | | | | | 33, -frag_air[33] |
| 34 | | | | | 34, -frag_air[34] |
| 40 | 1.23229 | | | | 40, -frag_air[40] |
| 44 | | 1.07484 | | | |

### A.1.6 High Resolution Fitting

2008:

peak width fitting on $C^+$, $N^+$, $O^+$, $O_2^+$, and $Ar^+$

peak shape:

V-mode: $Ar^+$ (28.04.-13.05.) and $O^+$ (13.05.-30.05)

W-mode: $Ar^+$ (28.04.-26.05.) and $O^+$ (26.05.-30.05)

Table A 4 Peak width and peak shape parameters for 2009

| week | | 24.02.09 – 03-03-09: | 09.03.09 – 17.03.09 | 17.03.09 – 25.03.09 |
|---|---|---|---|---|
| WIDTH | V | C, CH, OH, $C_2H$, $N_2$, $O_2$, Ar, SO, $SO_2$, $C_8H_5O_3$, W182<br>(0.9692 + 0.0158 · *m/z*) | C, CH, OH, $C_2H$, $N_2$, $O_2$, Ar, SO, $SO_2$, $C_8H_5O_3$, W182<br>(1.0527 + 0.0126 · *m/z*) | C, CH, OH, $C_2H$, $N_2$, $O_2$, Ar, SO, $SO_2$, $C_8H_5O_3$, W182<br>(1.056 + 0.0127 · *m/z*) |
| | W | C, CH, OH, $C_2H$, N2, $O_2$, Ar, SO, $SO_2$, W182<br>(1.1019 + 0.0188 · *m/z*) | C, CH, OH, $C_2H$, $N_2$, $O_2$, Ar, SO, $SO_2$, W182<br>(1.1696 + 0.0182 · *m/z*) | C, CH, OH, $C_2H$, $N_2$, $O_2$, Ar, SO, $SO_2$, W182<br>(1.1643 + 0.0194 · *m/z*) |
| SHAPE | V | average of all masses for both wings | left wing: C;CH;OH;$C_2H$; $O_2$;Ar;SO;W182<br>right wing: C;CH;OH;$C_2H$; $N_2$;$O_2$;W182; | left wing: C;CH; OH;$C_2H$;$N_2$;$O_2$;Ar;SO;$SO_2$<br>right wing: C;CH;OH;$C_2H$; $N_2$;$O_2$ |
| | W | left wing: C;CH;OH;$C_2H$; $O_2$;Ar;SO;W182<br>right wing: C;CH;OH;$N_2$; $O_2$;Ar;SO;$SO_2$ | left wing: C;OH;$C_2H$; $O_2$;Ar;SO;W182;<br>right wing: C;CH;OH; $C_2H$;N2;$O_2$;Ar;$SO_2$ | left wing: C;CH;OH;$C_2H$; $O_2$;Ar;SO;$SO_2$;W182<br>right wing: C;OH;$N_2$; $O_2$;Ar |

# A.2 AMS Data

## A.2.1 Batch Diurnals

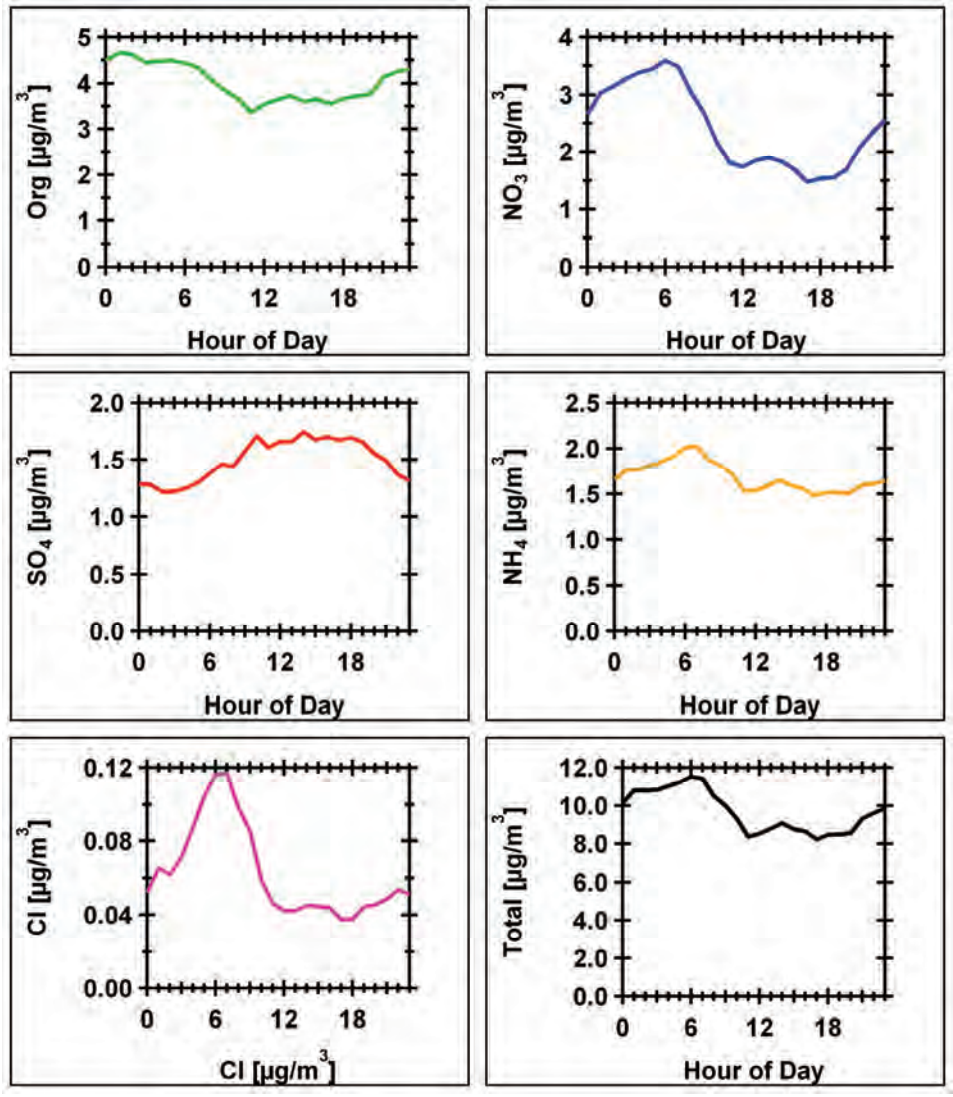


Figure A 1 Diurnal averages in 2008

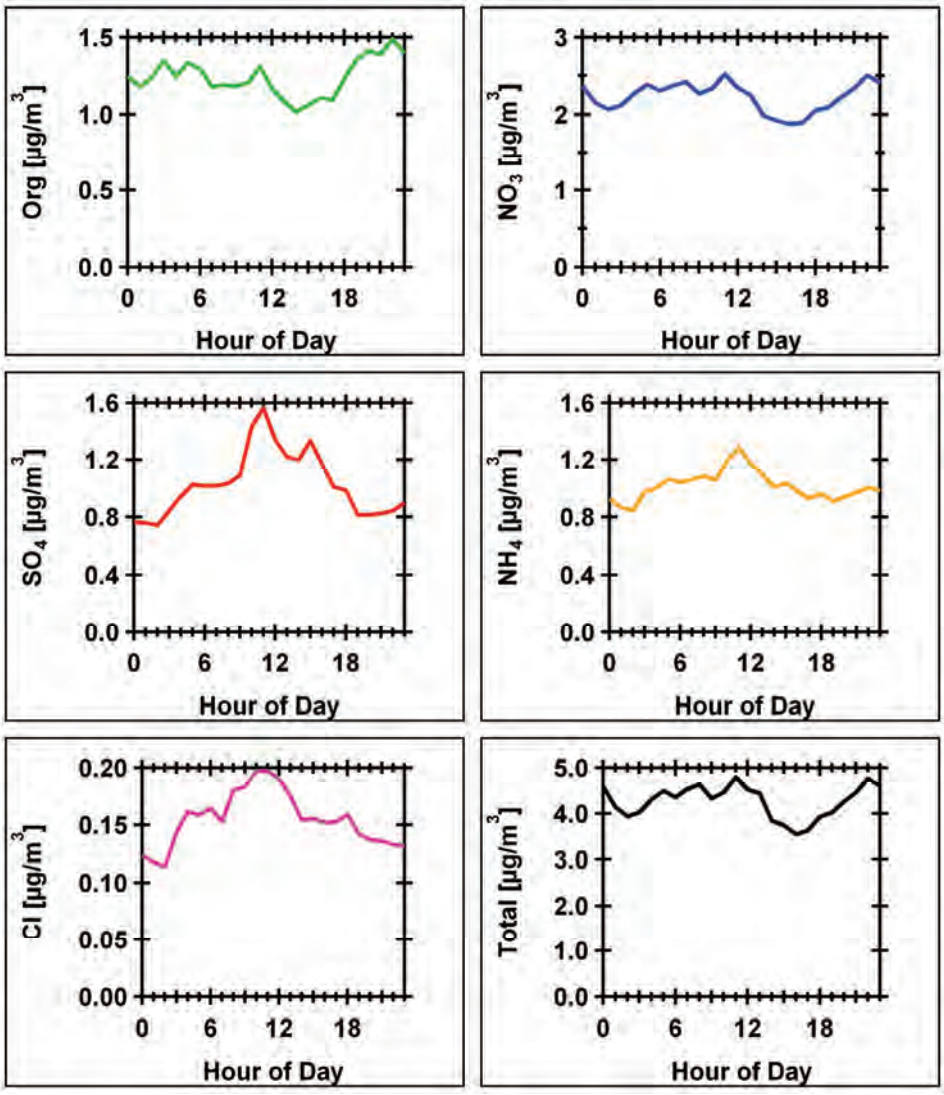


Figure A 2 Diurnal averages in 2009

### A.2.2 Size Distributions

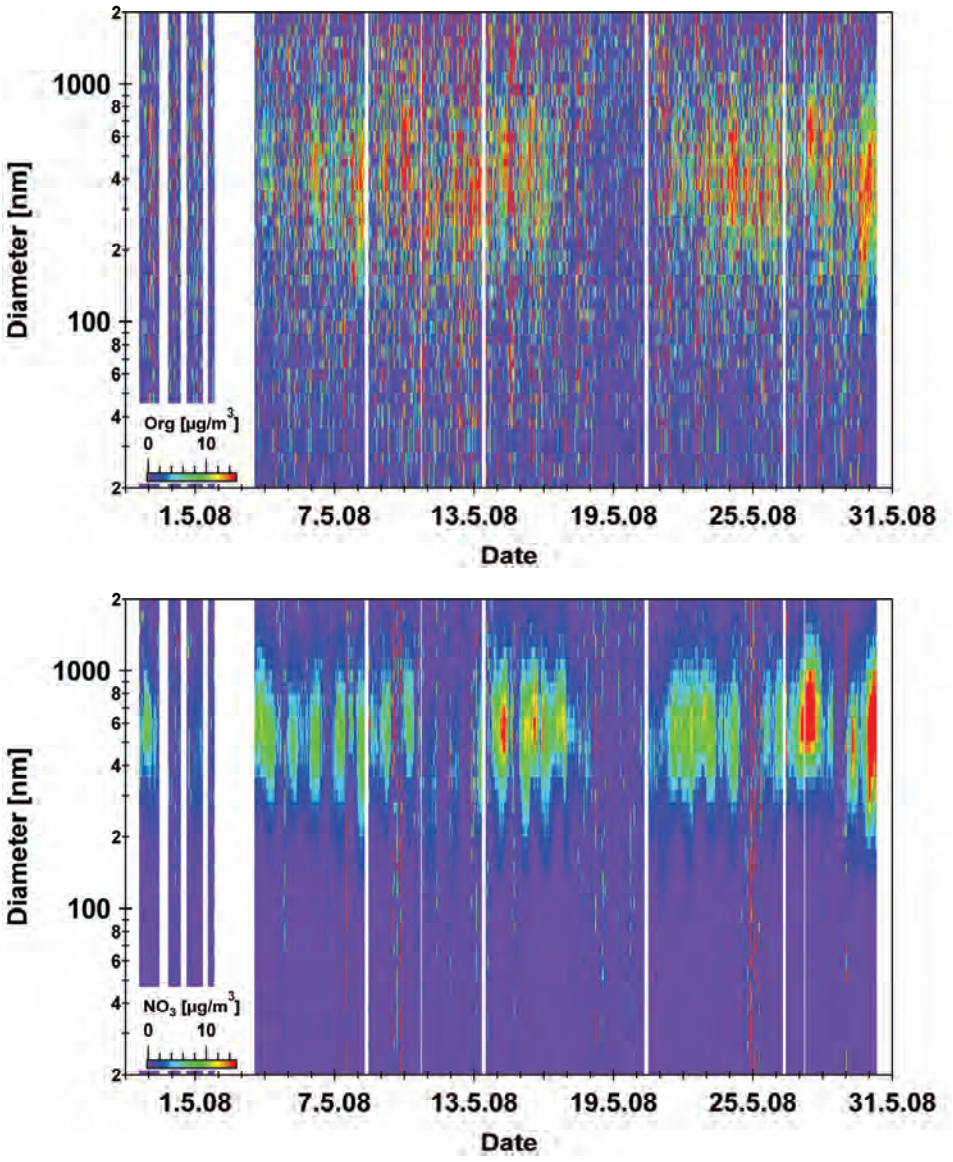


Figure A 3 Size distribution image plots of organic and nitrate in 2008.

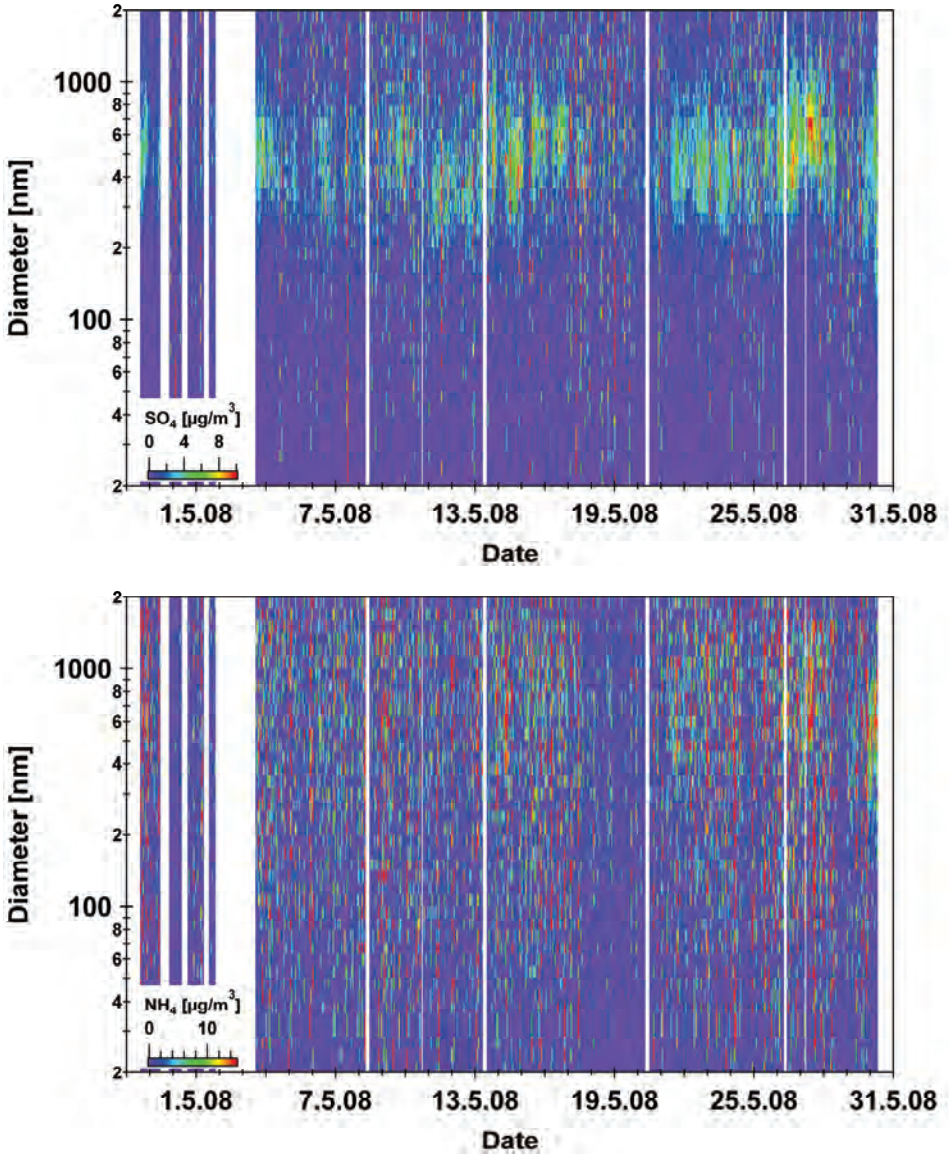


Figure A 4 Size distribution image plots of sulfate and ammonium in 2008.

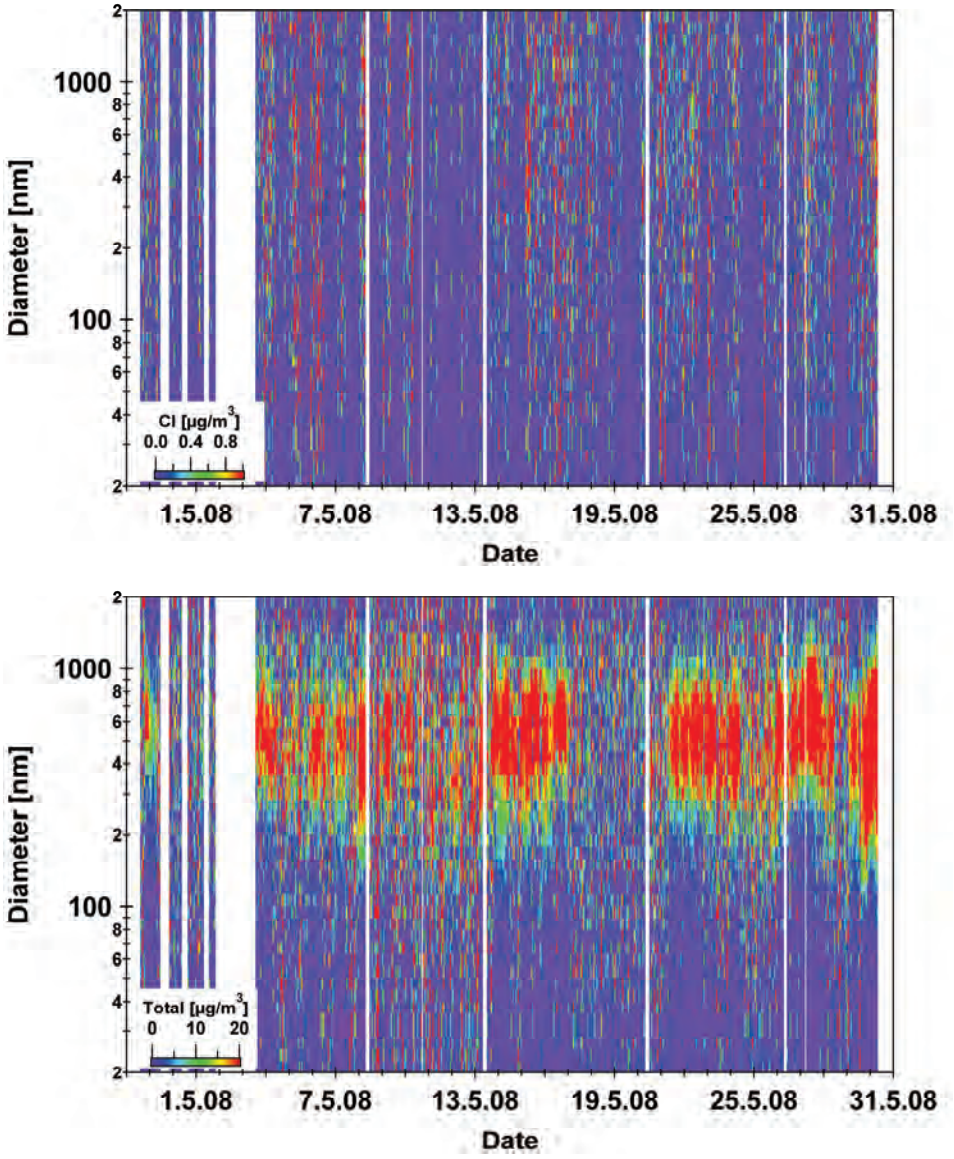


Figure A 5 Size distribution image plots of chloride and total in 2008.

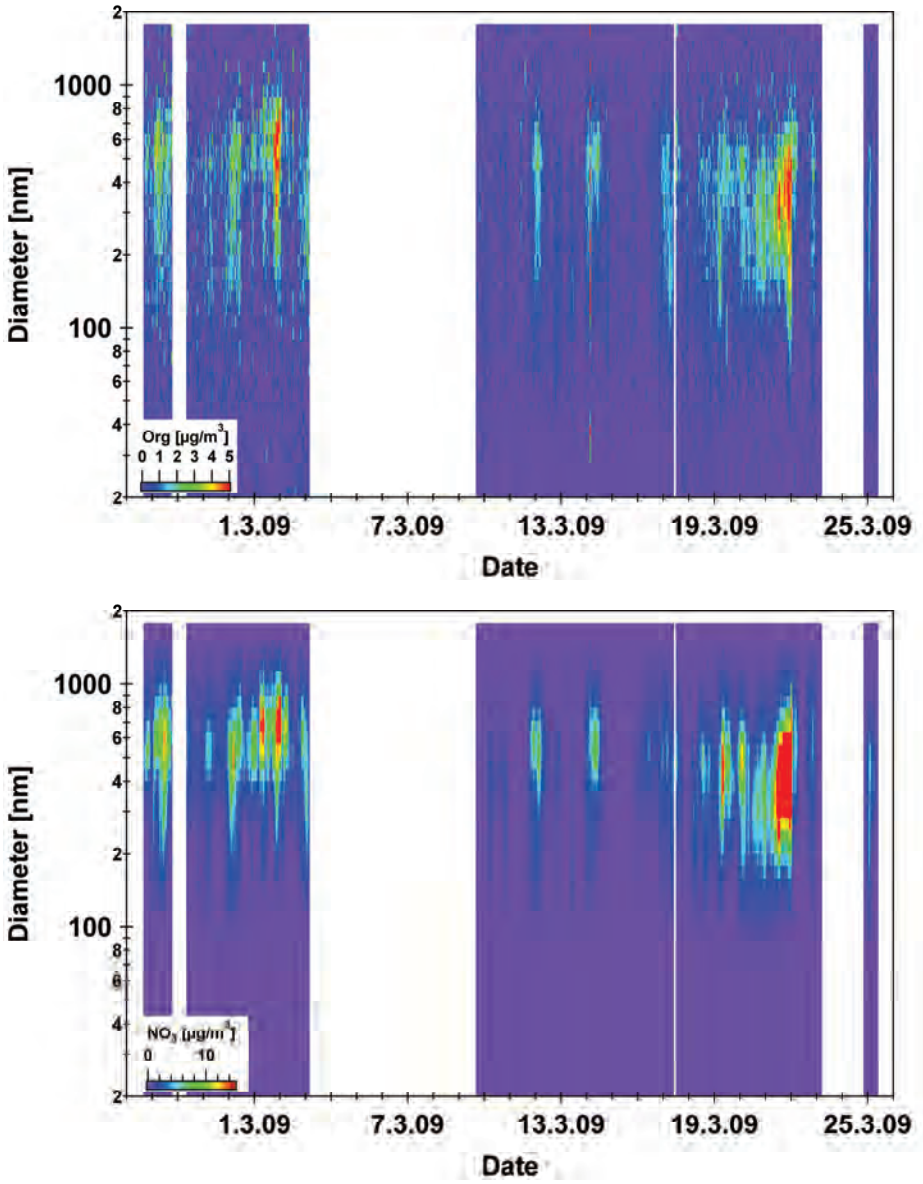


Figure A 6 Size distribution image plots of organic and nitrate in 2008.

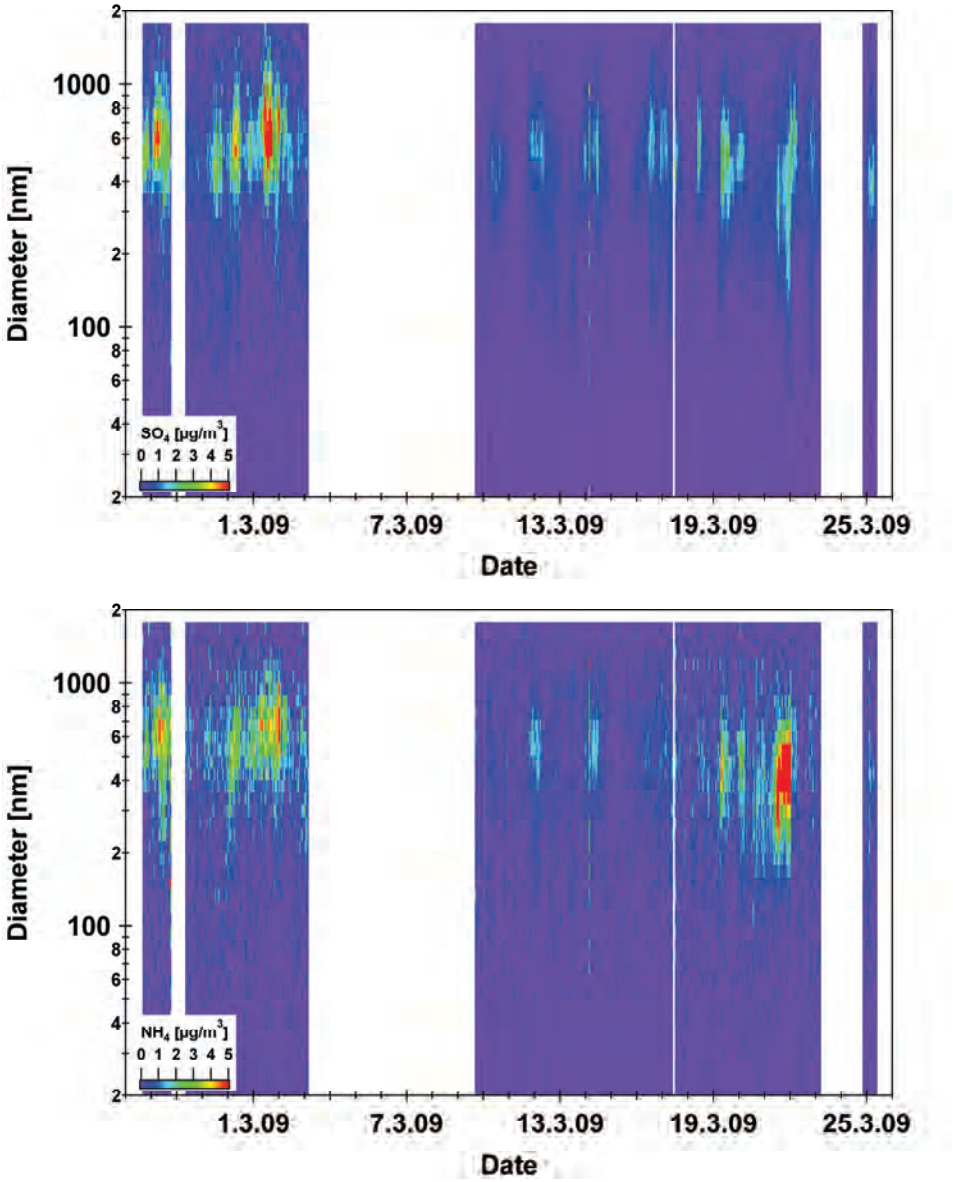


Figure A 7 Size distribution image plots of sulfate and ammonium in 2009.

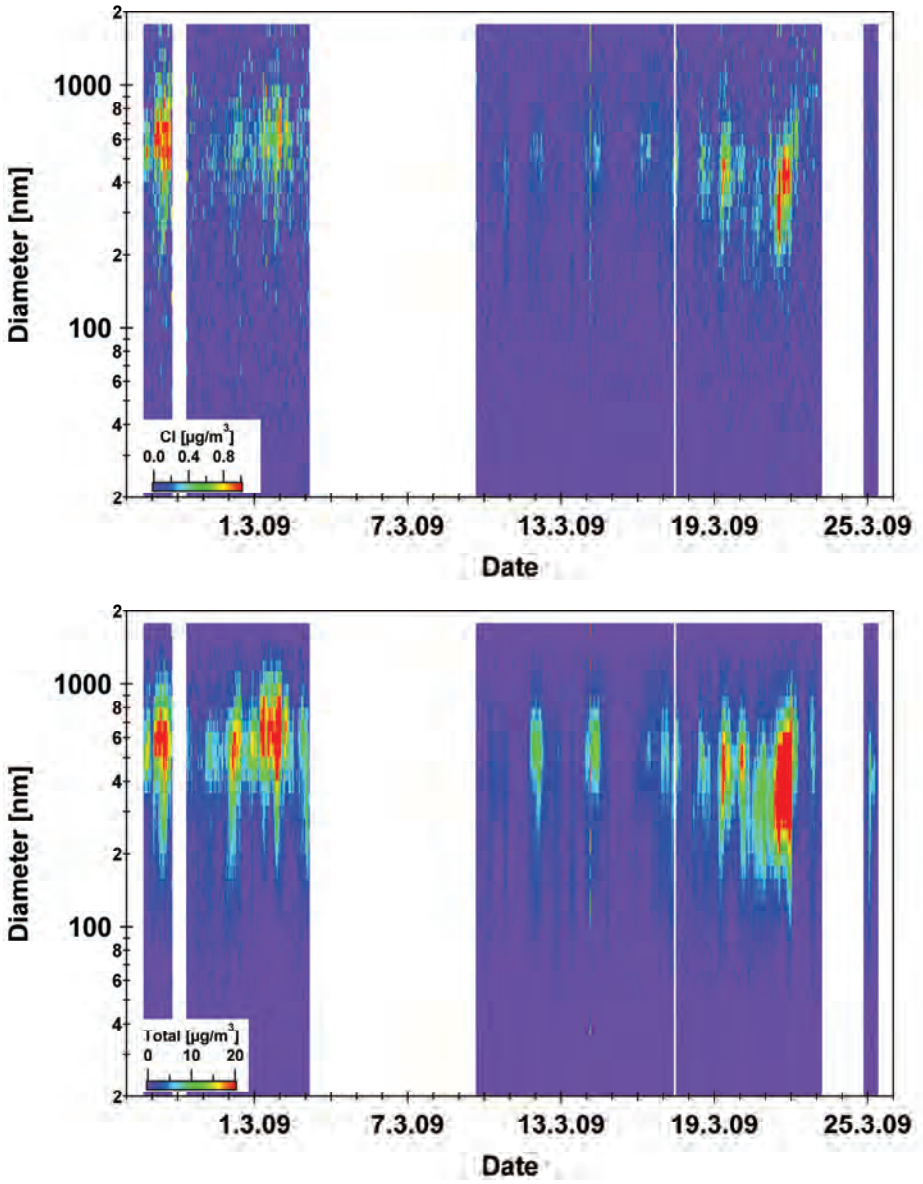


Figure A 8 Size distribution image plots of chloride and total in 2009.

# A.3 Comparison

## A.3.1 SMPS

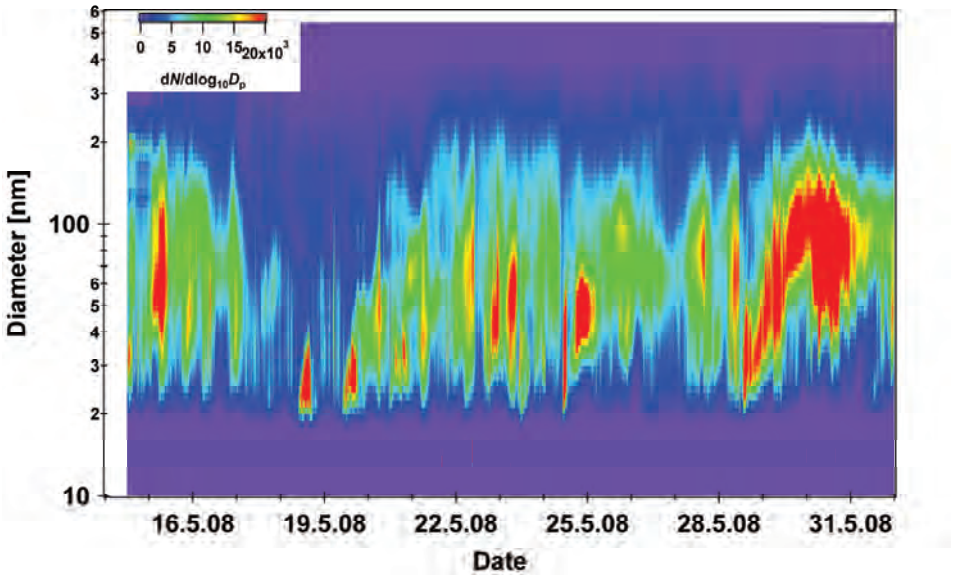


Figure A 9 SMPS particle size distribution in May 2008.

## A.3.2 MARGA 2008

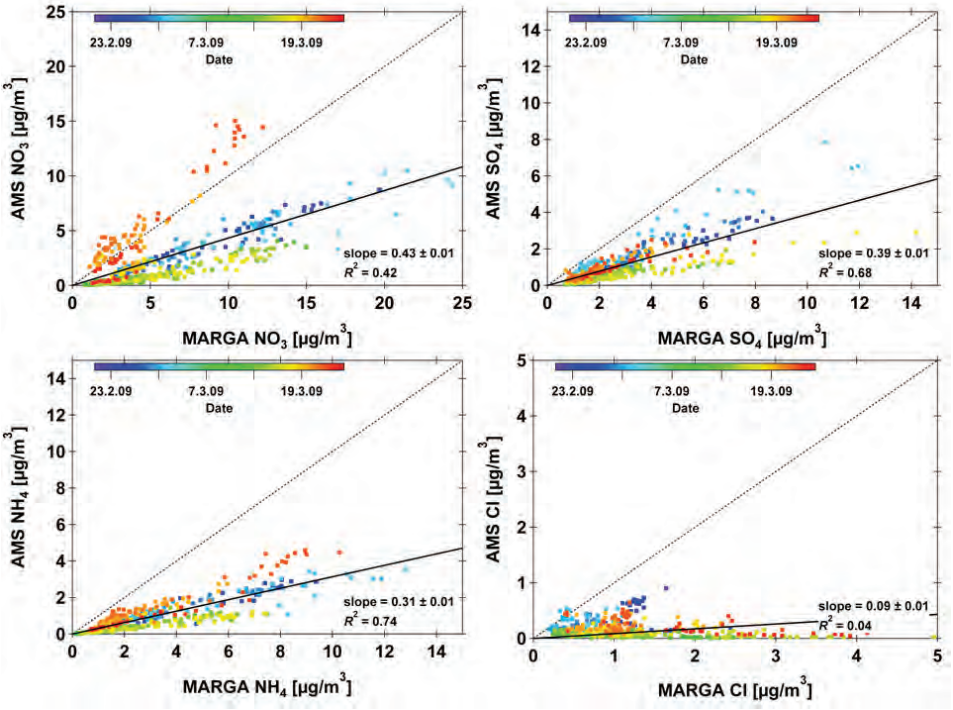


Figure A 10 Correlation AMS inorganic species to MARGA data in 2008.

### A.3.3 MARGA 2009

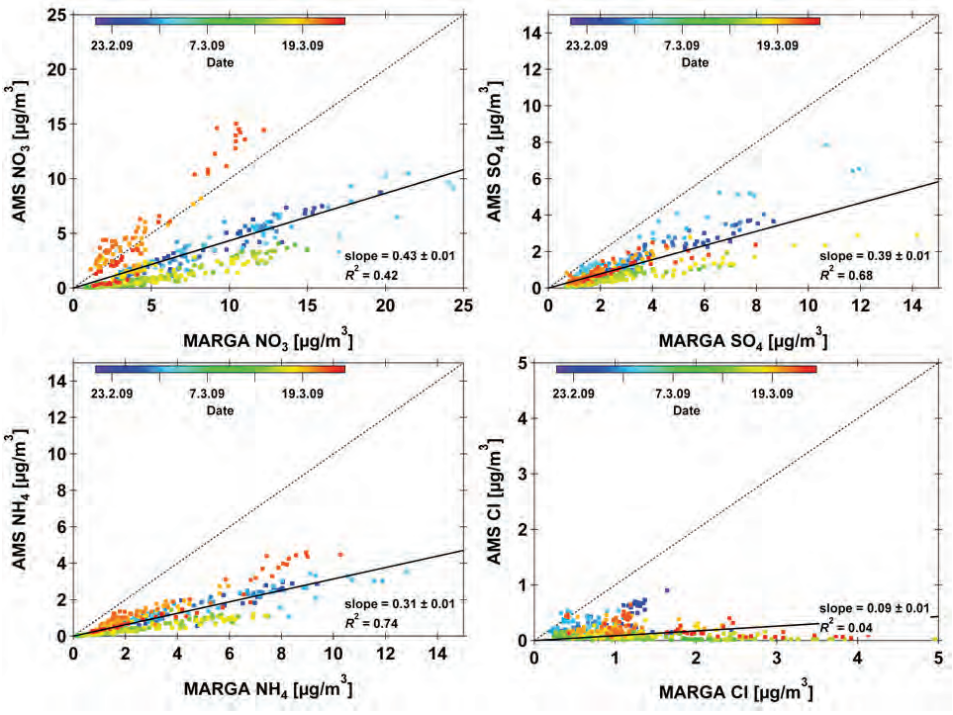


Figure A 11 Correlation AMS inorganic species to MARGA data in 2009.

### A.3.4 MARGA Sizer

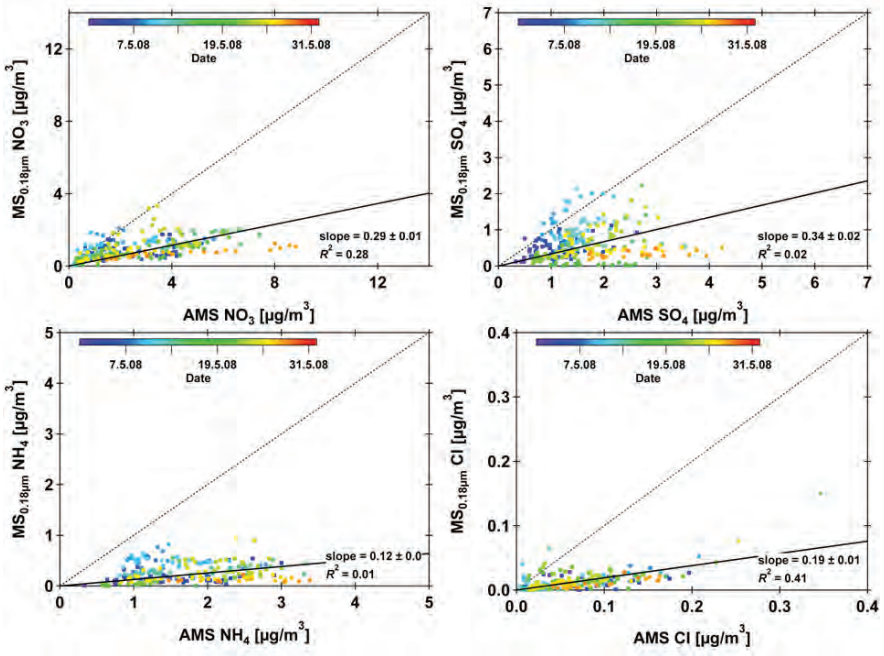


Figure A 12 Correlation AMS inorganic species to MARGA Sizer PM(0.18 µm) data in 2008.

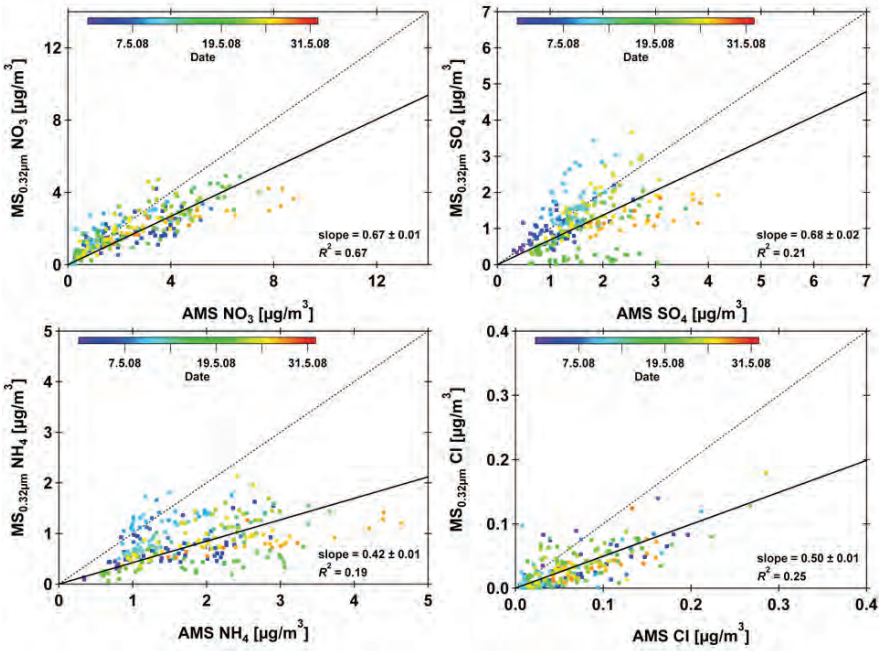


Figure A 13 Correlation AMS inorganic species to MARGA Sizer PM(0.32 µm) data in 2008.

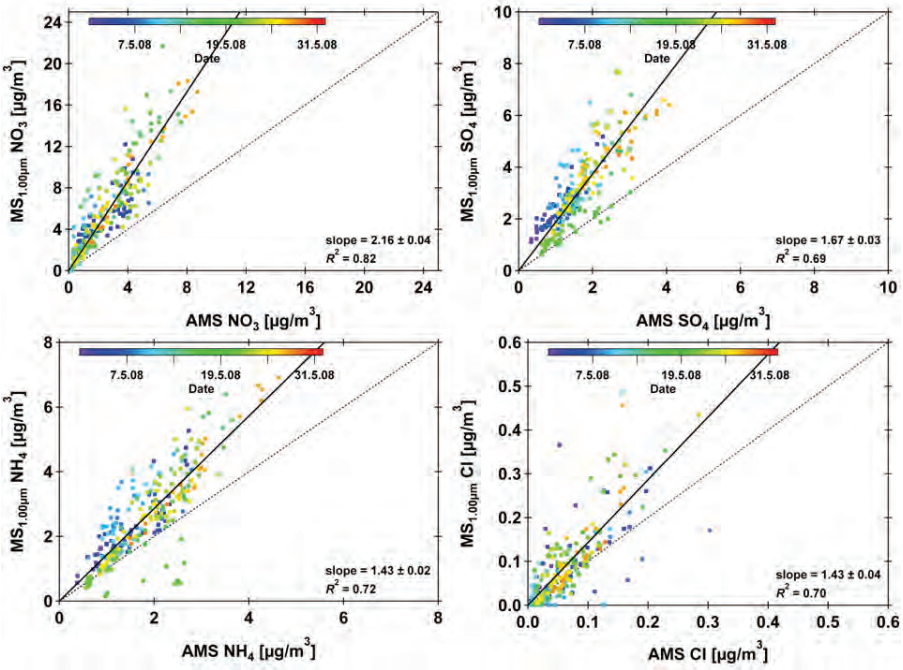


Figure A 14 Correlation AMS inorganic species to MARGA Sizer PM(1.00 µm) data in 2008.

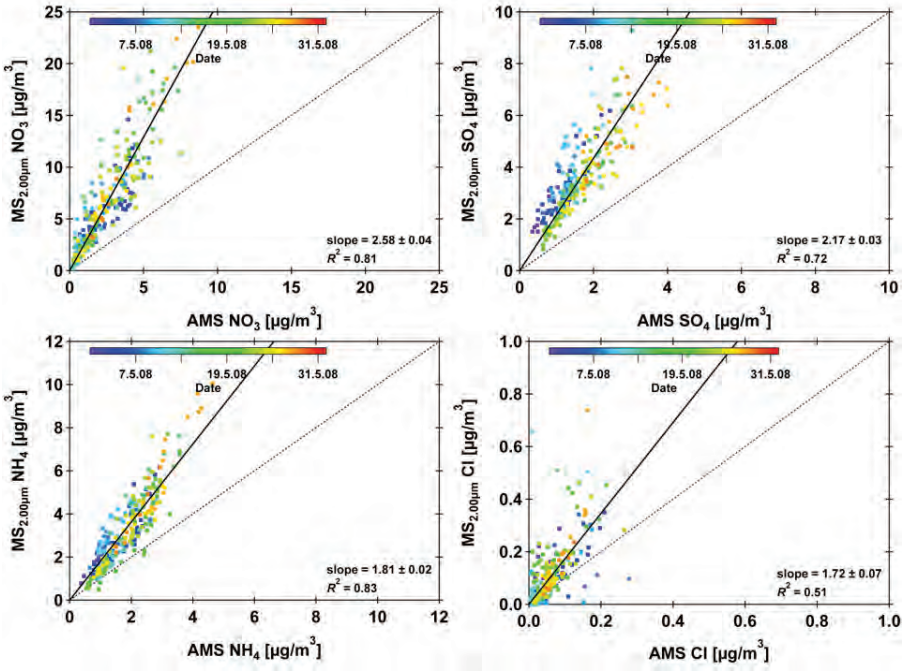


Figure A 15 Correlation AMS inorganic species to MARGA Sizer PM(2.00 µm) data in 2008.

## A.4 PMF Data

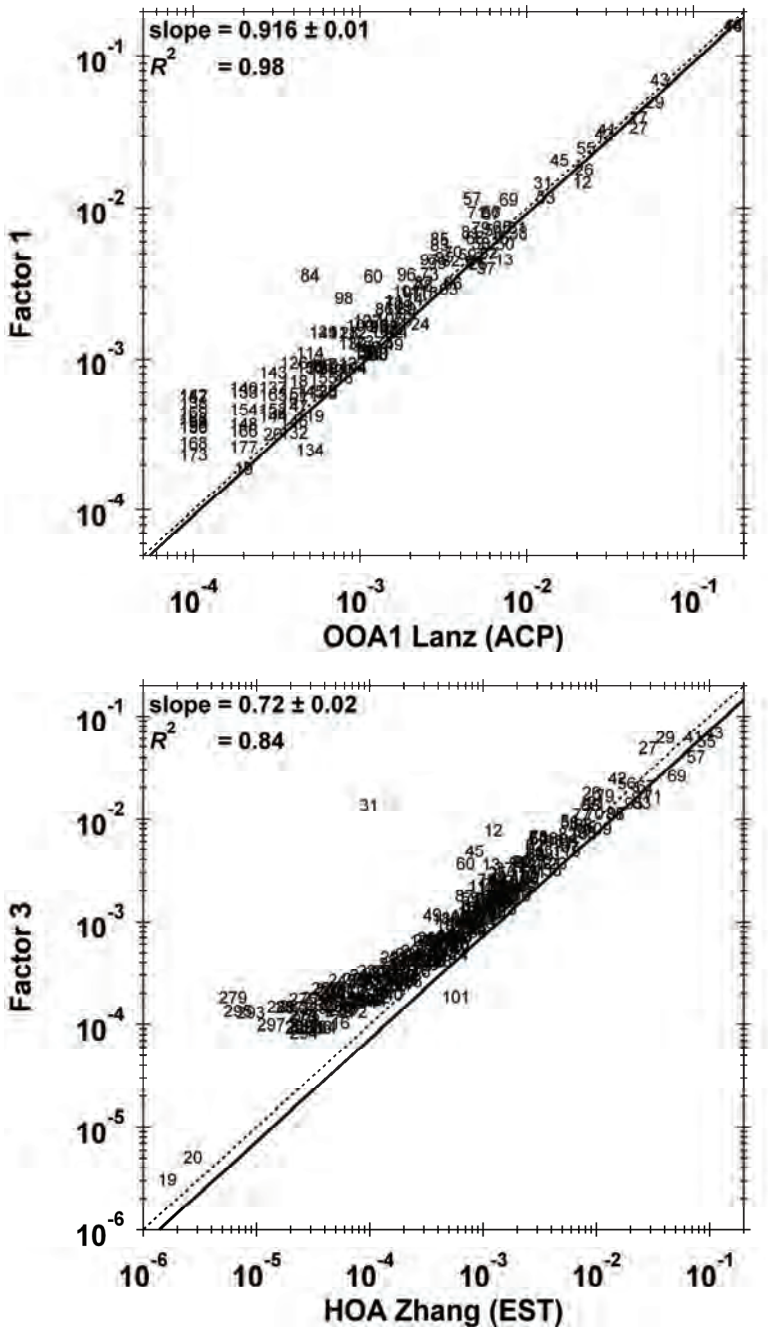


Figure A 16 Correlation of PMF factor 1 MS to OOA1 MS from [*Lanz et al.*, 2008] (top) and factor 3 MS to HOA MS from [*Zhang et al.*, 2005] in 2008.

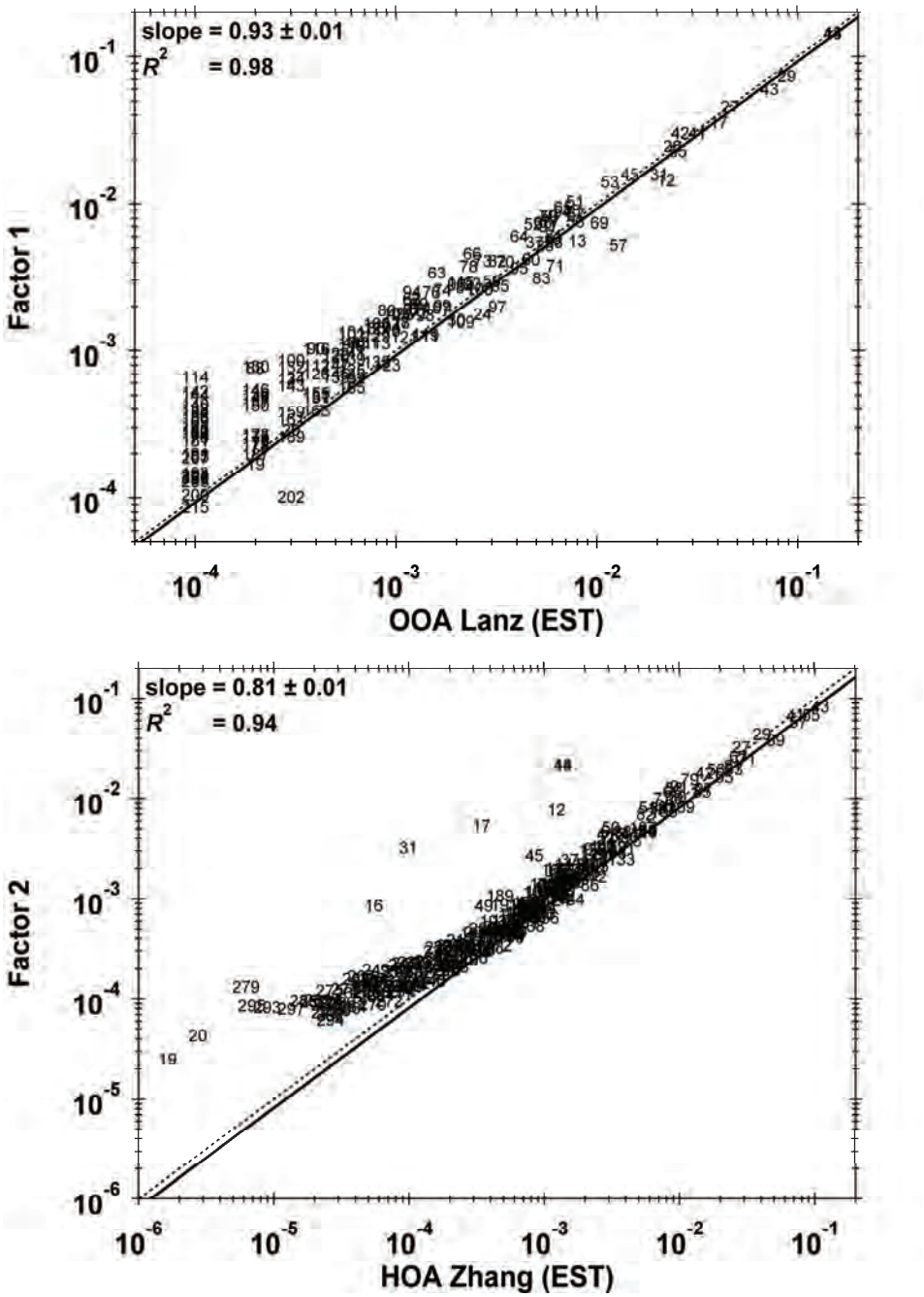


Figure A 17 Correlation of PMF factor 1 MS to OOA1 MS from [*Lanz et al.*, 2008] (top) and factor 2 MS to HOA MS from [*Zhang et al.*, 2005] in 2009.

# Erklärung

Ich versichere, dass ich die von mir vorgelegte Dissertation selbständig angefertigt, die benutzten Quellen und Hilfsmittel vollständig angegeben und die Stellen der Arbeit – einschließlich Tabellen, Karten und Abbildungen – die anderen Werken im Wortlaut oder dem Sinn nach entnommen sind, in jedem Einzelfall als Entlehnung kenntlich gemacht habe; dass diese Dissertation noch keiner anderen Fakultät oder Universität zur Prüfung vorgelegen hat; dass sie – abgesehen von unten angegebenen Teilpublikationen – noch nicht veröffentlicht worden ist sowie, dass ich eine solche Veröffentlichung vor Abschluss des Promotionsverfahrens nicht vornehmen werde. Die Bestimmungen dieser Promotionsordnung sind mir bekannt. Die von mir vorgelegte Dissertation ist von PD Dr. Andreas Hofzumahaus am Forschungszentrum Jülich, ICG-2: Troposphäre betreut worden.

Teilpublikationen:

Fry et al. (2009), Organic nitrate and secondary organic aerosol yield from $NO_3$ oxidation of $\beta$-pinene evaluated using a gas-phase kinetics/aerosol partitioning model, Atmospheric Chemistry and Physics, 9 (4), 1431-1449.

Rollins et al. (2009), Isoprene oxidation by nitrate radical: alkyl nitrate and secondary organic aerosol yields, Atmospheric Chemistry and Physics, 9 (18), 6685-6703.

Köln, den 25.02.2010

Amewu Mensah

# Danksagung

Angesichts der vorangegangenen Seiten gilt mein erster Dank PD Astrid Kiendler-Scharr. Sie hat mich weit über das normale Mass hinaus unterstützt, motiviert und geleitet. Vielen, vielen Dank für dein Verständnis und deine Unterstützung.

Ich danke meinen beiden Prüfern Herrn PD Andreas Hofzumahaus für die angenehme Betreuung als Doktorvater und Herrn Prof. Andreas Wahner nicht nur für die Übernahme des Koreferats sondern auch in seiner Funktion als Institutsdirektor.

Ein grosser Dank geht an die Christiane Nüsslein-Volhard-Stiftung, deren Stipendiatin ich sein durfte. Ich möchte mich nicht nur für die finanzielle Unterstützung, die die Organisation des Alltages als Doktorandin mit Kind wesentlich erleichtert hat, sondern auch für die Möglichkeit sich mit anderen motivierten Wissenschaftlerinnen austauschen zu können bedanken.

Ich bedanke mich bei der Hetero-Gruppe für die schöne und wissenschaftlich stets anregende Zeit, ganz besonders bei Achim, Angela, Ralf, Thomas und meinen beiden Bürogenossen Thorsten und Bettina.

Ich danke Frau Berger für ihre Fürsorglichkeit und Sorgfältigkeit, dem IT-Team, hier im Besonderen Helga London und Michael Decker, für viel Hilfsbereitschaft und Geduld und den Mitarbeitern der Werkstätten für ihre tatkräftige Unterstützung.

Dem gesamten ICG-2 nunmehr IEK-8 danke ich für die tolle Zusammenarbeit und das angenehme Arbeitsklima.

Meine grosse Bewunderung gilt meinen Beifahrern Anke und Miikka für ihre Unerschrockenheit und unerwähnt darf auch nicht die Jülicher Kantine mit ihrem Personal bleiben, die so hervorragend für mein leibliches Wohl gesorgt hat.

Ich danke meinen Eltern, ohne die ich jetzt nicht dort wäre, wo ich jetzt bin. Meiner kleinen Familie Stephan, Romeo und Fiona gilt mein ganz besonderer Dank, die ihr mich jeder auf seine Weise bei dem Unterfangen Doktorarbeit unterstützt und begleitet habt.

Nochmals möchte ich meinen Dank an meine Studienkollegen aller Generationen äussern. Ich habe im Laufe meines Studiums sehr liebe und interessante Menschen kennen gelernt. Ich danke der deutschen Gesellschaft, die mein Studium finanziert und mir damit unabhängig von meiner Herkunft eine hervorragende Ausbildung ermöglicht hat.

*In Memoriam H.T. Davis*

1. **Einsatz von multispektralen Satellitenbilddaten in der Wasserhaushalts- und Stoffstrommodellierung – dargestellt am Beispiel des Rureinzugsgebietes**
   von C. Montzka (2008), XX, 238 Seiten
   ISBN: 978-3-89336-508-1

2. **Ozone Production in the Atmosphere Simulation Chamber SAPHIR**
   by C. A. Richter (2008), XIV, 147 pages
   ISBN: 978-3-89336-513-5

3. **Entwicklung neuer Schutz- und Kontaktierungsschichten für Hochtemperatur-Brennstoffzellen**
   von T. Kiefer (2008), 138 Seiten
   ISBN: 978-3-89336-514-2

4. **Optimierung der Reflektivität keramischer Wärmedämmschichten aus Yttrium-teilstabilisiertem Zirkoniumdioxid für den Einsatz auf metallischen Komponenten in Gasturbinen**
   von A. Stuke (2008), X, 201 Seiten
   ISBN: 978-3-89336-515-9

5. **Lichtstreuende Oberflächen, Schichten und Schichtsysteme zur Verbesserung der Lichteinkopplung in Silizium-Dünnschichtsolarzellen**
   von M. Berginski (2008), XV, 171 Seiten
   ISBN: 978-3-89336-516-6

6. **Politikszenarien für den Klimaschutz IV – Szenarien bis 2030**
   hrsg.von P. Markewitz, F. Chr. Matthes (2008), 376 Seiten
   ISBN 978-3-89336-518-0

7. **Untersuchungen zum Verschmutzungsverhalten rheinischer Braunkohlen in Kohledampferzeugern**
   von A. Schlüter (2008), 164 Seiten
   ISBN 978-3-89336-524-1

8. **Inorganic Microporous Membranes for Gas Separation in Fossil Fuel Power Plants**
   by G. van der Donk (2008), VI, 120 pages
   ISBN: 978-3-89336-525-8

9. **Sinterung von Zirkoniumdioxid-Elektrolyten im Mehrlagenverbund der oxidkeramischen Brennstoffzelle (SOFC)**
   von R. Mücke (2008), VI, 165 Seiten
   ISBN: 978-3-89336-529-6

10. **Safety Considerations on Liquid Hydrogen**
    by K. Verfondern (2008), VIII, 167 pages
    ISBN: 978-3-89336-530-2

11. **Kerosinreformierung für Luftfahrtanwendungen**
von R. C. Samsun (2008), VII, 218 Seiten
ISBN: 978-3-89336-531-9

12. **Der 4. Deutsche Wasserstoff Congress 2008 – Tagungsband**
hrsg. von D. Stolten, B. Emonts, Th. Grube (2008), 269 Seiten
ISBN: 978-3-89336-533-3

13. **Organic matter in Late Devonian sediments as an indicator for environmental changes**
by M. Kloppisch (2008), XII, 188 pages
ISBN: 978-3-89336-534-0

14. **Entschwefelung von Mitteldestillaten für die Anwendung in mobilen Brennstoffzellen-Systemen**
von J. Latz (2008), XII, 215 Seiten
ISBN: 978-3-89336-535-7

15. **RED-IMPACT**
**Impact of Partitioning, Transmutation and Waste Reduction Technologies on the Final Nuclear Waste Disposal**
SYNTHESIS REPORT
ed. by W. von Lensa, R. Nabbi, M. Rossbach (2008), 178 pages
ISBN 978-3-89336-538-8

16. **Ferritic Steel Interconnectors and their Interactions with Ni Base Anodes in Solid Oxide Fuel Cells (SOFC)**
by J. H. Froitzheim (2008), 169 pages
ISBN: 978-3-89336-540-1

17. **Integrated Modelling of Nutrients in Selected River Basins of Turkey**
Results of a bilateral German-Turkish Research Project
project coord. M. Karpuzcu, F. Wendland (2008), XVI, 183 pages
ISBN: 978-3-89336-541-8

18. **Isotopengeochemische Studien zur klimatischen Ausprägung der Jüngeren Dryas in terrestrischen Archiven Eurasiens**
von J. Parplies (2008), XI, 155 Seiten, Anh.
ISBN: 978-3-89336-542-5

19. **Untersuchungen zur Klimavariabilität auf dem Tibetischen Plateau - Ein Beitrag auf der Basis stabiler Kohlenstoff- und Sauerstoffisotope in Jahrringen von Bäumen waldgrenznaher Standorte**
von J. Griessinger (2008), XIII, 172 Seiten
ISBN: 978-3-89336-544-9

20. **Neutron-Irradiation + Helium Hardening & Embrittlement Modeling of 9%Cr-Steels in an Engineering Perspective (HELENA)**
by R. Chaouadi (2008), VIII, 139 pages
ISBN: 978-3-89336-545-6

21. **in Bearbeitung**

22. **Verbundvorhaben APAWAGS (AOEV und Wassergenerierung) – Teilprojekt: Brennstoffreformierung – Schlussbericht**
von R. Peters, R. C. Samsun, J. Pasel, Z. Porš, D. Stolten (2008), VI, 106 Seiten
ISBN: 978-3-89336-547-0

23. **FREEVAL**
Evaluation of a Fire Radiative Power Product derived from Meteosat 8/9 and Identification of Operational User Needs
Final Report
project coord. M. Schultz, M. Wooster (2008), 139 pages
ISBN: 978-3-89336-549-4

24. **Untersuchungen zum Alkaliverhalten unter Oxycoal-Bedingungen**
von C. Weber (2008), VII, 143, XII Seiten
ISBN: 978-3-89336-551-7

25. **Grundlegende Untersuchungen zur Freisetzung von Spurstoffen, Heißgaschemie, Korrosionsbeständigkeit keramischer Werkstoffe und Alkalirückhaltung in der Druckkohlenstaubfeuerung**
von M. Müller (2008), 207 Seiten
ISBN: 978-3-89336-552-4

26. **Analytik von ozoninduzierten phenolischen Sekundärmetaboliten in *Nicotiana tabacum* L. cv Bel W3 mittels LC-MS**
von I. Koch (2008), III, V, 153 Seiten
ISBN 978-3-89336-553-1

27. **IEF-3 Report 2009. Grundlagenforschung für die Anwendung**
(2009), ca. 230 Seiten
ISBN: 978-3-89336-554-8

28. **Influence of Composition and Processing in the Oxidation Behavior of MCrAlY-Coatings for TBC Applications**
by J. Toscano (2009), 168 pages
ISBN: 978-3-89336-556-2

29. **Modellgestützte Analyse signifikanter Phosphorbelastungen in hessischen Oberflächengewässern aus diffusen und punktuellen Quellen**
von B. Tetzlaff (2009), 149 Seiten
ISBN: 978-3-89336-557-9

30. **Nickelreaktivlot / Oxidkeramik – Fügungen als elektrisch isolierende Dichtungskonzepte für Hochtemperatur-Brennstoffzellen-Stacks**
von S. Zügner (2009), 136 Seiten
ISBN: 978-3-89336-558-6

31. **Langzeitbeobachtung der Dosisbelastung der Bevölkerung in radioaktiv kontaminierten Gebieten Weißrusslands – Korma-Studie**
von H. Dederichs, J. Pillath, B. Heuel-Fabianek, P. Hill, R. Lennartz (2009), Getr. Pag.
ISBN: 978-3-89336-532-3

32. **Herstellung von Hochtemperatur-Brennstoffzellen über physikalische Gasphasenabscheidung**
von N. Jordán Escalona (2009), 148 Seiten
ISBN: 978-3-89336-532-3

33. **Real-time Digital Control of Plasma Position and Shape on the TEXTOR Tokamak**
by M. Mitri (2009), IV, 128 pages
ISBN: 978-3-89336-567-8

34. **Freisetzung und Einbindung von Alkalimetallverbindungen in kohlebefeuerten Kombikraftwerken**
von M. Müller (2009), 155 Seiten
ISBN: 978-3-89336-568-5

35. **Kosten von Brennstoffzellensystemen auf Massenbasis in Abhängigkeit von der Absatzmenge**
von J. Werhahn (2009), 242 Seiten
ISBN: 978-3-89336-569-2

36. **Einfluss von Reoxidationszyklen auf die Betriebsfestigkeit von anodengestützten Festoxid-Brennstoffzellen**
von M. Ettler (2009), 138 Seiten
ISBN: 978-3-89336-570-8

37. **Großflächige Plasmaabscheidung von mikrokristallinem Silizium für mikromorphe Dünnschichtsolarmodule**
von T. Kilper (2009), XVII, 154 Seiten
ISBN: 978-3-89336-572-2

38. **Generalized detailed balance theory of solar cells**
by T. Kirchartz (2009), IV, 198 pages
ISBN: 978-3-89336-573-9

39. **The Influence of the Dynamic Ergodic Divertor on the Radial Electric Field at the Tokamak TEXTOR**
von J. W. Coenen (2009), xii, 122, XXVI pages
ISBN: 978-3-89336-574-6

40. **Sicherheitstechnik im Wandel Nuklearer Systeme**
von K. Nünighoff (2009), viii, 215 Seiten
ISBN: 978-3-89336-578-4

41. **Pulvermetallurgie hochporöser NiTi-Legierungen für Implanat- und Dämpfungsanwendungen**
von M. Köhl (2009), XVII, 199 Seiten
ISBN: 978-3-89336-580-7

42. **Einfluss der Bondcoatzusammensetzung und Herstellungsparameter auf die Lebensdauer von Wärmedämmschichten bei zyklischer Temperaturbelastung**
von M. Subanovic (2009), 188, VI Seiten
ISBN: 978-3-89336-582-1

43. **Oxygen Permeation and Thermo-Chemical Stability of Oxygen Permeation Membrane Materials for the Oxyfuel Process**
by A. J. Ellett (2009), 176 pages
ISBN: 978-3-89336-581-4

44. **Korrosion von polykristallinem Aluminiumoxid (PCA) durch Metalljodidschmelzen sowie deren Benetzungseigenschaften**
von S. C. Fischer (2009), 148 Seiten
ISBN: 978-3-89336-584-5

45. **IEF-3 Report 2009. Basic Research for Applications**
(2009), 217 Seiten
ISBN: 978-3-89336-585-2

46. **Verbundvorhaben ELBASYS (Elektrische Basissysteme in einem CFK-Rumpf) - Teilprojekt: Brennstoffzellenabgase zur Tankinertisierung - Schlussbericht**
von R. Peters, J. Latz, J. Pasel, R. C. Samsun, D. Stolten
(2009), xi, 202 Seiten
ISBN: 978-3-89336-587-6

47. **Aging of $^{14}$C-labeled Atrazine Residues in Soil: Location, Characterization and Biological Accessibility**
by N. D. Jablonowski (2009), IX, 104 pages
ISBN: 978-3-89336-588-3

48. **Entwicklung eines energetischen Sanierungsmodells für den europäischen Wohngebäudesektor unter dem Aspekt der Erstellung von Szenarien für Energie- und $CO_2$ - Einsparpotenziale bis 2030**
von P. Hansen (2009), XXII, 281 Seiten
ISBN: 978-3-89336-590-6

49. **Reduktion der Chromfreisetzung aus metallischen Interkonnektoren für Hochtemperaturbrennstofzellen durch Schutzschichtsysteme**
von R. Trebbels (2009), iii, 135 Seiten
ISBN: 978-3-89336-591-3

50. **Bruchmechanische Untersuchung von Metall / Keramik-Verbundsystemen für die Anwendung in der Hochtemperaturbrennstoffzelle**
von B. Kuhn (2009), 118 Seiten
ISBN: 978-3-89336-592-0

51. **Wasserstoff-Emissionen und ihre Auswirkungen auf den arktischen Ozonverlust**
**Risikoanalyse einer globalen Wasserstoffwirtschaft**
von T. Feck (2009), 180 Seiten
ISBN: 978-3-89336-593-7

52. **Development of a new Online Method for Compound Specific Measurements of Organic Aerosols**
by T. Hohaus (2009), 156 pages
ISBN: 978-3-89336-596-8

53. **Entwicklung einer FPGA basierten Ansteuerungselektronik für Justageeinheiten im Michelson Interferometer**
von H. Nöldgen (2009), 121 Seiten
ISBN: 978-3-89336-599-9

54. **Observation – and model – based study of the extratropical UT/LS**
by A. Kunz (2010), xii, 120, xii pages
ISBN: 978-3-89336-603-3

55. **Herstellung polykristalliner Szintillatoren für die Positronen-Emissions-Tomographie (PET)**
von S. K. Karim (2010), VIII, 154 Seiten
ISBN: 978-3-89336-610-1

56. **Kombination eines Gebäudekondensators mit H2-Rekombinatorelementen in Leichwasserreaktoren**
von S. Kelm (2010), vii, 119 Seiten
ISBN: 978-3-89336-611-8

57. **Plant Leaf Motion Estimation Using A 5D Affine Optical Flow Model**
by T. Schuchert (2010), X, 143 pages
ISBN: 978-3-89336-613-2

58. **Tracer-tracer relations as a tool for research on polar ozone loss**
by R. Müller (2010), 116 pages
ISBN: 978-3-89336-614-9

59. **Sorption of polycyclic aromatic hydrocarbon (PAH) to Yangtze River sediments and their components**
by J. Zhang (2010), X, 109 pages
ISBN: 978-3-89336-616-3

60. **Weltweite Innovationen bei der Entwicklung von CCS-Technologien und Möglichkeiten der Nutzung und des Recyclings von $CO_2$**
Studie im Auftrag des BMWi
von W. Kuckshinrichs et al. (2010), X, 139 Seiten
ISBN: 978-3-89336-617-0

61. **Herstellung und Charakterisierung von sauerstoffionenleitenden Dünnschichtmembranstrukturen**
von M. Betz (2010), XII, 112 Seiten
ISBN: 978-3-89336-618-7

62. **Politikszenarien für den Klimaschutz V – auf dem Weg zum Strukturwandel, Treibhausgas-Emissionsszenarien bis zum Jahr 2030**
hrsg. von P. Hansen, F. Chr. Matthes (2010), 276 Seiten
ISBN: 978-3-89336-619-4

63. **Charakterisierung Biogener Sekundärer Organischer Aerosole mit Statistischen Methoden**
von C. Spindler (2010), iv, 163 Seiten
ISBN: 978-3-89336-622-4

64. **Stabile Algorithmen für die Magnetotomographie an Brennstoffzellen**
von M. Wannert (2010), ix, 119 Seiten
ISBN: 978-3-89336-623-1

65. **Sauerstofftransport und Degradationsverhalten von Hochtemperaturmembranen für CO2-freie Kraftwerke**
von D. Schlehuber (2010), VII, 139 Seiten
ISBN: 978-3-89336-630-9

66. **Entwicklung und Herstellung von foliengegossenen, anodengestützten Festoxidbrennstoffzellen**
von W. Schafbauer (2010), VI, 164 Seiten
ISBN: 978-3-89336-631-6

67. **Disposal strategy of proton irradiated mercury from high power spallation sources**
by S. Chiriki (2010), xiv, 124 pages
ISBN: 978-3-89336-632-3

68. **Oxides with polyatomic anions considered as new electrolyte materials for solid oxide fuel cells (SOFCs)**
by O. H. Bin Hassan (2010), vii, 121 pages
ISBN: 978-3-89336-633-0

69. **Von der Komponente zum Stack: Entwicklung und Auslegung von HT-PEFC-Stacks der 5 kW-Klasse**
von A. Bendzulla (2010), IX, 203 Seiten
ISBN: 978-3-89336-634-7

70. **Satellitengestützte Schwerewellenmessungen in der Atmosphäre und Perspektiven einer zukünftigen ESA Mission (PREMIER)**
von S. Höfer (2010), 81 Seiten
ISBN: 978-3-89336-637-8

71. **Untersuchungen der Verhältnisse stabiler Kohlenstoffisotope in atmosphärisch relevanten VOC in Simulations- und Feldexperimenten**
von H. Spahn (2010), IV, 210 Seiten
ISBN: 978-3-89336-638-5

72. **Entwicklung und Charakterisierung eines metallischen Substrats für nanostrukturierte keramische Gastrennmembranen**
von K. Brands (2010), vii, 137 Seiten
ISBN: 978-3-89336-640-8

73. **Hybridisierung und Regelung eines mobilen Direktmethanol-Brennstoffzellen-Systems**
von J. Chr. Wilhelm (2010), 220 Seiten
ISBN: 978-3-89336-642-2

74. **Charakterisierung perowskitischer Hochtemperaturmembranen zur Sauerstoffbereitstellung für fossil gefeuerte Kraftwerksprozesse**
von S.A. Möbius (2010) III, 208 Seiten
ISBN: 978-3-89336-643-9

75. **Characterization of natural porous media by NMR and MRI techniques: High and low magnetic field studies for estimation of hydraulic properties**
by L.-R. Stingaciu (2010), 96 pages
ISBN: 978-3-89336-645-3

76. **Hydrological Characterization of a Forest Soil Using Electrical Resistivity Tomography**
by Chr. Oberdörster (2010), XXI, 151 pages
ISBN: 978-3-89336-647-7

77. **Ableitung von atomarem Sauerstoff und Wasserstoff aus Satellitendaten und deren Abhängigkeit vom solaren Zyklus**
von C. Lehmann (2010), 127 Seiten
ISBN: 978-3-89336-649-1

78. **18th World Hydrogen Energy Conference 2010 – WHEC2010 Proceedings**
**Speeches and Plenary Talks**
ed. by D. Stolten, B. Emonts (2010)
ISBN: 978-3-89336-658-3

78-1. **18th World Hydrogen Energy Conference 2010 – WHEC2010 Proceedings**
**Parallel Sessions Book 1:**
**Fuel Cell Basics / Fuel Infrastructures**
ed. by D. Stolten, T. Grube (2010), ca. 460 pages
ISBN: 978-3-89336-651-4

78-2. **18th World Hydrogen Energy Conference 2010 – WHEC2010 Proceedings**
**Parallel Sessions Book 2:**
**Hydrogen Production Technologies – Part 1**
ed. by D. Stolten, T. Grube (2010), ca. 400 pages
ISBN: 978-3-89336-652-1

78-3. **18th World Hydrogen Energy Conference 2010 – WHEC2010 Proceedings**
**Parallel Sessions Book 3:**
**Hydrogen Production Technologies – Part 2**
ed. by D. Stolten, T. Grube (2010), ca. 640 pages
ISBN: 978-3-89336-653-8

78-4. **18th World Hydrogen Energy Conference 2010 – WHEC2010 Proceedings**
**Parallel Sessions Book 4:**
**Storage Systems / Policy Perspectives, Initiatives and Cooperations**
ed. by D. Stolten, T. Grube (2010), ca. 500 pages
ISBN: 978-3-89336-654-5

78-5. **18th World Hydrogen Energy Conference 2010 – WHEC2010 Proceedings**
**Parallel Sessions Book 5:**
**Stategic Analysis / Safety Issues / Existing and Emerging Markets**
ed. by D. Stolten, T. Grube (2010), ca. 530 pages
ISBN: 978-3-89336-655-2

78-6. **18th World Hydrogen Energy Conference 2010 – WHEC2010 Proceedings**
**Parallel Sessions Book 6:**
**Stationary Applications / Transportation Applications**
ed. by D. Stolten, T. Grube (2010), ca. 330 pages
ISBN: 978-3-89336-656-9

78 Set (complete book series)

**18th World Hydrogen Energy Conference 2010 – WHEC2010 Proceedings**
ed. by D. Stolten, T. Grube, B. Emonts (2010)
ISBN: 978-3-89336-657-6

79. **Ultrafast voltex core dynamics investigated by finite-element micromagnetic simulations**
by S. Gliga (2010), vi, 144 pages
ISBN: 978-3-89336-660-6

80. **Herstellung und Charakterisierung von keramik- und metallgestützten Membranschichten für die $CO_2$-Abtrennung in fossilen Kraftwerken**
von F. Hauler (2010), XVIII, 178 Seiten
ISBN: 978-3-89336-662-0

81. **Experiments and numerical studies on transport of sulfadiazine in soil columns**
by M. Unold (2010), xvi, 115 pages
ISBN: 978-3-89336-663-7

82. **Prompt-Gamma-Neutronen-Aktivierungs-Analyse zur zerstörungsfreien Charakterisierung radioaktiver Abfälle**
von J.P.H. Kettler (2010), iv, 205 Seiten
ISBN: 978-3-89336-665-1

83. **Transportparameter dünner geträgerter Kathodenschichten der oxidkeramischen Brennstoffzelle**
von C. Wedershoven (2010), vi, 137 Seiten
ISBN: 978-3-89336-666-8

84. **Charakterisierung der Quellverteilung von Feinstaub und Stickoxiden in ländlichem und städtischem Gebiet**
von S. Urban (2010), vi, 211 Seiten
ISBN: 978-3-89336-669-9

85. **Optics of Nanostructured Thin-Film Silicon Solar Cells**
by C. Haase (2010), 150 pages
ISBN: 978-3-89336-671-2

86. **Entwicklung einer Isolationsschicht für einen Leichtbau-SOFC-Stack**
von R. Berhane (2010), X, 162 Seiten
ISBN: 978-3-89336-672-9

87. **Hydrogen recycling and transport in the helical divertor of TEXTOR**
by M. Clever (2010), x, 172 pages
ISBN: 978-3-89336-673-6

88. **Räumlich differenzierte Quantifizierung der N- und P-Einträge in Grundwasser und Oberflächengewässer in Nordrhein-Westfalen unter besonderer Berücksichtigung diffuser landwirtschaftlicher Quellen**
von F. Wendland et. al. (2010), xii, 216 Seiten
ISBN: 978-3-89336-674-3

89. **Oxidationskinetik innovativer Kohlenstoffmaterialien hinsichtlich schwerer Lufteinbruchstörfälle in HTR´s und Graphitentsorgung oder Aufarbeitung**
von B. Schlögl (2010), ix, 117 Seiten
ISBN: 978-3-89336-676-7

90. **Chemische Heißgasreinigung bei Biomassenvergasungsprozessen**
von M. Stemmler (2010), xv, 196 Seiten
ISBN: 978-3-89336-678-1

91. **Untersuchung und Optimierung der Serienverschaltung von Silizium-Dünnschicht-Solarmodulen**
von S. Haas (2010), ii, 202 Seiten
ISBN: 978-3-89336-680-4

92. **Non-invasive monitoring of water and solute fluxes in a cropped soil**
by S. Garré (2010), xxiv, 133 pages
ISBN: 978-3-89336-681-1

93. **Improved hydrogen sorption kinetics in wet ball milled Mg hydrides**
by L. Meng (2011), II, 119 pages
ISBN: 978-3-89336-687-3

94. **Materials for Advanced Power Engineering 2010**
ed. by J. Lecomte-Beckers, Q. Contrepois, T. Beck and B. Kuhn
(2010), 1327 pages
ISBN: 978-3-89336-685-9

95. **2D cross-hole MMR – Survey design and sensitivity analysis for cross-hole applications of the magnetometric resistivity**
by D. Fielitz (2011), xvi, 123 pages
ISBN: 978-3-89336-689-7

96. **Untersuchungen zur Oberflächenspannung von Kohleschlacken unter Vergasungsbedingungen**
von T. Melchior (2011), xvii, 270 Seiten
ISBN: 978-3-89336-690-3

97. **Secondary Organic Aerosols: Chemical Aging, Hygroscopicity, and Cloud Droplet Activation**
by A. Buchholz (2011), xiv, 134 pages
ISBN: 978-3-89336-691-0

98. **Chrom-bezogene Degradation von Festoxid-Brennstoffzellen**
von A. Neumann (2011), xvi, 218 Seiten
ISBN: 978-3-89336-692-7

99. **Amorphous and microcrystalline silicon applied in very thin tandem solar cells**
by S. Schicho (2011), XII, 190 pages
ISBN: 978-3-89336-693-4

100. **Sol-gel and nano-suspension electrolyte layers for high performance solid oxide fuel cells**
by F. Han (2011), iv, 131 pages
ISBN: 978-3-89336-694-1

101. **Impact of different vertical transport representations on simulating processes in the tropical tropopause layer (TTL)**
by F. Plöger (2011), vi, 104 pages
ISBN: 978-3-89336-695-8

102. **Untersuchung optischer Nanostrukturen für die Photovoltaik mit Nahfeldmikroskopie**
von T. Beckers (2011), xiii, 128 Seiten
ISBN: 978-3-89336-696-5

103. **Impact of contamination on hydrogenated amorphous silicon thin films & solar cells**
by J. Wördenweber (2011), XIV, 138 pages
ISBN: 978-3-89336-697-2

104. **Water and Organic Nitrate Detection in an AMS: Laboratory Characterization and Application to Ambient Measurements**
by A. Mensah (2011), XI, 111 pages
ISBN: 978-3-89336-698-9

Energie & Umwelt / Energy & Environment
Band / Volume 104
ISBN 978-3-89336-698-9

JÜLICH
FORSCHUNGSZENTRUM